X-ray Spectral Signatures of Accreting Black Holes

CANDIDATE
Andrea Martocchia

SUPERVISORS
Vladimír Karas
Giorgio Matt
John Miller

Thesis submitted for the degree of *"Doctor Philosophiæ"*.

October 2000

X-ray Spectral Signatures of Accreting Black Holes

CANDIDATE

Andrea Martocchia

SUPERVISORS

Vladimír Karas
Giorgio Matt
John Miller

Thesis submitted for the degree of *"Doctor Philosophiæ"*.

October 2000

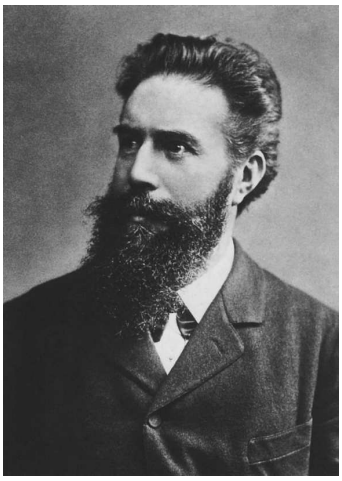

Wilhelm Conrad Röntgen (1845–1923),
the discoverer of X-rays

Contents

Introduction

Motivation

In recent years an important line of research was developed in the field of high energy astrophysics and gravitation, concerning the computation of relativistic distortions of spectral features from accreting Black Hole [**BH**] systems. These computations are needed to get observational evidence of the existence of astrophysical BHs: the physical parameters of accreting BHs may be deduced from the form of the spectral features observed in the X-ray band through satellite missions. Dealing with methods which are proved to be useful and practical to find out BHs, people also tried to establish criteria in order to determine the BH angular momentum.

In order to obtain astrophysically realistic results, it has been necessary to combine the general-relativistic model of the BH gravitational field with the local physics of radiation processes in the accreting medium. This theoretical effort was linked to the complex phenomenology observed through X-ray satellite data and in other spectral bands, resulting in a substantial improvement of our understanding of the subject, which eventually reached, to some extent, a textbook level.

Our own contribution to these developments is presented in this Dissertation. In particular, in order to allow comparison with the data we developed a computational tool (kerrspec) aimed to fit the observed X-ray spectral features on the base of fully relativistic models. The newest results we got are presented in the last sections of this work.

Relativistic Distortions of Spectra from Accreting BHs

The integration of photon paths in the spinning BH (Kerr) metric and the computation of spectral distortions from accreting BH systems are needed

since complex emission features with shapes and energy most naturally explained in terms of relativistic effects have recently been discovered by X-ray satellites. The interest in such high-energy spectral distortions arised especially after the detection of the broad, asymmetric profile of the iron $K\alpha$ fluorescent line in the X-ray data of the Seyfert galaxy MCG–6-30-15 (Tanaka *et al.* 1995), whose shape is thought to be due to strong gravity effects taking place at only a few gravitational radii from the BH event horizon. Also the large equivalent width of the fluorescent Kα line and the position of its centroid energy may be understood if the line is produced in a medium with fast rotational motion, very near to a BH.

All classes of astrophysical objects where an accreting BH could be hosted are of interest in this research. In the Milky Way such objects are called (galactic, stellar mass) Black Hole Candidates [**BHC**s], whereas every Active Galactic Nucleus [**AGN**], as well as most (possibly all) galaxies, could host a supermassive BH at their center. The gravitational field around such BHs can be described by the Kerr solution within the framework of the Theory of General Relativity [**GR**].

Signatures of a BH spacetime should be contained in the electromagnetic radiation which emerges from its accretion disc [**AD**], i.e. the disklike configuration of the accreting matter, and from a putative "corona" above it. This radiation is mainly concentrated in the X-ray band. The current models basically involve a *primary* emission, originating in the hot coronal plasma – which illuminates the disc and reveals itself in the form of a powerlaw-like spectrum – and a *secondary* emission, consisting of reflected and fluorescent features from the illuminated disc itself. We wish to stress that *both* of them must be modelled self-consistently, including the GR effects they undergo. All photon paths are thus treated in terms of geometrical optics in a curved spacetime.

Both continuum and line emission from accretion discs around Kerr BHs are currently being investigated under simplified geometrical and physical assumptions. However, further development is necessary in order to address more complicated and realistic physical models for the primary X-ray source, for the accretion flow and for their mutual interaction as well. Variability issues do also need to be self-consistently investigated in more detail, but they are not in the main focus of the present Thesis. In this work we will just sketch the main recent achievements on these issues. Instead, we concentrate ourselves on the computation of selected spectral features.

Description of the Dissertation

Aim of the present dissertation is, first of all, to provide a deeper insight into the mentioned issues, from a theoretical as well as from a phenomenological point of view.

The text is organized as follows. Chapter 1 is devoted to a general introduction on the subject of astrophysical BH systems, on the methods to find them out, on current models for accretion and variability properties, on what is actually observed, while chapter 2 deals with the mathematical tools provided by GR to describe static – i.e. *Schwarzschild* – or rotating – i.e. *Kerr* – BH metrics, and the particle motion allowed in such spacetimes.

In chapter 3 we illustrate and compare systematically the computations of synthetic line profiles and of other spectral features from relativistic accretion discs, taking also into account the various uncertainties in the current models. After giving some further mathematical background on relativistic accretion discs, geometrical optics and computational techniques of geodesics in Kerr metric, we review the work that has been done in the past and, starting with section 3.5, introduce also our own achievements in calculating primary illumination (Martocchia 1996), emissivity law and local spectra (Martocchia & Matt 1996; Martocchia, Matt & Karas 1999; Martocchia, Karas & Matt 2000) and relativistic spectra at infinity from such systems (Martocchia, Karas & Matt 2000).

Then we describe the fitting technique that we have recently developed, that is the kerrspec tool, to be used in the standard XSPEC software for X-ray data analysis (Martocchia, Matt & Karas, 2000).

The last chapter (4) is aimed to show the new results obtained with kerrspec, and to mention open lines of research, with particular regard to some important sources (Martocchia, Matt & Karas 2000; Martocchia, Haardt & Matt 2000; Karas, Martocchia & Šubr 2000).

Acknowledgements

This Dissertation has been written in the summer 2000, during the last months of my PhD stay at the International School for Advanced Studies (SISSA), in Trieste. It is based on the work I did mostly in collaboration with Vladimír Karas in Prague and Giorgio Matt in Rome. I am grateful to both of them for the constant help and personal friendship developed during the past years.

Being Rome my home town, I will remember these PhD time essentially as the time of Trieste and Prague.
In Trieste, I wish to warmly thank John Miller for the support during my stay.
In Prague, I also want to say thank you to the people of the Institute of Astronomy of the Charles University, that hosted me in various occasions, for the kind hospitality and the nice athmosphere I enjoyed there.

To my work, the Tartarus on-line archive of ASCA data, which is supported by Jane Turner and Kirpal Nandra under NASA grants NAG5-7385 and NAG5-7067, has been essential.

Chapter 1

Astrophysical Black Holes

1.1 Historical Remarks

The issues we are going to deal with are connected with the problem of the existence of black holes,[1] and with the possibility of determining their physical properties: the mass and the angular momentum – spin.

It is already in the famous works of Michell (1784) and Laplace (1796), late in the 18th century, that we can find the first account of the objects with the properties that are nowadays attributed to black holes. In the classical GR theory a *Black Hole* is an object which does not allow information – neither radiation, nor particles – to be trasmitted outside the *event horizon*. In the static case, this happens when the mass M has entirely collapsed within the *Schwarzschild radius*

$$r_s = 2\,\frac{GM}{c^2}.$$

Thus the event horizon is what actually characterizes a BH with respect to other models of compact objects which possess a solid surface.

Historically, the observational search for black holes is linked with the origin of extragalactic astronomy and, in particular, of what is now called *active galaxies*. This branch of astronomy can be traced back to the works of H. D. Curtis (1918), who described a long jet of material outcoming from the elliptical galaxy M 87, and C. K. Seyfert (1943) who discovered a class of extragalactic objects — spiral galaxies with particularly compact and bright nuclei, now called Seyfert's galaxies. There is now both direct and indirect evidence that active galactic nuclei are actually powered by supermassive BHs (for a review: Ho & Kormendy 2000; cp. section 1.4.2).

[1] For recent references on the problem of the existence of astrophysical BHs, see e.g.: Celotti *et al.* 1999; Robertson 1998; Menou *et al.* 1997.

But, interestingly, Albert Einstein himself did not believe in the existence of BHs (Einstein 1939);[2] the first modern scientific paper to describe these elusive objects and the effects on particles in their vicinity was by Oppenheimer & Snyder (1939). However, attention has been increasingly devoted to BHs only from the 60's, when they were invoked as a possible solution to the "missing mass" puzzle (Hoyle *et al.* 1964) and to the problem of the nature of *quasars* (Zeldovich & Novikov 1964, Salpeter 1964).

There are different kinds of environments in which we expect to find a BH. A stellar-mass BH can be the remnant of a collapsed, massive star, or the product of an interaction in a binary system. Supermassive BHs are expected in the centers of galaxies, as the product of inner dynamics and huge mass collapses; recent results induce us to think that most, if not all, nucleated galaxies harbor a very massive, compact object – possibly a massive BH – at their center (Kormendy & Richstone 1995; Magorrian *et al.* 1998). *Primordial* BHs are thought to have also formed, as the result of fluctuations or phase transitions in the early universe, when conditions were so extreme that BHs of all masses might have been produced.[3]

Low-mass BHs are more difficult to form because a much higher mass concentration is required to prompt the gravitational collapse. In general, the BH "density"[4] is proportional to $1/M^2$: for a solar mass BH the density required is forty times that of a nucleus, while a BH of $10^8 M_\odot$ has the density of the water.

Chandrasekhar (1931) found that electron degeneracy cannot prevent a cold body with $M \gtrsim 1.44 M_\odot$ ("Chandrasekhar's limit") from collapsing. The Chandrasekhar's limit is the boundary value to the existence of white dwarf stars (WD); however, for a higher mass the collapse may stop as the particles find a stable configuration, for instance after weak interactions take place, forming a neutron star (NS).

But NSs cannot have arbitrarily large masses, either: there is a maximum mass value, after which the pressure cannot balance gravity, a value that is believed to reside somewhere above the Chandrasekhar's limit, also depending on the angular momentum. Rhoades & Ruffini (1974), on the base of some symplifying assumptions on the equation of state (which is otherwise

[2] This controversy is nicely described in an article published on *Scientific American* (June 1996). See also Celotti *et al.* (1999).

[3] Primordial BHs can be discovered through *microlensing* phenomena. However, we will not deal with them further in this work because they are not connected with X-ray observational searches. We will focus instead on stellar mass (galactic) and supermassive BHs.

[4] M/V, using $V \equiv \frac{3}{4}\pi r_s^3$ and eq. (2.6).

rather uncertain for the matter in a NS), calculated a limit mass of $\sim 3.2 M_\odot$. However, when some of the assumptions are relaxed, the limit value can rise up to $\sim 14.3 M_\odot$.[5]

Thus, even after proving the existence of a large mass concentration, to "see" a BH we still need confirmation of the presence of the event horizon. This because gravity theories other than GR as well as different models of compact objects can provide analogous predictions of large mass concentrations. In particular, for galactic compact objects there are well-known (WDs, NSs) and less known alternatives to BHs (strange stars, Q stars, collapsars, "red" BHs, ...), while for supermassive compact objects models like: dense stellar clusters, "superstars", magnetoids etc. have less clearly defined properties.

1.2 Searching for Black Holes

Indications of the existence of extremely compact objects in the core of galaxies and galactic BH candidates usually come from the observation of kinematic properties in the innermost part of such systems.

In the case of galactic X-ray binary systems, mass estimates are based on the determination of the *mass function*, on the overall photometric variability (*light curves*), and on the variation of some specific spectral feature. One can constrain the mass of the central object by observing the spectral lines of the secondary star. Their Doppler shifts give an estimate of the radial velocity, and this can be combined with the orbital period of the binary, and translated through Kepler's third law into the mass function for the compact object:

$$f(M_X) = \frac{M_X^3 \sin^3 i}{(M_X + M_2)^2} = K^3 \frac{P}{2\pi G} \tag{1.1}$$

where i is the orbital axis inclination with respect to the observer, M_X the mass of the compact star, M_2 the mass of the secondary (directly observable) star, K is the latter's velocity amplitude and P is the period. Thus

$$f(M_X) = M_X \frac{\sin^3 i}{(1 + M_2/M_X)^2}$$

gives at least a firm lower limit to M_X. The uncertainty introduced by the inclination angle in (1.1) is clearly overcome if the system shows occultations.

[5]For a detailed discussion on these issues see e.g. Miller (1997), and references therein.

Other ways to test the presence of BHs are connected with variability. Spectroscopic studies are, in a certain sense, complementary to the study of light curves and variability of individual spectral features: the two methods give independent proof of huge mass concentrations. The variability timescale Δt in particular gives a hint of the involved dimensions: causality implies a source size less than $R \sim c\Delta t$. If R results to be small, as often happens, the BH hypothesis is favoured.

Although variability issues will not be investigated in detail in the present work, ways to discoved BHs through variability are worth to be mentioned. For instance, the issue of Quasi Periodic Oscillations is crucial because very much linked with GR (e.g. Cui *et al.*, 1998; see section 1.7), although most of QPO sources may contain neutron stars rather than BHs. Reverberation, i.e. investigation of illuminated matter response to variations of the primary flux, is also used as a method for BH mass estimates. The time-delayed response of the emission lines to continuum variations allows to infer the size of the (broad) line emitting region, which is then combined with measurements of the Doppler widths of the variable line component (e.g. Peterson & Wandel, 2000; Gebhardt *et al.*, 2000. On reverberation studies, see also section 3.4).

We already mentioned that the question of the existence of an event horizon is crucial. Showing the very existence of an event horizon gives the best possible evidence of a BH. But the event horizon is no solid surface and therefore cannot be observed directly through electromagnetic radiation. If the accretion flow is advection-dominated, it may be possible to discriminate between compact objects with or without an event horizon, as explained in section 1.3.1.

A different argument is based on the configuration of the accreting matter: for instance the location of the innermost emitting orbits, location which can be inferred through analyzing the spectral features. Zhang *et al.* (1997) for instance claimed that the strong soft X-ray component detected in some spectral states of GRS 1915+105 is due to thermal emission from the innermost region of a relativistic accretion disc extending where only a spinning BH metric would allow (see section 4.5).

The spectroscopical analysis of velocity fields in the innermost region of the accreting flow is also important and can be adopted for both AGN and BHCs. This can be done observing line shifts, or the broadening and relativistic distortion of selected spectral features.

With this method, very strong mass concentrations have been discovered in the centres of many galaxies, including ours.

In the Milky Way, very large proper motions of the stars have been measured in the vicinity of the radio source Sgr A*, which coincides with the dynamical center of the galaxy, implying that a central mass of about $2.6 \times 10^6 M_\odot$ is confined in a volume of ~ 72 Schwarzschild radii (Lo et al., 1998) i.e. less than 10^{-6} cubic parsecs (Ghez A.M. *et al.*, 1998).

The water maser emission feature in the spectrum of NGC 4258 (M106) is clearly originated from a sub-parsec-diameter accretion disc where velocity fields are of the order of 470 km s^{-1}, so that a central mass of 3.6×10^7 $M_\odot$ is estimated to reside within a radius of less than 0.13 parsec (Miyoshi *et al.* 1995; Herrnstein *et al.* 1999).

However, the water maser method as well as the spectroscopic analysis of velocity fields are diagnostics for matter at $\gtrsim 10^3$ gravitational radii from the central compact object. Conversely, the present dissertation is focused on the study of phenomena taking place very near to the compact object, i.e. in very strong fields, through looking at the spectral distortions of relativistic origin. Those distortions, which have been detected in the X-ray band in the iron Kα line profile of some sources, can probe distances of just a few gravitational radii. Our aim is precisely to isolate what is due to the spacetime curvature from all other possibly involved effects.

1.3 Accreting Black Hole Systems

We have just explained that to look for a BH means in fact to explore the properties of the environment where it may be hosted. After the first discoveries of powerful galactic X-ray sources through rocket experiments in the Sixties (section 4.1), a model was proposed in which the strong high-energy emission originates in the process of accretion onto a compact object in a binary system. Soon it was clear that the accreted material would be carrying so much angular momentum that it would not fall onto the compact object along radial paths, but rather be drawn into a thin accretion disc and slowly spiral inwards as a result of viscous drag. The compact object could be either a NS or a BH. The efficiency of power conversion in the latter case can be extremely high (see section 1.4); thus accretion onto a BH was immediately recognized to be a viable mechanism also for explaining the AGN phenomenon, where the energies at play are enormous.

Among the first works in which astrophysical accreting BH systems were modelled, let us recall Lynden-Bell (1969), Pringle & Rees (1972) and Shields (1978).

In this section we describe what are the current models of astrophysical

BH plus accreting flow systems, and what sort of spectra and variability are they expected to produce.

1.3.1 Accretion Flows: Discs and Coronae

After some years of rush, often contradictory development, accretion disc theory nowadays seems to have reached a status in which important concepts have been focused and understood, specific models have been developed and explored in great detail, many difficult calculations have been made; but the actual correspondence of all this to the real systems is not sufficiently established yet, and it appears that important points may still be lacking.

The first accretion model was developed by *Bondi & Hoyle* (1944), who considered a simple **spherical** configuration where the material falls inwards, heating up because of compression. This is an adiabatic process with index $\gamma = 5/3$. The matter can radiate away only a fraction of the heat before crossing the event horizon: the efficiency of this process is generally small and depends on the electron-proton coupling, on the emission mechanism, and the magnetic field may also play an important role.

If a sufficient amount of angular momentum is involved, then accretion must take place in a disk-like configuration. The accretion flow will be axially symmetric in the first approximation, although various kinds of perturbations can arise. The efficiency of the radiation escaping the system can be much higher than in the spherical case, even if a part of the heat produced locally is advected into the hole. In the steady-state, energy, mass and angular momentum conservation hold and can be expressed through corresponding equations. For the energy balance, it is thus assumed that the sum of the heat radiated away plus the one advected into the event horizon is equal to the whole amount which is produced locally.

Since the work of *Shakura & Sunyaev* (1973) a model has been developed to describe geometrically thin ($h(R) \ll R$, $\frac{\dot{M}}{\dot{M}_{Edd}} < 1$) and optically thick (i.e. completely opaque) discs, lying on the equatorial plane (**SS** discs). Here the orbital dynamics is dominated by the gravitation, thus the matter is ordered in a *Keplerian* velocity field: the radial component is small with respect to the tangential one, and the relativistic formulae for constant circular, equatorial motion can be adopted (see section 3.1). Physically, this case is likely to occur when the matter is dense and the pressure is gas-dominated. All the heat produced is supposed to be radiated away (no advection) like in a

blackbody with an effective temperature[6] $T_{eff} \propto R^{-3/4}M^{-1/4}$. Thus in the case of a stellar mass BH the disc temperature will be of the order of 1 keV, while for a BH in the center of a galaxy the temperature can be thousand times less. Such discs are therefore considered cold with respect to other models which will be described in the following; and this makes them appropriate to produce the Compton reflection and fluorescent features which have a particular interest for us (see section 1.4).

For lower values of the density the disc becomes optically thin, and the radiation spectrum is then dominated by Comptonized free-free radiation (*Shapiro et al.* 1976). But such a case is thermally unstable, thus not relevant for realistic flows.

When viscosity is taken into account in a more realistic manner, the considerations become much more complicated. In general, the viscosity parameter α, together with the pressure, determines the energy and angular momentum dissipation in the accreting flow, and one can study the variations of $\dot{m}$ with varying α.

When α is taken into account in the computations of the accretion flow, the result is both a thickening of the disc ($h(r)/r \gtrsim 1$) – which becomes in fact a sort of a *torus* – and a fast switch to the unstable regime.

Finally, two branches of solutions exist in which the accretion flow is *advection dominated*.

The first branch occurs for high densities and very high (larger than Eddington's) accretion rates, when the photons are trapped in the flow. In this case the radiation pressure causes the disc to expand and become a *slim*

[6]The disc emits at each radius a blackbody spectrum at the effective temperature determined by the local dissipation rate $f(R, J)$ (in erg cm^{-2} s^{-1}):

$$\sigma T_{eff}^4 = \frac{3GM\dot{M}}{8\pi R^3} f(R, J),$$

thus the emitted spectrum will result from the integral on R (J is the BH spin). The same mass-temperature dependence can be also seen in the expression of the maximum disc temperature

$$T_{max} = T(r \sim 2r_{ms}) \simeq 10^7 \left(\frac{M}{M_\odot}\right)^{-1/4} \left(\frac{\dot{M}}{\dot{M}_E}\right)^{1/4} \text{K} \simeq 1.2(\dot{M}/M)^{1/4}.$$

Therefore $T_{\rm BHC} \sim 10^7$ K, while $T_{\rm AGN} \sim 10^5 \div 10^6$ K (cp. Treves *et al.*, 1988. Notice that $M_{Edd} = L_{Edd}/c^2$).

disc (Abramowicz *et al.* 1988). Because of such small luminosity and high accretion rate, this model could be of interest only for objects radiating near their Eddington luminosity, as it has been proposed for NL Sy-1 galaxies (see section 1.4).

The other refers, conversely, to very low densities. Such flows would have low to medium accretion rates ($\dot{m}/\dot{m}_{Edd} < \alpha^2 \sim 0.01$). Because of the low density, energy is not efficiently transferred from ions to electrons and is therefore advected into the event horizon together with the protons. A property here is that the plasma has two characteristic temperatures – say $T_e < T_p$. While the electrons can cool efficiently through free-free or synchrotron processes, the proton gas will approach virial temperatures, of the order of ~ 100 keV.

These discs can be referred to as *proper* **ADAF**s (*Advection Dominated Accretion Flow*s). However, they can differ by the cooling processes, for instance whether or not soft photons are present to induce inverse Compton (Ichimaru 1977, Narayan & Yi 1995, Abramowicz *et al.* 1995, Narayan *et al.* 1998a). Actually, for these values of the accretion rate ($\dot{m}/\dot{m}_{Edd} < \alpha^2$) there is no way to predict whether proper ADAFs or SS discs should occur: both solutions are valid, and so the choice is made only on a phenomenological base.

Much attention has been devoted to ADAFs in the last few years.[7] They are thought to be present in low luminosity objects, such as LINERs and the centers of galaxies like the Milky Way (Sgr A*), NGC 4258,[8] M87 and other ellipticals (e.g. Menou *et al.* 1997). ADAF models can be relevant to explain the X-ray emission from underluminous AGN or the "low" state of galactic BHCs (e.g. Narayan *et al.* 1998b; however, for a contrasting view on the need of ADAFs in quiescent BHC see: Nayakshin 2000b).

When an ADAF is present, the fact that a large amount of the energy is advected onto the compact object gives an important distinction between those compact objects with an event horizon – where much radiation is "lost" for the observer, as is the case of BHs – and those without an event horizon – whose surface can re-radiate the energy away. This is therefore a possible way to "discover" BHs.

However, advection-dominated accretion models are not suited to repro-

[7] Updated reviews on the subject are those by Chakrabarti (2000) and Spruit (2000).

[8] However, see Fiore *et al.* 2000 for a contrasting view on this source, based on the lack of Bremsstrahlung emission in the *BeppoSAX* data.

duce what are thought to be reflection spectra from "cold" matter, as explained in section 1.4.3.[9]

Rather, it is possible – or even likely – that real accretion flows are *bimodal*, which means that there is a transition from one to another regime of accretion in the flow itself. For instance, ADAFs are thought to be surrounded by a thin cold (SS) disc, located farther from the BH, where the cooling time is smaller than the viscous time. In this case the hot medium which makes up the ADAF can be cooled by inverse Compton scattering of the soft photons produced by the cold disc.

Such a configuration can be of importance from a phenomenological point of view, as shown in the works by Done *et al.* (1998) and Życky *et al.*(1997, 1998), who calculated both line and reflected continuum in Schwarzschild metric, with regard to some BHCs (see chapter 3). Among the authors which studied such ADAF-SS transitions, let us remember: Dullemond & Turolla (1998); Czerny *et al.* (2000), who proposed a model consisting of the accretion disc with an accreting two-temperature advection corona and substantial disc-corona mass exchange; Meyer *et al.* (2000), who in practice identify the innermost corona (produced by evaporation of the inner disc flow) with an ADAF; Gu & Lu (2000), who claim that the SS-ADAF transition is possible also for large values of the viscosity.

Following the suggestion of Blandford & Begelman (1999), various authors are now considering the possibility of *outflows* or even *winds* in the accreting matter. Blandford & Begelman called their model **ADIOS** (*Advection Dominated Inflow-Outflow Solution*). In their model, low radiative efficiency implies vanishing radial energy and angular momentum fluxes through the flow, therefore the "Bernoulli function" is positive, and winds are produced towards outside. However, Abramowicz *et al.* (2000) showed that this is not strictly required in ADAFs, since they may indeed have either positive or negative Bernoulli functions; at high viscosity, the presence of outflows still depends on various factors.

With a low viscosity prescription, convective cooling brings the energy towards outside, without need of significant matter outflows. At small values of the viscosity parameter, $\alpha \lesssim 0.1$, the dynamics of non-radiating accretion flows is dominated by convection (*Convection Dominated Accretion Flows*: Quataert & Gruzinov 1999, Quataert & Narayan 1999). Convection strongly suppresses the accretion rate, transfers angular momentum inwards and radiation from small to larger radii. The fate of this convective luminosity and form of the corresponding spectra has been addressed also by Ball *et*

[9]Nevertheless, for references to relativistic computations of spectra from ADAFs see section 3.4.

al. (2000). On the same issue of inflow-outflows, works have been recently published also by Di Matteo *et al.* (1999), Ozel & Di Matteo (2000), Turolla & Dullemond (2000), Beckert (2000).

In the field of hot accretion flows, calculations have been usually performed in a pseudo-Newtonian approximation (see Appendix). However, relativistic effects are properly accounted for through the *inner boundary conditions*, which describe qualitatively the effects very well. A completely open issue remains that of the *outer* boundary conditions, which are often taken as parameters of the model: we do not know where the outer boundary of an ADAF is, nor what happens there.

The Disc-Corona Connection

In order to account for the X-ray reflection spectra observed in real sources, a "two phases" mechanism – assuming inverse-Compton upscattering of the disc soft photons by hot electrons in a corona, and Compton reflection from the *cold* disc – has been theoretically developed by Haardt & Maraschi (1991, 1993; see also: Haardt 1994). In the initial version of this model the disc is sandwiched within an optically thin corona. But in this case the ratio between the disc thermal component and the X-ray luminosities is smaller than observed in BHCs in soft states and in high-luminosity AGN. This is why Haardt *et al.* (1994) proposed a modification, in which the corona is patchy, i.e. made up of a few blobs, that could be due to the formation of magnetic loops storing energy and releasing it rapidly through reconnection, like in solar flares.[10] Below a flare, the disc is heated up.

Signatures of a hot Comptonizing corona are common in the X-ray spectra of most astrophysical sources (e.g. Merloni & Fabian, 2000, and references therein). The process consists in the up-scattering of soft photons from the disc by the coronal plasma, which powers them up to the energies of the power-law component of the spectrum. A basic computational model for this phenomenon has been developed for Seyfert galaxies by Haardt *et al.* (1997), involving a few essential parameters: the soft photons (disc) temperature T, the reduced coronal temperature $\theta = (T_e k)/(m_e c^2)$ (which refers to electrons and positrons in the plasma), and the coronal optical depth τ

[10] A reflection component is present in the solar spectrum, too, and is due to reflection of flares by the photosphere. It is worth noticing that this may be not the only analogy between astrophysical disc-corona pictures and solar physics: the concept of *corona* itself is derived from the latter, while many issues (flares, magneto-hydrodynamical processes, seismology, and so on) are often translated by theoreticians from one case to the other.

(which includes an electron/positron contribution and a further contribution by nuclei). It comes out that the spectral index α depends on both θ and τ, while the cutoff energy does not really depend on the optical depth. The observed temperatures and optical depths lie in a narrow range of values: $0.1 < \tau < 1, \quad T = (1 \div 3) \times 10^9$ keV. Merloni & Fabian (2000) argue that this fact supports evidence for magnetically- rather than thermally-dominated coronas.

In fact, the Comptonization model is useful for both galactic BHCs and most AGN, apart from the different disc temperature – and thus ionization – involved.

Nayakshin & Kallman (2000) also considered the case of a corona overlying the cold disc. Due to additional pressure and weight acting onto the disc, the pressure and density in the accreting flow is large enough to render the gas cool and neutral. No highly ionized skin forms in such a model; if the corona is Thomson thin, then the EW of the iron line does not depend on the accretion disc or corona luminosity.

1.4 Phenomenology

In this section we concentrate on the observed properties of galactic BHCs and AGN in the X- and γ-ray energy bands. Among the sources in our sky, galactic as well as extra-galactic Black Hole candidates may be selected precisely investigating the properties of their strong X-ray / soft γ-ray emission, which originates from their innermost regions. Galactic BHCs are a subclass of X-ray binaries; most AGN emit a considerable amount of their radiation at the highest energies. Both classes show spectral features which cannot be produced by any classical stellar process: the electromagnetic radiation is so strong that it must be due to the gravitational energy release by compact objects or, more precisely, to the extremely effective conversion of gravitational energy into electromagnetic radiation by the matter accreting onto a BH. This efficiency is described by the formula

$$L = \eta \dot{M} c^2, \tag{1.2}$$

which links the luminosity to the accretion rate through an adimensional parameter η, representing the *efficiency of mass conversion*, which in the case of BHs is estimated to be in the range $0.06 \div 0.4$ - while, for instance, the hydrogen-helium fusion in the stars has an efficiency $\eta \sim 0.007$ only.

In galactic BHCs the BH mass can be of the order of some tens of the solar mass; in AGN, on the other hand, the BH must have $M \gtrsim 10^6 M_\odot$ to account for the extremely strong emission coming out. The main difference between galactic BHCs and AGN lies in the different order of magnitude of the involved masses, sizes, and distance from the observer, while many spectral properties are analogous. A peculiarity of galactic BH candidates is that they always reside in binary systems, and often show phenomena which are connected to the interaction with the companion star (transient behavior, strong variability). Some of these phenomena are common to most X-ray binaries: something analogous occurs also when the compact object is a neutron star or a white dwarf.[11]

A noticeable variability, due to changes of $\dot{m}$ and/or the accreting flow geometry, is also detected in AGN but at longer timescales, because of the different size.

Considerable work has been devoted in the past both to formation and collimation of jets, in BHCs as well as in AGN. It had been often assumed that the BH spin drives the jet production. However, recent studies indicate that the role played by the "classical" Blandford-Znajek mechanism in its original formulation (Blandford & Znajek, 1977), as a way to directly extract rotational energy from a BH to power jets, has been often overestimated. An extremely interesting review on this debate has been recently written by Krolik (2000). The original Blandford-Znajek mechanism is now hardly believed to be able to account for the strong energy outflows needed to produce jets; rather, the required magnetic field may be generated in the core region by ordered motion of accreting gas and dust. The disc magnetic field is likely to play a strong role in expelling material as well as in collimating the outflow.

This scenario is attractive because magnetically-driven jets scale easily to any size, from binaries to AGN. Magnetohydrodynamical simulations give hints on the transient nature of jets, due to instabilities in magnetic-pressure dominated discs, or magnetic "switches" due to variations in the coronal particle density.

Currently there is no way to directly measure the strenght of such magnetic fields. Moreover, it is not clear why jets are not a general feature of such systems.

It may still be true that BH spin and jet production are connected, but rather in an indirect sense: the BH spin causes the event horizon to shrink

[11] For a general discussion on X-ray binaries see for instance Longair (1994), or the volume *X-Ray Binaries*.

and the accretion disc inner edge to extend down close to the BH; this can increase soft X-ray production significantly, and very strong inflow-outflow processes may take place in the core of the system.

However, the so called *spin paradigm* which states that spinning BHs are connected with the formation of jets, and therefore to strong syncrotron i.e. radio emission, is no more such a solid assumption as it was supposed to be in the past. The fact that Seyfert galaxies, for which rotating BHs are claimed to explain broad emission lines, as we will see in the following, do not emit very much radiation in the radio band also seems to contradict the spin paradigm.

In AGN, correlations other than that between BH spin and jet occurrence are being investigated (e.g. the role of the BH mass: Laor 2000). In galactic objects, another possibility is that the occurrence of jets is related to the high mass loss rate from the nearby companion. Jets are indeed common in galactic BHCs, even more than in AGN. For galactic BHCs there are solid indications that the formation of jets is related to the accretion process.[12]

1.4.1 Galactic BHCs, Superluminals

Galactic BHCs have quite well-defined spectral properties in the X-ray band: a powerlaw tail with variable luminosity and slope is present at higher energies, while a thermal component often dominates at lower energies. However, transitions between two, or even more, spectral states, each of them characterized by the different relative importance of the various components, is very often observed.

In particular, two spectral states are commonly detected: the one is characterized by a strong soft component, probably of disc (thermal) origin, with a power-law hard tail with spectral index $\Gamma \sim 1.7$ (*high* or *soft* state); the other one shows a simple power-law spectrum with a less pronounced, or even undetectable, soft component ($\Gamma \sim 2 \div 3$, *low* or *hard* state).

This is, among others, the case of Cyg X-1, which is the best studied galactic BHC. It is also the first X-ray source whose binary nature was demonstrated, through spectroscopy. Its mass function allowed to estimate the compact object's mass to be in the range $9 \div 15 M_{\odot}$ (e.g. Celotti *et al.*, 1999). This source is usually found in the hard state, but switches occasionally to a soft state which lasts for 2 or three months. There is an interesting suggestion by Gilfanov *et al.* (2000) that *in the soft state* the reflected flux

[12] A detailed discussion on the issues of jets origin and collimation is beyond the scope of this dissertation. For more information and review on all the topics related to jets see e.g. Celotti & Blandford (2000) and references therein.

reproduces, with nearly regular response, variations of the primary emission; on the other hand, this is not the case when the source is in the hard state, in which variations of the reflected flux are significantly suppressed in comparison with the primary emission. The reflector (an optically thick AD) is probably switching in inner radius between $\sim 100m$ and $\sim 10m$ respectively in the soft and hard states, if the central BH has a mass $\sim 10M_{\odot}$.

Analyzing *RXTE* temporal data of Cyg X-1 it has been found that the relative amplitude of the reflection features (Kα line and smeared edge) decreases with increasing frequency in the power spectrum. If this behavior is solely due to a finite light crossing time, then it would imply that the characteristic size of the reflector is $\sim 150m$ (e.g. Revnivtsev *et al.*, 1999; Gilfanov *et al.*, 2000).

Characteristic processes occurring in Active Galactic Nuclei are somehow reproduced in smaller objects of stellar dimensions, which are often referred to as *microquasars*. Hosted in binary systems, they show matter ejection along bipolar jets. Because of a special relativistic effect, the matter in these jets sometimes has apparent velocities greater than c, and thus the sources are called *superluminal*. There are three of such objects in the sky, namely GRS 1915+105, GRO J1655-40 and the more recently discovered XTE J1748-288. GRS 1915+105 was the first observed galactic source of this kind. Its superluminal radio expansion was reported by Mirabel & Rodriguez in 1994. We are going to deal with this source in detail in section 4.5, showing results of relativistic fits of its iron fluorescent line emission.

Confirmation that an extremely hot disc, even if not stable, resides in the microquasar would be extremely important because an unusually high disc temperature may be explained by the BH rotation, which makes the disc extend closer to the BH, hence be hotter. If interpreted according to the standard accretion disc prescription of Shakura & Sunyaev (1973), where $T[\mathrm{keV}] = 1.2(\dot{M}/M)^{1/4}$ (cp. section 1.3.1), the temperatures observed in some cases[13] would correspond to a mass of the central object much less than 1 $M_{\odot}$. Such a low mass, however, seems unacceptable given the high luminosities. Thus, either a different cooling process is active in such microquasars, or the assumption of the last stable orbit at the Schwarzschild's BH value of $6m$ is not valid: the disc extends more inside (see Greiner 1999, §4, for more practical examples).

Thus, indications that superluminal sources may host rotating BHs are

[13] 2-3 keV, in the case of GRS 1915+105. For this source cp. the careful study of the bright soft X-ray emission, made by Zhang *et al.* (1997), who infer the presence of a rotating BH at its center. See also section 4.5.

independent of the occurrence of jets. As we will better see in section 1.7, rotating BHs could account also for certain types of QPOs observed in some microquasars (Cui *et al.* 1998).

1.4.2 AGN

The systematic research and classification of active galaxies started with the discovery of *quasars* in the early 1960s (Hazard et al. 1963; Schmidt 1963). The current astronomical literature discusses observational properties and theoretical models of AGN and related objects (Weedman 1986), and it turns out that the most massive black holes are expected to reside inside AGN. These are the criteria used in order to classify an extragalactic object as an AGN (Miller 1985; Woltjer 1990):

- Radiation of the object is strongly dominated by its compact nucleus;
- Strong nuclear continuum emission is present; nuclear emission lines are excited by non-stellar continuum radiation, or some other additional processes;
- Continuum and emission lines are variable.
- Outflows in the form of collimated jets emanate from the nucleus.
- Extended radio lobes are developed well outside the optical counterpart of the object.

An AGN must satisfy at least some of the above-mentioned conditions. Although a discussion of the various classes of Active Galactic Nuclei, and the related unification models, is beyond the aims of this work, it is important to keep in mind some basic criteria used for their classification.

The key distinction among AGN is determined by their emission in the radio band: there are radio-loud and radio-quite objects. The radio-loudness is due to synchrotron emission from accelerated plasmas, thus to strong outflows (*jets*). However, radio-loud objects, showing such violent phenomena, are much less frequent (about a tenth) than the radio-quiet.

In the following we will essentially consider the subclass of radio-quiet AGN hosted in spiral galaxies with a pretty regular morphology, called *Seyfert* galaxies [**Sy**] (Seyfert 1943).

The standard unification model stresses the effect of the galaxy's inclination with respect to the line of sight (Antonucci 1993). There are *type I* sources and *type II* sources. Type I sources do show broad emission lines in their spectra, which most likely arise in the innermost part of the system

(*Broad Line Region* – **BLR**), where strong velocity fields are present. Type II sources do not show such features, probably because direct observation of the BLR is impossible to us due to obscuring material on the line of sight. The basic unification model assumes that the obscuring material is distributed equatorially and with axial symmetry in a sort of a *torus*; objects of type II are seen edge-on, while objects of type I are seen pole-on, thus showing their core regions directly to us.

Seyfert galaxies can be divided into such sub-classes: *Sy-1*'s are those in which *broad* (velocities of thousands km s^{-1}) emission lines can be observed, while in *Sy-2*'s, which are less bright, only *narrow* (hundreds km s^{-1}) lines can be seen. In X-rays, Sy-2's are heavily absorbed by neutral matter, largely in excess of the Galactic one. This indicates that obscuring material, probably located in a *torus*, hides the nucleus to our observation. Therefore Sy-2's are not well suited to our investigation of relativistic spectral features.[14]

The Sy-1 / Sy-2 dichotomy is thus traditionally interpreted on the base of the orientation with respect to the observer, possibly combined with further effects due to obscuring material. If the column density of such material is equal or larger than the inverse Thomson cross section – i.e. $n_H \geq \sigma_T^{-1} = 1.5 \times 10^{24} cm^{-2}$ – then the galaxy is told to be a *Compton-thick Sy-2*. Recently, a refinement of the unification model for Seyfert galaxies has been proposed (Matt 2000b) in which Compton-thick Sy-2's are those sources observed through compact thick matter (torus) while Compton-thin and intermediate Sy's are obscured by dust lanes at larger distances.

Seyfert galaxies have bright cores, often with strong emission lines in the optical and X-ray bands. The hosting spirals are still observable, and this makes the historical difference with the so-called *Quasi Stellar Objects* [**QSO**s].

The analogous of Sy-1 galaxies in the context of *radio-loud* AGN are the Fanaroff-Riley of type 1 and the Broad Lines Radiogalaxies.

[14] Further sub-classes have been introduced for the Seyferts: *Narrow Line Seyfert 1* galaxies (**NLSy-1**) show extreme soft X-ray excesses and large variability. Among other possibilities, it has been supposed that they have accretion rates close to the Eddington limit - which means, for a given luminosity, smaller BH masses when compared with the other Seyferts (Wandel 2000, Mathur 2000) - and perhaps slim ADs (Mineshige *et al.* 2000). *Intermediate* Seyfert types (Sy-1.5, Sy-1.8, Sy-1.9) have been classified on the base of their emission line spectrum in the optical band, which is not relevant to our present aims.

1.4.3 Common X-Ray Properties of AGN and BHCs

Let us now summarize the properties of X-ray and γ-ray spectra of AGN and BHCs.[15]

In the soft X-ray band a *soft excess* can be observed. This is more common in the case of BHCs, while its peak resides at lower energies in the case of AGN ($\sim$ 10 eV). It can be due to thermal emission from the AD, therefore is detected especially in the case of galactic objects because the disc temperature has an inverse dependence on the BH mass (see section 1.3.1).

In AGN, this emission may be related – when seen from the optical-UV "perspective" – with the *Big Blue Bump* (**BBB**).

Actually, it is likely that the soft excess in AGN is a mixture of different contributions (e.g. reflection by ionized matter) which may or may not be present simultaneously (e.g. Piro *et al.* 1997). A few absorption features imprinted on the X-ray emission of AGN – edges due to oxygen and other ions, resonant absorption lines – are supposed to be due to a *Warm Absorber*, i.e. to ionized matter on the line-of-sight. However, these spectral features are not relevant to our aims, so we will not deal with them any further in the present work.

A common feature in the spectra of both AGN and galactic BHCs is a continuum *power law* emission, with index $\Gamma \simeq 2$ in AGN (Pounds *et al.* 1990, Nandra & Pounds 1994), and variable in the range $1.5 \div 3$ in BHCs (see section 1.4.1), which is thought to be the result of inverse Compton scattering of thermal photons in a hot corona, although the characteristics of the plasma and the radiation field are yet under investigation. This component is visible up to a *cutoff* energy of some tenths, or a few hundreds, keV. In the following we will call it *primary flux*.

Initially discovered by *Ginga* (Pounds *et al.* 1990, Matsuoka *et al.* 1990), an additional continuum emission (a "hump", up to some hundreds keV) is observed in most AGN spectra. When added to the primary component, this hump hardens the total spectrum above a few keV and steepens it above a few tens of keV. The shape of the reflected component is determined by the competition between photoelectric absorption (whose cross section depends on the energy, after each photoabsorption edge, as $\propto E^{-3}$) and Compton scattering (with a more or less constant cross section, at least up to a few tens of keV). The two cross sections are equal at about 10 keV if the matter is neutral (see next section) and the elemental abundances are close to the

[15] For a review of observed spectra see e.g. Zdziarski (1999).

cosmic values.

Some discrete features are also imprinted onto the reflection hump: they are the *iron lines* Kα and Kβ and an iron *edge*. A straightforward explanation is that the hump as well as the discrete features have the same origin in "cold" matter – as would be the case for a SS disc – which is illuminated by the primary continuum (power-law) flux and reflects it through Compton scattering and – in the case of the lines – by fluorescence.

This interpretation is consistent with the fact that Compton reflection and broad fluorescent lines are less common in galactic BHCs, whose AD is much hotter and therefore substantially ionized. In the next section we deal in more detail with the fluorescent features, which are crucial for our relativistic computations (chapter 3).

The reflected radiation features from the disc (continuum, iron lines and edge) had been predicted by Guilbert & Rees and by Lightman & White in 1988 in a first rough, "lamp-post" picture including a primary source which illuminates a "cold" disc.

Some issues on the continuum components remain open.

Zdziarski *et al.* (1999) found a correlation between the power law index Γ and the amount of Compton reflection R. Even if evidence of this correlation may be strengthened by a similar correlation found between Γ and the iron line EW (Lubiński & Zdziarski, 2000), the result gave rise to a controversy concerning the fact that the parameters Γ and R cannot be simultaneously estimated independently of the model used.

Other open issues concern the occurrence of the soft excess in Seyferts, and the typical (if any) cutoff energy in the hard X-ray spectra. For a summary of the current understanding on these points see e.g. Matt (2000).

To conclude, it may be worth mentioning a couple of cases in which the $e^+ - e^-$ annihilation line at 511 keV (i.e. not in X-rays, but in the γ band) has been detected in BHCs, because this feature can be a diagnostic of Kerr spacetime in the same way of the Kα line of iron we are going to deal with in detail all through this work.

A line at 481 ± 22 keV has been seen in Nova Muscae, an X-ray transient, and another one at 480^{+96}_{-72} keV in the spectrum of 1E 1740-29, a strongly variable X-ray source, both by the *SIGMA* experiment which, however, could not determine their profile because of the low energy resolution.

In the case of Nova Muscae a peak at ~ 200 keV has also been detected. This could be the "red" horn of the relativistically-distorted feature. In the other source no second peak has been detected, which may mean that the

inclination is small (Hameury *et al.*, 1994; see section 3.4).

1.5 The Fluorescent Lines

We now discuss the issue of the fluorescent lines which are produced along with the Compton reflection in a "cold" disc, and constitute probably the best diagnostic of relativistic effects taking place in such systems. Here we also intend to review the status of the observations, both in AGN and BHCs. A subsection is devoted to alternative interpretations of the iron line profiles. For more detail on the subject of broad iron lines observed in AGN see e.g. Fabian *et al.* (2000).

Line Formation

Kα lines arise by fuorescence, i.e. emission after photoelectrical absorption, in the transition from the L ($n = 2$) to the K ($n = 1$) shell. The Kβ corresponds to the transition from the M ($n = 3$) shell.

For X-ray astronomy, the most relevant case is that of iron. Its Kα feature has a rest energy equal[16] to $E_\alpha = 6.4$ keV, while the Kβ is at 7.07 keV. Of course, the photoionization can occur only if the incident photons have an energy above the ionization threshold, which for the K shell is immediately after the Kβ at 7.1 keV (K *edge*). There is also a Nickel Kα feature at 7.5 keV (see Figure 3.3).

These values hold for neutral matter. At higher ionization states, the outer electrons are less effective in screening the nuclear charge, so the energy gaps between the shells increase: for FeXXVI, that is the hydrogen-like ion, Kα rest energy reaches 6.97 keV. The probability that a Kα photon is emitted by fluorescence (recombination, in the case of FeXXV and FeXXVI) depends also on the ionization state. For neutral iron, this probability is equal to 0.305, in a 150:17 proportion with the similar probability for $K\beta$: therefore the latter results to be 9 times weaker (see Matt 1992, and references therein).

[16] In fact, there are two components of the iron Kα line, at 6.391 and 6.404 keV respectively, but they cannot be resolved by the current detectors, and will not be considered separately in our discussion.

Line Width and Intensity

The line broadness which is usually observed in AGN and BHCs is substantially greater than the instrumental resolution and cannot be solely of thermal origin: the line at rest has $\Delta E \sim 1$ eV, and at the typical disc temperatures one can expect at most $\Delta E \lesssim 5$ eV. It is therefore likely that this effect has kinematic and/or gravitational origin.

General-relativistic effects on the profiles have been assumed and modelled first by Fabian *et al.* (1989).

When well-resolved line profiles are not available, it may be very useful to explore the integral characteristics of the spectral features. Namely, a crucial point to address is that of the *equivalent width* (**EW**) of such lines, i.e. the line intensity relatively to the underlying continuum flux:

$$\mathrm{EW} = \frac{\int F_{\mathrm{line}}(E)\mathrm{d}E}{F_{\mathrm{cont}}(E = E_{\mathrm{line}})}, \tag{1.3}$$

where the underlying continuum can be intended either as the direct (primary), or as the Compton-reflected one, or as the sum of the two i.e.

$$F_{\mathrm{cont}} = F_{\mathrm{dir}} + F_{\mathrm{ref}}.$$

E_{line} is the rest energy of the line, i.e. 6.4 keV for the iron Kα.

The iron line EW depends on the disc inclination with respect to the observer, and – assuming an isotropic primary emission and a solid angle subtended by the matter with respect to the primary source equal to 2π – its value can vary between 0 (edge-on disc) and ~ 150 eV (face-on disc; George & Fabian, 1991; Matt *et al.*, 1991). If relativistic effects in Schwarzschild metric are included, the maximum value for EW is expected to rise up to ~ 160 eV (Matt *et al.*, 1992). However, the observed iron line EWs do often remarkably exceed – even by a factor 2 or 3 (e.g. Mushotzky *et al.* 1995, Nandra *et al.* 1997a,b) – the previous limits. A possible way out of this problem is in terms of iron abundance (Basko 1978; George & Fabian 1991; Matt *et al.*, 1997), which is evaluated with respect to the other elements – O, Ne, Mg, Si, S – which possess a non-negligible photoelectric cross section at E =6.4 keV. Other hypotheses are based on a possible anisotropy of the primary radiation illuminating the disc (e.g. Ghisellini *et al.* 1991; Haardt 1993) and/or on the disc matter ionization (Matt *et al.*, 1993).

Our computations (Martocchia & Matt 1996, see section 3.5) suggest that an alternative explanation is possible: even if the primary source emits isotropically in its own reference frame, the strong spacetime distortion in the very vicinity of the BH causes an anisotropic illumination, such that most

of the emission is originated in the innermost part of the disc. This effect becomes more and more important if the BH is spinning, as we will see in section 3.5.

Undoubtedly, the EW strongly depends on the iron abundance (e.g. Matt *et al.* 1997), but the other integral parameters of the line do not. Moreover, the reflection component depends on the iron abundance in an easily recognizable way, i.e. changing the depth of the iron edge (Reynolds *et al.*, 1995). Therefore one can hope to separate the influence of iron abundance from other effects.

Strong constraints have been derived in the case of MCG–6-30-15 (Lee *et al.*, 1999).

A puzzling property of the observed Kα line EWs in Seyferts is their apparent anticorrelation with the *X-ray luminosity*. This property, which has been originally called "X-ray Baldwin effect" to underline the similarity with an optical effect in quasars (Iwasawa & Taniguchi 1993), may be due to ionization of the disc matter by the primary source (Nandra *et al.* 1997b; a review in Nandra 1999). The correlation between EW and *X-ray slope* in Seyferts has been studied, too (e.g. Lubiński & Zdziarski 2000, and references therein).

Observations

The Kα iron line is a very common feature in the high-energy spectra of both AGN and BHCs, and has become the subject of accurate investigations especially after the *ASCA* detection of the broad, double-peaked profile in the source MCG–6-30-15 (Tanaka et al. 1995), suggesting that general-relativistic effects are playing a role in distorting its shape. There are many objects which show a "broad" Kα line – i.e. broader than the instrumental resolution ($\Delta E \sim 100 \div 200$ eV). In AGN the fluorescent iron line had been detected for the first time in the radiogalaxy Centaurus A (Mushotzky *et al.*, 1978); afterwards, more and more broad Kα features were discovered in X-ray sources, and the Kα emission was found to be extremely common in Seyfert galaxies (Nandra & Pounds 1994; Mushotzky *et al.* 1995; Yaqoob *et al.* 1995; Eracleous *et al.* 1995; Iwasawa *et al.* 1996a).

Nandra *et al.* (1997a) and Reynolds (1997) used *ASCA* data to study the iron line in more than 20 Sy-1 galaxies, and found that most of them are significantly broader than the instrumental resolution. However, in some of these objects narrow lines may also be present, which are likely emitted by more distant matter, for instance in the torus (e.g. Matt 2000).

Sy-2 galaxies also possess iron Kα line profiles indicative of face-on discs (Turner *et al.* 1998): the mean inclination derived for the sample of Sy-2s does not differ from the mean inclination angle of Sy-1s, which is a problem for the standard unification scheme of AGNs (Antonucci 1993, cp. section 1.4.2). However, Weaver & Reynolds (1998) showed that fitting the spectra with an additional, narrow line at 6.4 keV (presumed to arise from the obscuring torus) the medium inclination for such objects can be up to ~ 50 degrees.

The iron line variability observed in NGC 7314 (Yaqoob *et al.* 1996) seems to be exactly what is expected from a line consisting of a disc broad component and a torus narrow component. In this source, the broad line responds to changes in the primary power-law flux while the narrow line is constant.[17]

In Compton thick Sy-2's the line also has a significant narrow component, which originates from matter far away from the central BH (Weaver & Reynolds 1998; see also Matt *et al.* 2000, and references therein).

Sulentic *et al.* (1998b) raised the problem of the disagreement between the inclination angle derived for the iron line and that from the Hα and Hβ lines. In a large sample of objects, the position of the line centroid at 6.4 keV is not consistent with the random orientation of the disc with respect to the observer (Sulentic *et al.* 1998a).

It has been suggested that in *low luminosity AGN* the accretion rate is smaller than in Seyferts. In this case ADAFs or slim discs are thought to be at play. As explained in section 1.6, such accretion modes are not expected to produce much fluorescent iron line fluxes. However, the main problem with low luminosity AGN is that they are faint in the X-ray band, and their spectra are typically complex because of non-nuclear spectral components (starburst regions, hot regions,...), thus line detection is difficult. Nevertheless, interestingly an iron Kα feature has been detected for instance in NGC 4258 (M106) (e.g. Reynolds *et al.*, 2000). Similar difficulties in detecting iron lines are experienced in radio-loud objects.

It is less common – but still not impossible – to find a Kα emission feature in a BHC spectrum. This may be due to the fact that in these systems the matter is much hotter, thus substantially ionized, so that resonant reabsorption of the fluorescence photons takes place (Ross & Fabian, 1993; Matt, Fabian & Ross, 1993). Therefore X-ray reflection produces here weak line emission but strong absorption edges; sharp features are also smeared as a result of Doppler and relativistic effects, as is probably the case for Cyg

[17] On iron line variability see section 1.7.

X-1, Nova Muscae and V404 Cyg (Życki *et al.* 1999, Done & Życki 1999, Young *et al.* 1999).

Apart from these sources, whose relativistically smeared spectra have been carefully studied by Życki *et al.* (1999, and references therein), galactic BHCs in which iron lines have been detected are the microquasar 4U 1630-47 (Cui *et al.*, 1999), and the superluminal sources XTE J1748-288 (Miller *et al.*, 2000) and GRO J1655-40 (Balucinska-Church & Church 2000).

Recently, we discovered iron line emission in the *BeppoSAX* data of the well known superluminal source GRS 1915+105: one of the final sections of this work is entirely devoted to its study.

1.6 Alternative Interpretations

The fact that strong broad, probably relativistic lines and blue "humps" are actually observed in some sources gives strength to the assumption that the accreting matter is optically thick. On the base of such observations, hot discs, and ADAFs in particular, seem not to be suited to produce those spectral features. But still there are viable hypotheses to be taken into account which deviate from the standard picture and can solve some open issues.

First of all, let us remember some sceptic points of view about the relativistic nature of the broad iron lines.

In some cases, an apparently broad line could be produced by an interplay of different components, as explained also in the previous section. Zdziarski *et al.* (1996) showed that, at least for one source, NGC 4151 (see section 4.2), the broad line may be an artifact due to a complex continuum. Referring to Seyfert galaxies, Sulentic *et al.* (1998c,a) modelled the iron line as the sum of two features with Gaussian profiles, one narrow (unshifted) and the other broad (redshifted). A similar model could explain some broad, double peaked AGN Balmer line profiles.

Weaver & Yaqoob (1998) and McKernan & Yaqoob (1998) suggested that in MCG–6-30-15 obscuration (i.e. occultation of some part of the system) can explain variations in the line profile without implying any variations in the intrinsic flux.

Fabian *et al.* (1995) considered several different kinds of mechanisms for the broadening of the line and concluded that none of them was satisfactory, thus strengthening the hypothesis of emission from a cold inner disc. In particular, they considered line production in an outflow or jet, superposition of

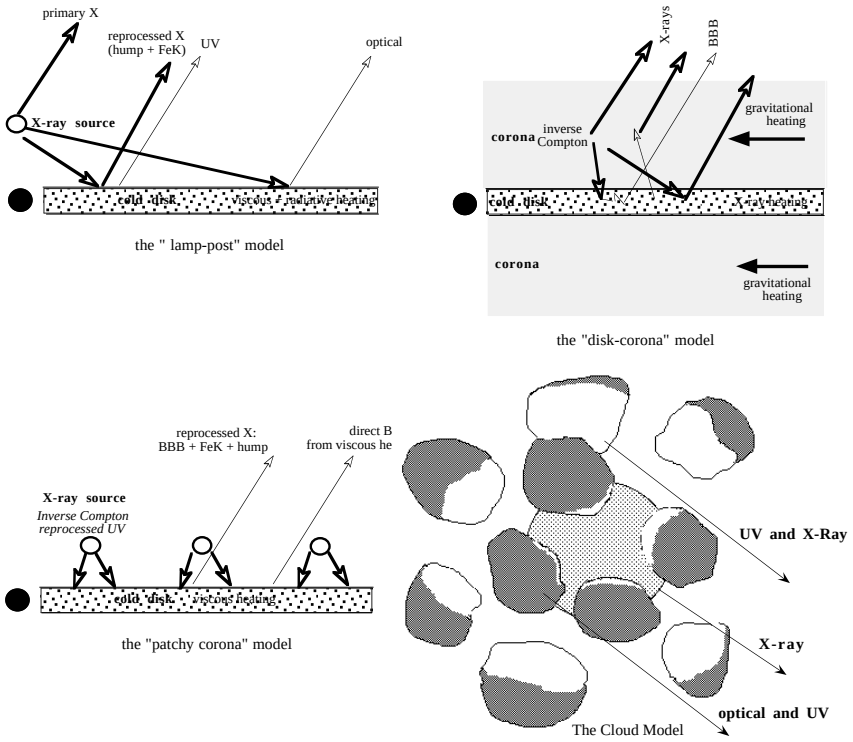

Figure 1.1: Models for the UV-X emission from central regions of accreting BH systems. The simplest version of a cold, X-ray irradiated disc is designated as *lamp-post model*: this scheme is the most relevant one for the present work. More refined models, also shown in this figure, consider the existence of an extended corona above the disc. Many observational properties of disc-corona models can be investigated with the simplified lamp-post scenario, too. The cloud model, on the other hand, relies on Comptonization as an important factor influencing the line formation. From Collin *et al.* (2000).

features from matter in different ionization states, and models where the line is intrinsically narrow or even absent, but a complex underlying continuum mimics its broad shape. These hypotheses were found to be either unphysical or not reproducing the observed spectra.

Another model considered by Fabian *et al.* is based on Compton down-scattering in a surrounding medium, and therefore can be called *(iron line) Comptonization model.*[18]

In the Comptonization model the line is intrinsically narrow because it is emitted at tens of gravitational radii, but enlarged by Compton scatterings experienced by the line photons when crossing a thick medium (*Comptonization by transmission*). Czerny *et al.* (1991) stated that in this case one can explain the observed broad profile if the electron temperature in the Comptonizing cloud is less than 0.25 keV and the gas has an optical depth around 5. An upper limit to the temperature of the Compton cloud comes from the fact that the iron Kα line photons need to be primarily *down*scattered rather then upscattered (Misra & Kembhavi 1998, Misra & Sutaria 1999). Another relevant point is that, in order not to get large photoelectric edges, the region is required to be highly ionized, i.e. the iron must be stripped of all its electrons.

Fabian and collaborators found this model unsatisfactory because:

a) For the medium to be highly ionized the region should be small and very near to the BH ($r < 10^{14}$ cm), which would render gravitational effects dominant anyway.

b) Other X-ray spectral features would be altered by such a covering medium. Misra (1999) remarks that multiple Compton scatterings would produce a break in the primary power-law continuum at approximately $E \sim m_e c^2/\tau^2$, i.e. $30-40$ keV, while *BeppoSAX* observations constrain the location of the continuum break at energies greater than 100 keV (e.g. Guainazzi *et al.* 1999; see also Matt 2000). Moreover, blackbody photons originating in the same matter where the narrow line is produced would follow analogous paths through the system and should thus be affected in the same way by Comptonization (Reynolds & Wilms, 1999).

c) The Compton temperature of this cloud would be $\gtrsim 0.25$ keV, which

[18] A motivation for this alternative picture resides in the possibility of explaining how the observed line flux stays constant while the underlying X-ray continuum varies, as claimed for some sources. The absence of short-term variations would imply that the line is emitted farther away from the BH, while the primary X emission comes from the innermost region. Another issue which could be clarified is: why such a large time delay between the X-ray and the UV flux variations is observed, and why in some cases the UV light curve lags behind the X-ray one, and the opposite in other cases.

is inconsistent with the upper limit on the temperature obtained from the profile.

Another problematic issue is that the presence of a Comptonizing cloud would raise questions regarding its dynamical support, stability, geometry and origin.

Nevertheless, some Authors further developed the Comptonization model showing that an emission feature can be broadened and red-shifted, with a sharp blue drop, due to the subsequent down-scatterings in the cloud. However the resulting, broad line profile is not similar to the double-peaked one which is expected from inner disc emission. The presence of a two-horn structure is a clear sign of inner disc emission influenced by Doppler and gravitational effects, perhaps just broadened by Comptonization (for spectral fits see: Ruszkowski & Fabian, 2000).

Misra & Kembhavi (1997) took the case of the most famous broad iron line ever detected, that in the *ASCA* spectrum of MCG–6-30-15, and put it in connection with a highly ionized cloud with radius 10^{14} centimeters – i.e. about 300 Schwarzschild radii – and temperature ~ 0.21 keV. The authors stated that both effects (the relativistic and the Compton distortions) may concur in this case.

This Comptonization-by-transmission model has been the subject of recent criticism by Reynolds & Wilms (1999), who in particular addressed the version of Misra & Sutaria (1999). They applied observational constrains for MCG–6-30-15 and NGC 3516, and found that the model is ruled out on the base of the data, apart from a very small region of the parameter space in the case of the second source. In particular they analyzed the continuum variability timescale and the absence of an observed soft excess, concluding that the constrained model requires a continuum source which violates the black body limit.

Even more recently, Ruszkowski *et al.* (2000) focused the attention on MCG–6-30-15 and showed that the Comptonization model has problems with simultaneously fitting the red tail and the core of the line, and that the UV power required to cool the Comptonizing cloud would exceed the Eddington limit; in particular, the best-fit Thomson depth would imply a continuum break at ~ 16 keV, which is not observed.

A more elaborated version of the Comptonization model has been proposed by Collin-Souffrin *et al.* (1996) and developed by Abrassart & Dumont (1998), Abrassart (1999), and further by Karas *et al.* (2000), who included the gravitational and kinematical effects. In their picture a set of individ-

ual Comptonizing clouds is taken into account, with almost spherical orbital motion around the center. The primary X-ray source is just supposed to be in the middle of the system, while both the line formation – by the inner, irradiated surfaces of the clouds – and its subsequent Comptonization occur in the clouds (*Comptonization by reflection*). This can be the case, for instance, if the innermost part of the disc is disrupted due to disc instabilities. However, in this scheme the very presence of a cold disc is not requested any more. Both the iron line and the thermal continuum would come from the Comptonizing cloud itself. Moreover, the Comptonizing medium could be identified with the Warm Absorber, too (e.g. Collin *et al.* 2000, and references therein).

The Comptonization-by-reflection model does not require a very high degree of ionization, thus the Lyman discontinuity and all edges are "erased". The temperature of the clouds is of the order of 10^5 K, so they can be the source of the BBB, too.

In Karas *et al.* (2000) the clouds follow planar orbits departing from the equatorial plane of the disc. Their excursion is limited by a maximum angle of deflection θ_m, while their self-obscuration depends on their dimension, varying from pointlike to finite. The scenario is simplified, of course, in the sense that the cloud distance is kept fixed, as a sort of (quasi)spherical surface surrounding the hole; gravity is treated in a pseudo-newtonian approach; no lensing is taken into account (no GR). But nevertheless the picture is accurate and allows to estimate the effects of varying θ_m as well as the self-obscuration; the local spectra (intrinsic line profiles) are carefully computed for different ionization assumptions, too, through a Montecarlo code (Abrassart 1999). Notice that a large ionization is required. Recently, this scheme was developed further by considering also the radial distribution of the clouds and by constraining some of their physical properties (Hartnoll & Blackman 2000b).

What comes out is that a double peaked profile can be reproduced for low deflection angles (almost disc-like distribution of the clouds) and low self-obscuration. Moreover, variability can be modelled quite naturally due to changes in the parameters and transient self-obscuration.

Finally, it is worth mentioning the hypotheses that the line be indeed an iron, relativistic distorted feature, but that the geometry of the emitter be quite different from the usually assumed one: the feature could be produced by illuminated clouds or filaments (Guilbert & Rees, 1988), in some jet-like or outflow configuration (e.g. Wang *et al.* 2000, and references therein) or bicone (Sulentic *et al.*, 1998b; e.g. the latter also for more discussion on alternatives to the iron Kα disc emission model).

However, such pictures should be fine-tuned in order to avoid the occurrence of blue-ward emission, which is not observed.

1.7 Variability

To conclude this part on phenomenology, we now summarize briefly some variability properties of AGN and BHCs. Variability is related to the accretion process, thus can also be an excellent diagnostic for testing the presence of a BH.[19]

Roughly speaking, variability can be of two kinds: *irregular*, when it is due to flares of magnetic origin, thermal instabilities and other non-steady phenomena; or *periodical*, that is linked to the disc and BH rotation, or system dynamics in general.

Processes of depletion and refilling of some disc region can happen again and again, even regularly, or be just transient and unpredictable. They can be accompanied by changes in the characteristics of the corona, including its geometry, density and optical thickness. In the case of galactic microquasars, all these changes bring to drastic variations of the spectral state and intensity of the source, as already mentioned in section 1.4.1. A dramatic example, under this account, is given by the source GRS 1915+105 (section 4.5).

The disc-corona picture itself (section 1.3) can in principle be tested not only by spectral properties, but also through variability studies.

An important diagnostic for accreting BH systems may be given by the behavior of the iron line and reflected X-ray continuum fluxes in response to variations of the primary flux (*reverberation*: see also section 3.4). If we think of a primary X-ray source located above the disc, we expect that its variations be followed by variations of the radiation coming from the illuminated disc. It is also possible that the source is localized in some small region, but the illuminated disc surface is much more extended, and in this case rapid primary X-ray fluctuations would be erased by the effect of different light travel times towards the disc and from the disc to the observer.

The iron line in AGN is expected to vary in response to the continuum fluctuations with a time lag $\sim 500(r/r_g)\ (M/M_\odot)10^{-7}$ seconds, as inferred from the system's dimensions.

[19] An *RXTE* survey of the overall long-term variability in the 2–10 keV band relative to nine Sy-1 objects - including MCG–6-30-15, NGC 3516 and NGC 4151 - has been given by Markowitz & Edelson (2000). However, in this Thesis we do not focuse attention on the overall (bolometric) variability, but rather on the relative variability of the various spectral components in that energy band.

However, the reflected features and possibly also the thermal (UV-optical) light curves should always lag behind the X-ray one, while the opposite is sometime observed, for instance in the case of NGC 7462.

While the primary radiation can vary on timescales $T \sim 10^2 \div 10^3$ seconds, in general this variation is not followed by the iron line flux. On the contrary, there is often a complex and surprising behavior of the line versus the underlying continuum, as seen in the case of a few objects which have been monitored by *RXTE* and *ASCA* in recent years (see section 4.3). Some strange behaviors can be perhaps explained using alternative disc-corona pictures; however, this study requires more solid observational evidence combined with fully-relativistic computations of both the primary and reflected radiation.

Disc reflection both in the common lamp-post and in the magnetic flares pictures has been described by Nayakshin *et al.* (1999) and Nayakshin (2000a). They found that because of the difference in the ionization structure of the illuminated material in the two pictures, the line EW *increases* with the primary X-ray luminosity in the first, and *decreases* in the second case. Some observed behaviors in AGN led the authors to suggest that the evidence is thus in favor of magnetic flares as sources of the primary radiation: the line EW in this case *anticorrelates* with the X-ray luminosity.

Very recently, a sample of 15 Sy-1 galaxies has been analyzed carefully by Weaver *et al.* (2000) using *ASCA* data, in the attempt to determine the properties of the iron line variability and its correlation with the continuum flux. Using the line centroid energy, intensity and EW as indicators of the changes, line variability was registered in 2/3 of the sources. However, in most cases the line does not appear to track changes in the continuum; moreover, on the short timescales the behavior is complex, with some portions of the profile responding to the continuum and other not, which makes it difficult to use the reverberation diagnostic. On the basis of their analysis, Weaver *et al.* conclude that in some cases the simple disc model for the line production may be inadequate to explain the data.

Periodic and Quasi-Periodic Variability

In an accretion disc, it is reasonable to imagine that some localized, co-rotating structure arises from turbulence, like a hotter (or colder) spot or region – vortices, for instance – or spiral patterns, which can be induced in the gas by non-axisymmetric perturbations of the gravitational field, e.g. by

a satellite. In the latter case, a number of spiral arms arises naturally from such interactions, depending on the type of perturbing forces acting on the disc (see Karas, Martocchia & Šubr, 2000, and references therein).

Semerák *et al.* (1999) also concentrated their attention on the issue of sources with periodical variability, in the attempt to constrain the parameters of the BH which could be hosted in them.

In general, the variations of spectral and timing parameters (in particular those of the soft spectral component) are sometimes correlated to the variations of the QPO centroid frequency.

*Quasi-Periodic Oscillation*s [**QPO**s], especially those occurring at kHz frequencies recently discovered by the Rossi X-Ray Timing Explorer (e.g. Van der Klis 1998), have important general-relativistic implications. In particular, some of them may prove the relativistic Lense-Thirring precession, around NSs as well as around BHs, and a new way of measuring the BH spin. The QPO models that invoke magnetic effects for LMXRBs do not apply to candidate BHs, because of the less importance of the magnetic field, which is mantained by the accretion disc, in such systems.

The story begun in the 1980s when systematic broad power spectrum analyses were performed using *EXOSAT* data. Broad peaks ($\Delta\nu \sim \nu$) with centroid frequencies of $5 - 50$ Hz were discovered in some BHCs.

The structures disappeared only after thousands of cycles, but usually reappeared soon.

An important development came through the *RXTE* satellite, with a time resolution of the order of a fraction of millisecond. It discovered that in various LMXRBs there are two peaks (*twin peaks*) which vary their centroid frequencies more or less in an identical manner, so remaining at a fixed distance $\nu_0 = \nu_2 - \nu_1$ from each other. This distance is very stable and can be very small. The current picture says that the effect is determined by two frequencies beating: that related to the rotation of the compact object and that connected to the Keplerian disc velocity.

If one considers a particle moving circularly in a non-equatorial plane around a rotating NS – but the same actually holds for a BH – GR predicts that the compact object rotation induces a prograde precession of the orbital plane. Stella & Vietri (1998) considered the beat frequency model for kHz QPOs in LMXRBs and proposed to interpret the low frequency QPO at 10 kHz as the Lense-Thirring precession (Lense & Thirring 1918, Wilkins 1972) of the disc inner edge – tipically, the last stable orbit. The nodal precession frequency is equal to

$$\nu = \nu_{orb} \frac{\Delta\Omega}{2\pi}$$

where ν_{orb} can be taken as the Keplerian orbital motion frequency

$$\nu_{orb} = (1/2\pi)(GM/r^3)^{1/2}$$

and $\Delta\Omega$ is an angle by which the nodes of a circular orbit are dragged per revolution. In the weak field limit this angle is equal to $2(\mid a \mid /c)(GM/r^3)^{1/2}$, and thus

$$\nu_{LT} \simeq \frac{GMa}{\pi c^2 r^3}$$

or

$$\nu_{LT} \simeq 6.45 \times 10^4 \mid a \mid (\frac{M}{M_\odot})^{-1}(\frac{r}{r_g})^{-3}\mathrm{Hz}.$$

In the case of a spinning BH, the accretion disc can extend very close to the event horizon, where the weak field approximation cleary breaks down. The exact problem has been solved analytically by Wilkins (1972), to derive the allowed ranges for the constants of motion (defined in chapter 2). Then, for a given a, it is no longer true in general that $\Delta\Omega$ depends only on the orbital radius. The expression of ν_{orb} is also more complicated (Bardeen *et al.* 1972). Cui *et al.* (1998) plotted the results derived in a fully-relativistic treatment for ν_{LT}: as expected, strong-field effects are important only for maximally spinning Kerr holes.

Phenomenologically, this idea has been applied to a number of BHCs,[20] even if on the basis of a very simplified disc model, as a possible diagnostic of the relativistic dragging of inertial frames in Kerr metric (Cui *et al.* 1998). The BH mass could be estimated dynamically in some cases. These QPOs, observed in the frequency range of a few to a few hundred Hz, tend to be relatively stable in their centroid frequencies.

By comparing the computed disc precession frequency with that of the observed QPO, the BH angular momentum can be estimated. For GRS 1915+105 and GRO J1655-40 this estimate is near to the maximal Kerr value. In general, the fact that only low-frequency QPOs have been detected in BHCs is consistent with the presence of only slowly rotating BHs in these systems.

[20] They are: GRO J1655-40, GRS 1915+105, Cyg X-1 and GS 1124-68. In Cyg X-1 the highest QPO frequency is $\sim$ 9 Hz, in GRO J1655-40 it is $\sim$ 300 Hz.

Chapter 2

Forms and Properties of the Kerr Metric

The previous section was devoted to illustrate the real astrophysical phenomena we are interested in. Now we are going to introduce the mathematical formalism and some theoretical background useful to deal with extremely strong gravitational fields, those of BHs.

2.1 Rotating BH Metric

It has been demonstrated that only a restricted class of stationary configurations are possible for a BH, and this class is entirely described by the Kerr-Newman solutions of Einstein's field equations. It is a three-parameter family: apart from M, the angular momentum J and its total electric charge Q are sufficient to describe the system. Within this family, the only static and chargeless solution ($J = 0$, $Q = 0$) is the *Schwarzschild solution*

$$ds^2 = \left(1 - \frac{2m}{r}\right) dt^2 - \frac{dr^2}{1 - \frac{2m}{r}} - r^2 \left(d\theta^2 + \theta^2 d\phi^2\right) \tag{2.1}$$

where t is the time coordinate, while r, θ and ϕ have the usual meaning of spherical coordinates. The above line element is written in *geometrical units* so that the mass has the dimension of a lenght[1] (*gravitational radius*):

$$m = GM/c^2 \equiv r_g.$$

In fact, since all stars rotate, their remnants after a gravitational collapse – and therefore stellar mass BHs too – must possess an angular momentum. For supermassive BHs, accreting matter transfers its own angular momentum

[1] In AGN, the gravitational radius ranges in the orders of micro- and milli-parsecs.

to them. It is thus very likely that real BHs do have an angular momentum with respect to a symmetry axis.

If matter is accreting onto the BH, then it is supposed (if the BH and the accretion disc are co-rotating) to give some additional angular momentum until an equilibrium configuration is reached.[2] At the equilibrium, on the base of calculations made by Thorne (1974), the accretion rate would have an asymptotical value and the BH spin a fixed angular momentum $J_{lim} \simeq 0.9981\ m^2$.

However, it is important not to restrict assumptions on the central BH and thus consider the most general form for the metric of stationary, axially symmetric, asymptotically flat spacetimes, i.e. the *Kerr-Newman metric* (Chandrasekar 1983):

$$ds^2 = e^{2\nu}dt^2 - e^{2\chi}(d\phi - \omega dt)^2 - e^{2\mu_1}dr^2 - e^{2\mu_2}d\theta^2. \tag{2.2}$$

When using the normalized parameter $a = J/m$ to indicate the BH angular momentum, the above coefficients are:

$$\begin{aligned} \omega &= \frac{2amr}{A} \\ e^{2\nu} &= \rho^2\Delta A^{-1} \\ e^{2\chi} &= A\rho^{-2}\sin^2\theta \\ e^{2\mu_1} &= \frac{\rho^2}{\Delta} \\ e^{2\mu_2} &= \rho^2, \end{aligned} \tag{2.3}$$

with:

$$\begin{aligned} \rho^2 &= r^2 + a^2\cos^2\theta \\ \Delta &= r^2 - 2mr + a^2 + Q^2 \\ A &= (r^2+a^2)^2 - a^2\Delta\sin^2\theta = \\ &= \rho^2(r^2 + a^2 + 2ma^2r\sin^2\theta\rho^{-2}) \equiv \rho^2\Lambda. \end{aligned} \tag{2.4}$$

We shall refer to the coordinates used here, whose interpretation has been already given, as to *Boyer-Lindquist coordinates* [**B-L**], from the name of the authors who first – and independently from each other – discovered the

[2] In fact, with the now viable observational tools it has become clear that real accreting systems are hardly in equilibrium: their spectral variability shows, on the contrary, that the accretion rate $\dot{m}$ fluctuates. If the accretion disc does not co-rotate, or if the accretion flow resides in different, possibly changing directions and planes, then the BH angular momentum can even decrease.

coordinate transformation from the original form of the metric (K-S, see below) to the (2.2).

Since we will consider only chargeless BHs, the function Δ takes the form $\Delta = r^2 - 2mr + a^2$, thus determining a coordinate singularity in

$$r_+ = m + \sqrt{m^2 - a^2} \qquad (m \leq r_+ \leq 2m). \tag{2.5}$$

which tends to the well-known *Schwarzschild radius*

$$r_s = r_+(a \equiv 0) = 2m \tag{2.6}$$

in the limit of $a \longrightarrow 0$. For a given a, r_+ is a coordinate singularity in the sense that one can find physical trajectories falling inwards even below this limit, down to $r \longrightarrow 0$, by using different coordinate systems; but it does indeed correspond to an *event horizon*, i.e. a surface which cannot be crossed from inside towards outside. Such coordinate singularities are not to be confused with the physical singularities, which remain in all coordinate systems: for instance, in Kerr metric one coincides with the origin of the B-L frame and can be reached only along trajectories which are confined on the equatorial plane (Carter 1968):

$$r = 0; \quad \theta = \pi/2. \tag{2.7}$$

However, from an astrophysical point of view it does not make much sense to investigate the world inside the region $r < r_+$, which cannot be "seen" in any way... For further information on such mainly mathematical issues see e.g. Chandrasekhar (1983), Straumann (1988), Misner *et al.* (1973).

Both the Schwarzschild and the *Reissner-Noordström* (charged, static BH) metrics can be seen as limiting cases of the Kerr-Newman family of solutions (2.2). From (2.5) we get that a rotating BH must have a (normalized) angular momentum between 0 and m, and therefore $r_+(m) = m$.

In conclusion, the spacetime of a spinning chargeless BH is fully characterized by two parameters only, m ed a, and can be described by the metric (2.2) with $Q = 0$, i.e. the *Kerr metric*. Actually, in the original work Kerr used a different coordinate set (Kerr 1963, Kerr & Schild 1964) with three Cartesian-type spatial coordinates (x, y, z) and a time (T) (*Kerr-Schild coordinates*, **K-S**), in which one gets:

$$\begin{aligned} ds^2 &= dT^2 - dx^2 - dy^2 - dz^2 - \frac{2mr^3}{r^4 + a^2 z^2} \cdot \\ &\cdot \left[\frac{r(x\ dx + y\ dy) - a(x\ dy - y\ dx)}{r^2 + a^2} + \frac{z\ dz}{r} + dT \right]^2 \end{aligned} \tag{2.8}$$

being r one of the roots of the equation

$$r^4 - (x^2 + y^2 + z^2 - a^2)r^2 - a^2z^2 = 0. \tag{2.9}$$

To our aims, using K-S coordinates is not convenient, because each (x,y,z) set has to be associated with two different r's – those given by (2.9) – and thus to two distinct physical points. Moreover, in this coordinate system the axial symmetry is not evident any more, even if the flat-type, or, Minkowskian asymptotic component of the metric $dT^2 - dx^2 - dy^2 - dz^2$ can still be recognized immediately, because it corresponds to the $r \longrightarrow \infty$ or $m \longrightarrow 0$ limits.[3]

In many works yet another form is used to write the Kerr metric: this is the so-called *Kerr-Newman* form (**K-N**) which uses the coordinates u, r, θ and ψ:[4]

$$du = dt + \frac{r^2 + a^2}{\Delta}\, dr \tag{2.10}$$

$$d\psi = d\phi + \frac{a}{\Delta}\, dr \tag{2.11}$$

so that

$$\begin{aligned} ds^2 &= (1 - \frac{2mr}{\rho^2})\, du^2 - 2\, du\, dr + 2a\sin^2\theta \frac{2mr}{\rho^2}\, du\, d\psi + \\ &- \rho^2\, d\theta^2 - \frac{\sin^2\theta}{\rho^2} A\, d\psi^2 + 2a\sin^2\theta\, dr\, d\psi. \end{aligned} \tag{2.12}$$

The formulae to transform K-N into K-S coordinates are the following:

$$\begin{aligned} T &= u - r \\ x + iy &= (r - ia)e^{i\psi}\sin\theta \\ z &= r\cos\theta. \end{aligned} \tag{2.13}$$

Very recently, a new form of the Kerr solution has been proposed by Doran (1999). It uses the local proper time for free-falling observers as time coordinate; in this frame many physical phenomena are particularly clear and the solution is well behaved at the event horizon.

[3]The singularity structure can also be easily seen:

$$x^2 + y^2 = a^2,$$

i.e. the (2.7) when going back to B-L coordinates.

[4]The horizon function here disappeares from any denominator, so one cannot see the coordinate singularity $r = r_+$ any more.

2.2 Properties of a Kerr Spacetime

Ergosphere

Apart from the horizon, there is another relevant surface in Kerr metric, the one where g_{00} is zero: this surface is called *ergosphere*, and is described by the equation:

$$r_{stat} = m + \sqrt{m^2 - a^2 \cos^2 \theta}. \tag{2.14}$$

It has the form of a spheroidal, compressed along the spin axis direction, which becomes spherical and fully coincides with the event horizon only in the Schwarzschild limit. On the equatorial plane, $r_{stat}(\theta = \pi/2) = 2m$ independently of the spin.

Inside the ergosphere g_{00} is negative. No static observers can exist there, because their geodesics would be spacelike ($ds^2 < 0$); instead, all particles are forced to follow the "rotation of the metric". There can however be outgoing trajectories, therefore the ergosphere has not to be confused with a horizon.

Motion. Geodesics

Probably due to the quite recent discovery of the equations of motion, it is still impossible to find a unitary, detailed treatment of geodesics as well as non-geodetic physical orbits in Kerr metric. We found particularly useful the descriptions by Bardeen (1970), Bardeen *et al.* (1972), and Chandrasekhar (1983), whose works have been the base for the following summary.

The solution of the equations of motion in Kerr metric is due to Brandon Carter, who first recognized the separability of the related Hamilton-Jacobi equation (Carter 1968). In the B-L coordinate system, the problem can be solved in a similar way as he did in K-N to get:[5]

$$\rho^2 \dot{t} = -E(a^2 \sin^2 \theta - a\lambda) + E(r^2 + a^2)(r^2 + a^2 - a\lambda)\Delta^{-1} \tag{2.15}$$

$$\rho^2 \dot{r} = \pm E V_r^{1/2} \tag{2.16}$$

$$\rho^2 \dot{\theta} = \pm E V_\theta^{1/2} \tag{2.17}$$

$$\rho^2 \dot{\phi} = -E(a - \lambda sin^{-2}\theta) + aE(r^2 + a^2 - a\lambda)\Delta^{-1}. \tag{2.18}$$

where the auxiliary functions (2.4) have been used, and two more functions have been introduced:

[5]Referring to the K-S coordinate system, Carter (1968) wrote that it is "too awkward for a good physical use". However, Hameury *et al.* (1994) appear to have solved the equations of motion, and to have integrated them numerically for computing line profiles, using K-S coordinates.

$$\begin{aligned} V_r &= (r^2 + a^2 - a\lambda)^2 - \Delta[q^2 + (a-\lambda)^2 + r^2\gamma^{-2}] \\ V_\theta &= q^2 - \cos^2\theta[a^2(\gamma^{-2} - 1) + \lambda^2 \sin^{-2}\theta] \end{aligned} \tag{2.19}$$

We adopted here a convention in which the constants are normalized with respect to the energy E.[6] So

$$\lambda = L/E$$

is the particle angular momentum component along the rotation axis ($\theta = 0$);

$$q^2 = \frac{K}{E^2} - \lambda^2 - a^2$$

is the *Carter's constant*, which is directly linked to the *separation constant* K, sometimes called *fourth* constant of the motion. If μ is the rest mass of the particle,

$$\gamma^{-1} = \mu/E.$$

Looking at the V_θ analytical expression, one can recognize the divergence at the symmetry axis ($\theta = 0$). Indeed, real solutions for the motion through the axis are possible only if $\lambda = 0$ (Carter 1968) – and this will be used in section **??**. This can be simply understood in terms of angular momentum: if the particle trajectory meets the axis, then the total angular momentum $\vec{q} = \vec{r} \times m\vec{v}$ must be perpendicular to the axis itself.

Carter (1968) also showed that the condition

$$q^2 = 0$$

is necessary, but not sufficient, in order to have that a trajectory starting on the equatorial plane stays confined there forever. In fact, unstable orbits, with $q^2 = 0$, going out of the equatorial plane (thus not entirely lying on the plane, i.e. *tridimensional*) do exist (Chandrasekhar 1983), as well as tridimensional orbits which are completely outside the equatorial plane and have $q^2 = 0$, $\lambda \leq a$. The singularity (2.7) can be reached only by geodesics

[6] The Hamiltonian function H written by Carter is cyclic in (i.e. does not depend on) the coordinates u and ψ, therefore

$$p_u = -E, \quad p_\psi = L$$

are constants of the motion, respectively equal to the total energy of the particle, and to the axis-parallel component of its angular momentum.

with $q^2 = 0$. The only orbits which can cross the equatorial plane are those with $q^2 > 0$. If, on the contrary, $q^2 < 0$, then the trajectory does never intersect the equatorial plane. All this can be seen from:

$$q^2 = p_\theta^2 + \cos^2\theta[a^2(\mu^2 - p_t^2) + p_\phi^2/sin^2\theta],$$

which is directly derived from the Hamilton-Jacobi equation (cp. Bardeen *et al.*, 1972; Carter 1968).

K is always positive for the trajectories which cross the equatorial plane, and thus also for all photon trajectories (*null geodesics*) we are interested in – both those impinging onto (primary) and those escaping from the disc (see chapter 3).

For the photons we also have $\mu = 0$, thus $\gamma^{-1} = 0$ and

$$(V_r)_{ph} = (r^2 + a^2 - a\lambda)^2 - \Delta[q^2 + (a - \lambda)^2] \quad (2.20)$$

$$(V_\theta)_{ph} = q^2 - \cos^2\theta(\lambda^2 sin^{-2}\theta - a^2). \quad (2.21)$$

The equations of motion in r and λ can be reduced to a single integral equation:

$$\int_r V_r^{-1/2} dr = \pm \int_\theta V_\theta^{-1/2} d\theta. \quad (2.22)$$

Equation (2.22) is the one used for numerically integrating the photon trajectories, thus to compute spectra, as it will be seen later on. It is necessary to notice that these integrals are *elliptic integrals* because V_r, V_θ are quadratic functions (in r and in $\cos\theta$, respectively).

$V_\theta^{-1/2}$ is a periodic function, while $V_r^{-1/2}$ is monotonically decreasing after a certain value of r. It is also worth noticing that, for some values of r and θ, and for some values of the pairs (λ, q), the functions to be integrated are not defined because $V_{r,\theta}$ is less than or equal to zero. In such regions of the (r, θ) plane there is no solution for the equations of motion. Therefore the integrand functions are very important, because they allow a pretty simple, qualitative analysis of real trajectories.

The case of null geodesics (photons) deserves a few more words. Expression (2.21) can be rewritten as follows:

$$(V_\theta)_{ph} = q^2 + (a - \lambda)^2 - (a\sin\theta - \lambda\sin^{-1}\theta)^2$$

which is positive if and only if

$$q^2 + (a - \lambda)^2 > 0,$$

i.e. $q^2 > -(a-\lambda)^2$. In the limiting case one has trajectories with a constant θ and $\lambda = a\sin^2\theta$.[7]

In the case $-(a-\lambda)^2 < q^2 < 0$, one can never get neither $\cos\theta = 0$ nor $\cos\theta = 1$: the trajectory will neither intersect the symmetry axis, nor the equatorial plane. Thus for us, the most interesting cases are for $q^2 \geq 0$.

Let us now consider again the more general case of massive particles (*timelike* geodesics: e.g. Chandrasekhar, 1983; §64a). The orbits can be *bound* ($E < 1$), *critical* or marginally bound ($E = 1$), and *unbound* ($E > 1$). In the first two cases q^2 is non-negative, i.e. the trajectory will *cross the equatorial plane and oscillate* (see Fig. 2.1). The other orbits are somehow similar to the null geodesics: there are solutions with $q^2 > 0$ crossing the plane, solutions with $q^2 < 0$ which always stay away from the plane, and finally solutions with $q^2 = 0$.

Integral equations can be written also for t and ϕ (see Carter 1968, and Misner *et al.* 1973). One just has to be careful, as usual, with the $\pm$ signs, which derive from the roots of $V_{r,\theta}$ and can be arbitrarily choosen, but must be consistent in the various equations.

The expressions (2.15)-(2.18) also give the contravariant components p^μ of the energy-momentum four-vector, i.e. (for massive particles):

$$p^\mu = m_0 \frac{dx^\mu}{d\lambda} = m_0 u^\mu.$$

The covariant components are:

$$p_\mu \;=\; (\; E \;,\; \pm E V_r^{1/2} \Delta^{-1} \;,\; \pm E V_\theta^{1/2} \;,\; -\lambda E \;) \qquad (2.23)$$

In general, one has to keep in mind that in the case of rotating BHs the geodesics differ from those in the Schwarzschild's spacetime at least under one account: they are not confined in a plane generally. Circular geodesics are rare – in fact, they are possible only on the equatorial plane.[8]

[7] This particular kind of null geodesics, called *null congruences*, is useful to build up a basis to describe Kerr spacetime in a Newman-Penrose formalism. See Chandrasekhar 1983, page 350.

[8] For a treatment of frame dragging effects on discs *not* in the equatorial plane see: Bardeen & Patterson (1975). Being beyond the scope of this dissertation, we don't address the issue of non-geodesic motion in Kerr metric here.

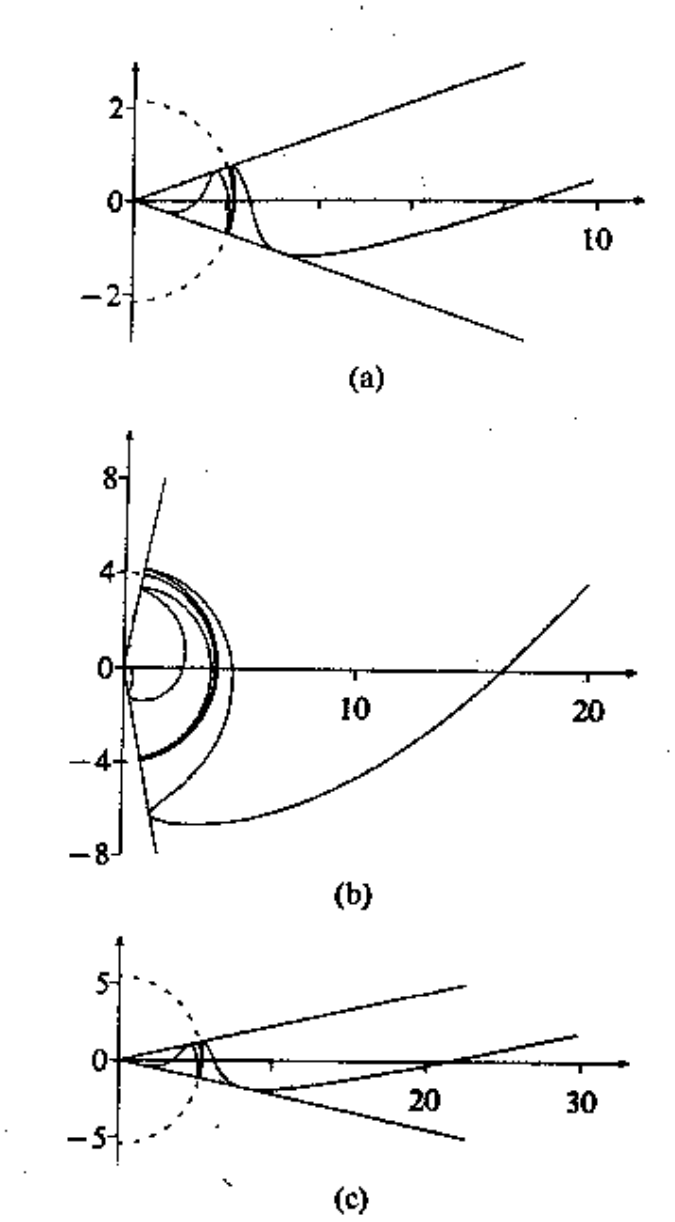

Figure 2.1: Examples of timelike geodesics' θ-oscillations when $E = 1$ (*critical* bound orbits) in the (r, θ) plane. The distance is expressed in units of m; the angular momentum a is $0.8m$. From: Chandrasekhar (1983).

2.3 Ray-tracing in Kerr Metric

The integrals in eq. (2.22) are *elliptic integrals*, i.e. belong to the class of integrals which can be reduced to the form (Goldstein 1950)

$$I = \int R[x, \omega(x)]dx$$

where R is a rational function, $\omega(x) = \sqrt{ax^4 + bx^3 + cx^2 + dx + e}$, a, b are not simultaneously equal to zero (otherwise the integral can be solved through circular funtions).

Every elliptic integral can be written in a standard Legendre's form – of the I, II or III kind – modulo a combination of circular functions; this is actually the case for the integrals in (2.22), too, as one can directly verify. To be more precise, the integrals in (2.22) are reducible to *Legendre's integrals of the first kind.*

Let us consider now equation (2.22) in more detail.

The θ integral can be easily rewritten in a standard form, with some differences in the cases of q^2 bigger, equal or less than zero (Chandrasekhar 1983, §63a,b). This is done using the root of the equation $V_\theta = 0$, i.e.:

$$\cos^2\theta = \frac{(\alpha^2 - q^2 - \lambda^2) \pm \sqrt{(\alpha^2 - q^2 - \lambda^2)^2 + 4q^2\alpha^2}}{2\alpha^2}, \qquad (2.24)$$

where:

$\alpha^2 = a^2(E^{-2} - 1)$ se $E^2 < 1$ (bound orbits);

$\alpha^2 = a^2(1 - E^{-2})$ se $E^2 > 1$ (unbound orbits);

$\alpha^2 = a^2$ se $E^2 = 1$ (photons and marginally bound orbits).

When referring to photon paths from an accretion disc to infinity, the first integral is between two finite values of θ ($\theta_{disc} = \pi/2$ and θ_∞). In this case, as well as for photons impinging onto the disc, we know that $q^2 > 0$, therefore $4q^2\alpha^2 > 0$ and thus we can take the + sign in (2.24).

The second integral extends up to $r_{obs} = \infty$, but can be rewritten as an integral between two finite extremes through a change of variable $r \longrightarrow 1/r$. The radial integral converges, as can be seen from the fact that V_r is monotonically increasing, so the function to be integrated goes to zero with increasing r.

Even in classical mechanics elliptic integrals are found in the solution of orbital motion's equations instead of an explicit form for the equation of the $\theta(r)$ trajectory, which is not always possible to write.

When a central potential such as $V(r)$ is involved, conservation laws lead to the equation:

$$\theta = \int \frac{Mr^{-2}dr}{\sqrt{2m[E - V(r)] - M^2 r^{-2}}} \; + \; constant$$

(Landau & Lifsits, 1975, Chap.3, §14), where M is the system's angular momentum with respect to the field center and m is the reduced mass $\frac{m_1 m_2}{m_1+m_2}$. In the classical case θ varies always monotonically with the time; the radial part can be treated as linear motion in a field with an effective potential energy

$$V_{eff} = V(r) + \frac{M^2}{2mr^2},$$

characterized by the centrifugal component $\frac{M^2}{2mr^2}$.

The locus of r's where the effective potential equals the total energy of the system E is the boundary of the region where motion takes place: on the boundary, the particle's radial speed is zero ($\dot{r} = 0$), while $\dot{\theta} = \frac{M}{mr^2} \neq 0$. Here are the motion's *turning points*, which can obviously be either minima or maxima (r_{min}, r_{max}).[9]

In the relativistic case, as well as in the classical one, we can derive the lower and upper limits – if they exist – through studying the denominator functions: in (2.22) this can be done both for r and θ. The variables' derivatives ("speeds") as well as the denominators become zero and invert their signs at the turning points.[10]

In order to compute an elliptic integral, one thus has to, first of all, find the variables values at the inversions, and then to consider separately the portions comprised between two subsequent turning points – and/or initial, or final points – changing the squared root's sign after each of them. The turning points of the θ trajectory are given by the roots of (2.24): there are two of them. On the other hand, V_r has four roots. Some of the roots can be degenerate, real or complex. By the turning points, the function (either V_r or V_θ) vanishes there with a real root.

[9] A trajectory can be limited in r, in which case both r_{min} and r_{max} do exist; this still does not mean that the orbit is closed. Closed orbits are an exception even in central potentials of classical mechanics: only for the gravitational Newtonian potential $V(r) \propto 1/r$ and the three-dimensional harmonic oscillator $V(r) \propto r^2$ it holds that all limited orbits are also closed.

[10] A powerful method to investigate the particle motion in Kerr spacetime is therefore given by the study of the regions where $V_{r,\theta}$ are greater than zero. The regions depend on the values of the constants of the motion, of course. A careful analysis of these regions and their boundaries (*inversion surfaces*) has been carried out by De Felice *et al.* (1974).

For the computation of line profiles and spectra, geodesics must be integrated from a Kerr BH accretion disc to the distant observer (*ray-tracing*). In this case, the initial and final θ values are obvious ($\theta_1 = \pi/2$ if we consider an equatorial discs, otherwise some function $\theta_1(r)$; and $\theta_2 = \theta_\infty = i$); in r, they are equal to the disc emitting point's radius and to a very large r (or infinity). Through a change of variable $r \longrightarrow u = 1/r$ the latter integral can be simplified and the second extreme ($r = \infty$) becomes zero.

From a numerical point of view, just notice that the first computations of geodesics in Kerr metric (e.g. Cunningham 1975) were performed using pre-computed elliptic integral values listed on textbooks (e.g. Byrd & Friedman, 1954). However, these tabulated values are not sufficient to achieve the precision needed nowadays: instead of using tables it is preferable, and tecnically possible now, to directly calculate the geodesics one by one. This is done with standard numerical techniques for computing integrals (Simpson's method) as explained e.g. in Martocchia (1996).

A minority of authors integrated the equations in a differential form instead of using the (2.22), applying well-known techniques like that by Runge-Kutta. However, from a practical point of view this method is as difficult as the integrals' one but pedagogically less interesting to explain – and widely known in any case!

Chapter 3

Computing Spectra

3.1 Kinematics of Relativistic Discs

For the reasons explained in section 1.3, we shall usually concentrate our investigation to optically thick, geometrically thin discs, assuming for simplicity that the emitting surface lies in the equatorial plane. Therefore we will normally use the physical model of SS accretion discs, as defined in section 1.3; the particle motion in such discs is *Keplerian*, i.e. planar, only determined by the central gravitational potential and by the conservation of angular momentum.

The accreting matter which surrounds a spinning BH at some distance can rotate both in the same or in the opposite sense with respect to the BH spin. But in fact, while falling inwards and approaching the event horizon, counter-rotating orbits are forbidden by the properties of the Kerr spacetime, which have been described in section 2.2. A supposedly counter-rotating flow must get reversed at some distance to enter the ergosphere along co-rotating orbits. An equatorial flow reaches the ergosphere at $r_{stat} = 2m$, independently of the value of a, as can be deduced from the formula (2.14).

Relativistic effects play a role in both determining the disc structure and affecting the electromagnetic radiation in the vicinity of the BH. The dynamics of relativistic SS discs has been first studied by Novikov & Thorne (1973) and Page & Thorne (1974), who gave the equations for the disc structure. The other physical aspects (energy and momentum transfer, viscosity, ...) have been so far simplified through a classical, or *pseudo-Newtonian*, treatment, even if the adoption of fully relativistic equations would be important to face the problems in a self consistent way.[1] Relativistic effects are important especially in the case of rotating BHs because in this case the disc can

[1] For a description of pseudo-Newtonian potentials refer to the Appendix.

extend much nearer to the event horizon, in terms of r. This has been first explained by Bardeen *et al.* (1972), whose work is the basic source for the formulae we are going to use in the following.

Let us consider circular, equatorial orbits in Kerr metric.[2] Their study is easier through the qualitative analysis of the behavior of the functions V_θ and V_r and their derivatives. It has been already stressed (section 2.2) that equatorial orbits have a zero Carter's constant. It has been also shown that such orbits, with constant r, are either bound or critical. The angular Keplerian velocity of a particle is given by:

$$\Omega_{eq} = \frac{d\phi}{dt} = \frac{u^\phi}{u^t} = \frac{\pm m^{1/2}}{r^{3/2} \pm a m^{1/2}} \tag{3.1}$$

where the signs depend on whether co-rotating ($\Omega > 0$) or retrograde orbits[3] are considered.

The *tangential velocity* is better expressed in the LNRF system (see Appendix), in which the particle is instantaneously located at the center of the reference frame - so that (Bardeen *et al.* 1972):

$$v^{(3)} = e^{\chi-\nu}(\Omega - \omega) \Longrightarrow \tag{3.2}$$

$$V_{eq} = v^{(3)}_{eq} = \pm \frac{\sqrt{m}(r^2 \mp 2a\sqrt{mr} + a^2)}{\sqrt{\Delta}(r^{3/2} \pm a m^{1/2})}. \tag{3.3}$$

V_{eq} can be understood as a "difference" between the particle velocity (Ω) and the "LNRF velocity" (ω) as seen by a distant observer. In the static limit we get

$$V_{eq} = \sqrt{\frac{m}{r - 2m}},$$

i.e.

$$\dot{\phi} \simeq \sqrt{\frac{m}{r^3}}.$$

Now let us normalize all quantities by $m = r_g$, so that m disappears from the formulae and everything, in the following, is expressed in "units of m".

Equatorial circular orbits are stable only down to the innermost radius r_{ms}, corresponding to (Figure 3.1):

[2] Table 4.5 provides a fast outlook of the simplified auxiliary functions on the equatorial plane.

[3] In the following we will always apply the upper sign to co-rotating, and the lower sign to retrograde orbits.

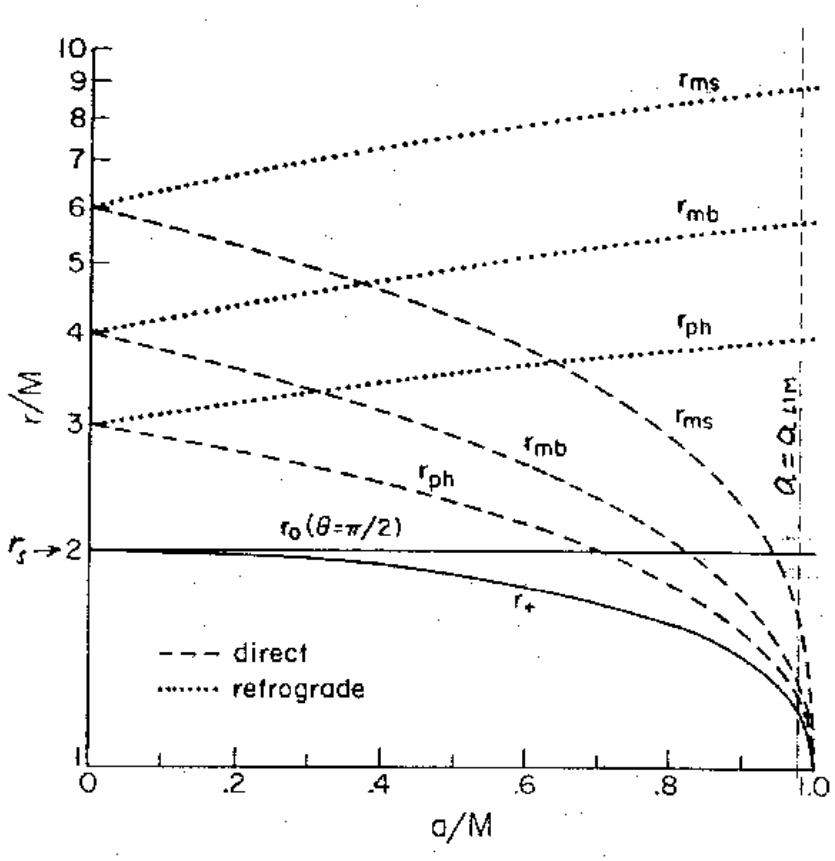

Figure 3.1: The most significant radii on the equatorial plane in Kerr metric, as functions of the BH spin. Here: r_o – corresponding to r_{stat} in the text – is the ergosphere boundary; r_+ is the event horizon; r_{ph} the minimum radius for particle circular orbits, corresponding to a photon orbit; r_{mb} the radius of the innermost bound orbit; r_{ms} the lower limit for circular stable orbits. Both cases of co-rotating (dashed) and counter-rotating (dotted) orbits are plotted. From: Bardeen *et al.* (1972).

$$r_{ms} = 3 + Z_2 \mp [(3 - Z_1)(3 + Z_1 + 2Z_2)]^{1/2} \tag{3.4}$$

with:

$$\begin{aligned} Z_1 &= 1 + (1 - a^2)^{1/3}[(1 + a)^{1/3} + (1 - a)^{1/3}] \\ Z_2 &= (3a^2 + Z_1^2)^{1/2} \end{aligned}$$

and therefore the well-known result arises (Thorne 1974):

$$r_{ms}(a_{lim} \simeq 0.9981) \simeq 1.232,$$

while in the Schwarzschild case $r_{ms}(a = 0) = 6$. This means that in Kerr metric stable orbits are allowed much closer to the BH than in the static case.

Treating V_r as a sort of effective potential, Bardeen and collaborators showed that there is a minimum radius for circular orbits

$$r_{ph} = 2 + 2\cos\left[\frac{2}{3}\arccos(\mp a)\right] \tag{3.5}$$

where the ratio between energy and rest mass of an orbiting particle becomes infinite (being thus the radius for zero rest mass particles, or the lowest possible radius for a circular orbit at all).[4]

In the static BH case, these radii have a simple graphic interpretation if one considers the diagram of the "effective potential", as in Chandrasekhar's textbook: there r_{ph} and r_{ms} are the abscissae for the maximum and minimum of the potential function. Of course, in the Schwarzschild metric this holds in all directions because an equatorial plane actually *does not exist* – or, better, there are infinite of them. The orbits with $r_{ph} \leq r < r_{ms}$ are unstable, while circular stable orbits have radii $r_c \geq r_{ms}$; in the case $a > 0$ such orbits can exist *only on the equatorial plane.*

Bardeen *et al.* (1972) pointed out the existence of a *marginally bound orbit*, corresponding to the radius

$$r_{mb} = r(E/\mu = 1) = 2 \mp a + 2\sqrt{1 \mp a}, \tag{3.6}$$

which is the minimum possible periastron for parabolic orbits;[5] here $\lambda = E/\mu = 1$.

The matter inflow from a geometrically thin disc *inside* the marginally stable orbit has been recently described in a pseudo-Newtonian approximation by Armitage *et al.* (2000).

[4]It may be useful to notice that r_{ph}(a=0) = 3, r_{ph}(a=1) = 1.

[5]From (3.3) we see that, independently of the BH spin, V_{eq} varies between 1 (i.e. the light's speed, reached at $r = r_{ph}$) and 0 – but not monotonically! Moreover, for $a = m$, its value at $r = r_{ms}$ is $V_{eq}(r_{ms}) = \frac{c}{2}$, while $V_{eq}(r_{mb}) = \frac{c}{\sqrt{2}}$.

Energy Shift

We will now use the reference frame of uniformly, circularly rotating matter on the equatorial plane (local disc frame LDF, $\mathbf{e}_{[\mu]}$, see Appendix): it is in this system that one can most easily deal with the photon emission from disc particles.

The four-velocity of the equatorial stable orbits in the "main" (B-L) system can be written as:

$$\mathbf{u}_e = \mathbf{e}_{[0]} = e^{-\nu}\gamma(\partial_t + \Omega\partial_\phi). \tag{3.7}$$

We are mainly interested in writing down expressions for the spectral shift of a photon: $g = E/E_0 = (1+Z)^{-1}$, which is, in the framework of GR:

$$g(\lambda, q) = \frac{(p_\mu)_{ph} u_o^\mu}{(p_\mu)_{ph} u_e^\mu}. \tag{3.8}$$

This formula contains both gravitational and kinetic effects (Narlikar 1994), thus neglecting only the cosmological. Let us now consider the four-velocities $\mathbf{u}_o$ (of the distant observer) and $\mathbf{u}_e$ (of the radiating disc particle) in the B-L system. They are the time "legs" of the respective comoving tetrads (see Appendix):

$$\begin{aligned} u_o^\mu &= (1,0,0,0) = e_0^\mu \\ u_e^\mu &= e^{-\nu}\gamma(1,0,0,\Omega) = e_{[0]}^\mu \qquad \text{from (3.7).} \end{aligned}$$

Using the expressions (3.1) and (2.23) one gets:

$$g_\infty(r_{eq}) = e^\nu \gamma_{eq}^{-1}(1 - \lambda\Omega_{eq})^{-1}, \tag{3.9}$$

so that for any circular, equatorial orbit (r_{eq}) and observer at infinity the spectral shift (3.9) does characterize a unique geodesic as well as the motion parameters do.

It may be useful to write down here some explicit, simple expressions for g_∞ of the photons emitted by a Keplerian disc, first in terms of $r = r_{eq}$ and $\Omega = \Omega_{eq}$ (Hameury *et al.*1994):

$$g_\infty(r = r_{eq}) = \frac{\sqrt{(1 - 2r^{-1} - r^2\Omega^2) + 4r^{-1}a\Omega - (1 + 2r^{-1})a^2\Omega^2}}{1 - \lambda\Omega} \tag{3.10}$$

and then, by substitution of Ω with the function $\Omega(r)$:

$$\begin{aligned} g_\infty(r = r_{eq}) &= (r^{1/2} - 1)\frac{\sqrt{r^2 + 2r^{3/2}}}{r^{3/2} + 1 - \lambda} = \\ &= \frac{(r^{1/2} + 1)\cos\Psi + r + r^{1/2} - 1}{\sqrt{r^2 + 2r^{3/2}}}, \end{aligned} \tag{3.11}$$

(Cunningham & Bardeen, 1973).[6]

3.2 Geometrical Optics

After the pioneering work by Cunningham & Bardeen (1973), analytical and numerical studies of geodesics in Kerr spacetime have been presented by De Felice *et al.* (1974, and references therein) and Pineault & Roeder (1977a,b). The latters used the null tetrad formalism of geometrical optics and derived results in the limit of weak field and low rotation. Afterwards, the optical appearance of a BH surrounded by an accretion disc has been carefully computed in 1979 by Luminet in Schwarzschild metric. In 1993 Viergutz discussed image generation in Kerr spacetime, while Rauch & Blandford (1994) presented a general-purpose code to trace geodesics in Kerr metric and calculated the caustic structure as a first application. In a quite different perspective, i.e. quasar microlensing, geodesics in Kerr metric have been integrated also by Agol & Krolik (1999).

A thorough review of the computations performed in order to get the predicted spectra from relativistic accretion flows will be presented in section 3.4. In the following we give some basic ingredients of geometrical optics which have been used in our computations.

For the integrations we need to write the element of solid angle $d\Omega_\infty$ as a function of the constants of motion. The problem here is to describe mathematically how the radiation flux is transmitted from one part of the system to the other, and to the distant observer, properly taking into account the distortion of the spacetime. So, for instance, with Ω_∞ we mean the (infinitesimal) *arrival* solid angle of the light ray which is emitted at some point near the BH. Because of the strong distortion, its expression in terms of the infinitesimal *emitted* solid angle

$$d\Omega_{[e]} = \sin\Theta d\Theta d\Phi$$

(here as a function of the emission angles in the LDF) is quite complex.

Let us define the *impact parameters* as the vertical and horizontal angular deviations with respect to the BH and its symmetry axis, and call them α and β, respectively.

To each null geodesic starting at a point P(r,ϕ) of the emitting matter corresponds an arrival point (α, β) on the image plane. Cunningham & Bardeen

[6] A more general expression for the photon energy shift between two arbitrary, circular orbits around the symmetry axis is given in the Appendix.

(1973) wrote the expressions for α and β as functions of the observer's inclination θ_∞ and the photon's constants of motion λ and q. If (a, b) are the image coordinates (Cartesian coordinates on the image plane), then: $\alpha \simeq \frac{a}{D}$ and $\beta \simeq \frac{b}{D}$. Because

$$\begin{aligned} a &= D\ \frac{p_{(3)}}{p_{(0)}} \\ b &= D\ \frac{p_{(2)}}{p_{(0)}}, \end{aligned} \tag{3.12}$$

where the vector components are those of the four-vector which is tangent to the geodesic in the LNRF system ($p^{(\alpha)} = \eta^{\alpha\beta} p_{(\beta)}$), one gets, in the limit $D \longrightarrow \infty$ i.e. $\theta_\infty \longrightarrow i$:

$$\begin{aligned} \alpha &\overset{D\to\infty}{\longrightarrow} \frac{\lambda}{\sin i} \\ \beta &\overset{D\to\infty}{\longrightarrow} V_\theta^{1/2}(\theta = i). \end{aligned} \tag{3.13}$$

Thus the arrival solid angle is linked to the variation of the impact parameters when the emitted solid angle – or: the constants of motion – varies:

$$d\Omega_\infty = \mid \frac{\partial(\alpha, \beta)}{\partial(\lambda, q)} \mid d\lambda dq.$$

The *Jacobian* $\mathbf{J} = \mid \frac{\partial(\alpha,\beta)}{\partial(\lambda,q)} \mid$ is easy to calculate through the formulae (3.13), being the determinant of the matrix:

$$\begin{pmatrix} \frac{d\alpha}{d\lambda} & \frac{d\alpha}{dq} \\ \frac{d\beta}{d\lambda} & \frac{d\beta}{dq} \end{pmatrix} = \begin{pmatrix} -\frac{1}{\sin i} & 0 \\ -\frac{\lambda}{\beta}\mathrm{cotan}^2 i & \frac{q}{\beta} \end{pmatrix},$$

thus finally:

$$d\Omega_\infty = \mid \frac{q}{\beta \sin i} \mid d\lambda dq = \frac{\mid q \mid d\lambda dq}{\sqrt{q^2 \sin^2 i + a^2 \sin^2 i \cos^2 i - \lambda^2 \cos^2 i}}. \tag{3.14}$$

We faced with the problem of computing the Jacobian in a rigorous way when using the directions of the emitted photons in their local frame (Θ, Φ) instead of the constants of the motion (Martocchia 1996).[7]

[7] Kojima (1991) gave the following expression:

$$d\Omega = 2\pi\ e^\chi \sin\Theta d\Theta d\Phi. \tag{3.15}$$

but this seems to us to have been derived in some unclear way, perhaps from the equalities

$$d\Omega_{B-L} \quad = \quad r^{-2}\sqrt{g_{\theta\theta} g_{\phi\phi}} d\theta d\phi \tag{3.16}$$

To do this we started from the (5.19) and (5.20), i.e. directly using the definitions, and easily derived the analytical form:

$$\begin{aligned} \mathbf{J}' &= \mid \frac{\partial(\lambda,q)}{\partial(\Theta,\Phi)} \mid = r\gamma_{eq}e^{-\nu} \cdot \\ &\cdot \quad [e^{\nu-\chi}+(\omega-\Omega_{eq})V_{eq}]^2 \frac{\sin^2\Theta \mid \cos\Phi \mid}{\mid e^{\nu-\chi}+\Omega_{eq}\sin\Theta\sin\Phi+\omega V_{eq} \mid^3}. \end{aligned} \quad (3.18)$$

This is in fact the Kerr equivalent of the expression written by Fabian *et al.* (1989) for the static (Schwarzschild) case.

We can also obtain the expression which links the emission solid angle $\Omega_{[e]}$ to the solid angle at infinity, or, "as seen by the fixed stars" Ω_∞:

$$\begin{aligned} d\Omega_\infty &= \mid \frac{\partial(\alpha,\beta)}{\partial(\lambda,q)} \mid \cdot \mid \frac{\partial(\lambda,q)}{\partial(\Theta,\Phi)} \mid d\Theta d\Phi = \mid \frac{q}{\beta\sin i} \mid \ \mathbf{J}'\, d\Theta d\Phi = \\ &= \mid \frac{qr\gamma_{eq}}{e^\nu \beta \sin i} \mid \cdot [e^{\nu-\chi}+(\omega-\Omega_{eq})V_{eq}]^2 \cdot \\ &\cdot \quad \frac{\mid \sin\Theta\cos\Phi \mid}{\mid e^{\nu-\chi}+\Omega_{eq}\sin\Theta\sin\Phi+\omega V_{eq} \mid^3} d\Omega_{[e]}. \end{aligned} \quad (3.19)$$

3.3 Local Emissivity

In order to study relativistic effects on reflection spectra and lines from accreting BH systems it is first of all necessary to carefully reproduce the locally reflected spectrum in terms of radial, angular (including *limb darkening*, see next), and frequency dependences, fully taking into account the chemical and ionization conditions of the matter. All this depends on the illuminating radiation field, i.e. on the characteristics of the primary radiation, which is also affected by relativistic distortions.

$$\begin{aligned} &= r^{-2}\rho e^{\chi} d\theta d\phi \\ &= r^{-2}\sin\theta\sqrt{A}\, d\theta d\phi \\ &\equiv r^{-2}\sqrt{r^2(r^2+a^2+2mr^{-1}a^2)}\cdot \sin\Theta d\Theta d\Phi, \end{aligned} \quad (3.17)$$

where Ω_{B-L} would be the emission angle in the B-L reference frame. The (3.16) is the relativistic analogue to the usual Euclidean expression for the solid angle. However, the last passage consists in roughly substituting at any function its value at the emission point, i.e. on the equatorial plane, which is not properly correct because the original expression holds for a source located *at the B-L coordinates origin*, i.e. just the BH itself!

Radial Dependence

Usually, for the computations of spectra in BH metric the disc emissivity has been taken as $F(r) \propto r^{-q}$. An emissivity law of this kind follows also from the Page & Thorne (1974) model (also: Novikov & Thorne, 1973). But the actual emissivity is much more complex and depends on the geometry of the illuminating matter.

Various attempts to derive the emissivity law $F(r)$ by "inverting" the observed line profiles have been made, e.g. by Čadež *et al.* (1999), Dabrowski *et al.* (1997), and Mannucci *et al.* (1992). Fitting with a simple power law, from the observations of Seyferts the corresponding index results in general to be near to $q = 2.5$ (Nandra *et al.* 1997a). This rather steep dependence implies that the illumination is strongly concentrated in the inner regions, with a half of the line emission coming from the radii lower than $\sim 20m$, which is consistent with the model of a "central" illuminating source. This model is sometimes called *anisotropic illumination model* (Henry & Petrucci 1997), which in the basic version corresponds to a pointlike, "lamp-post" illuminating source.

Dependence on Inclination

The overall X and γ-ray reflection spectrum is found to be strongly angle-dependent. When the accretion disc is seen with a nearly edge-on orientation the reflection hump is weak, while a face-on viewing angle provides a prominent hump.[8]

As the inclination at which the disc is viewed increases, the observed flux diminishes as an effect of the projection of the area, which corresponds to a cosine factor introduced in the emissivity law.

However, because the emitted photons are absorbed and scattered while leaving the disc surface at an oblique angle, the overall effect may be an obscuration (*limb darkening*) or, conversely, a brightening. Analytical formulae for this not-straightforward dependence on the angle have been given by Ghisellini *et al.* (1994):

$$\frac{I_{fluor}(\mu)}{I_{fluor}(\mu = 1)} = \frac{\mu \; ln(1 + 1/\mu)}{ln2} \tag{3.20}$$

[8]This effect is particularly strong in the model by Malzac *et al.* (1998). However, reflection-dominated Sy-1's are not observed, and these authors derive only high inclinations for some selected objects. Apparently the model succeeds in reproducing individual observed spectra, but contradicts the assumption that Sy-1's are seen at low inclinations. On the other hand, ionization could yield the solution of the puzzle, relaxing the constraints on the high energy cutoff in Seyferts, too.

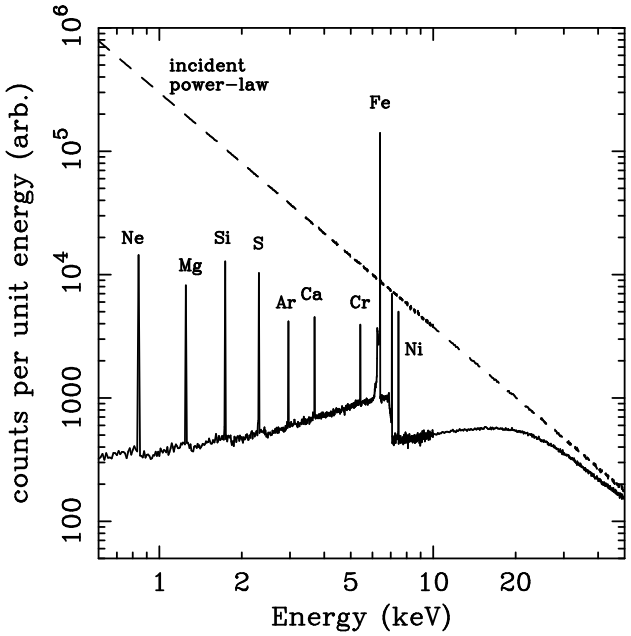

Figure 3.2: Here are the main reflection features generated by an illuminated cold disc, computed on the base of the Montecarlo method. From Reynolds (1996).

holds for the fluorescent emission, while the angle dependence for Compton-reflected photons is:

$$\frac{I_{refl}(\mu)}{I_{refl}(\mu=1)} = \mu[(3-2\mu^2+3\mu^4)ln(1+1/\mu)+(3\mu^2-1)(1/2-\mu)]. \quad (3.21)$$

Clearly, the disc reflection and fluorescence cannot be isotropic as the thermal emission, and the intensity varies with the incident angle of the primary photons, too.

Local Spectra

Of course, the reflected spectra do depend on the ionization state of the matter, and this in turn can be determined by the X-ray irradiation. A useful quantity in this discussion is the *ionization parameter*

$$\xi(r) = 4\pi F_X(r)/n(r) \quad (3.22)$$

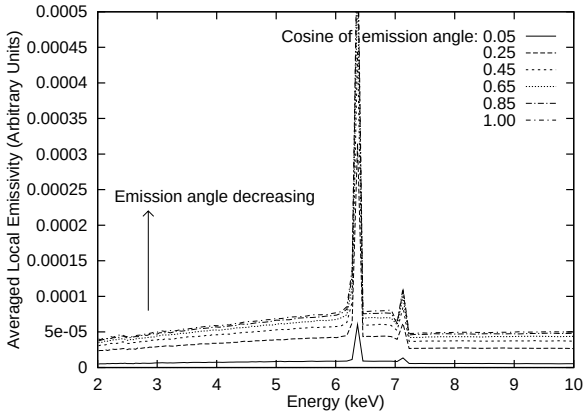

Figure 3.3: Examples of local spectra $F(E)$ around the iron line rest energy, $E_0 = 6.4$ keV. *Only angular dependences of the outgoing flux are shown here:* F represents the radiation flux averaged over the incident angle of the photons from the primary source.

where $F_X(r)$ is the X-ray flux received per unit area of the disc at radius r, and $n(r)$ is the comoving electron number density. The ionization parameter measures the ratio of the photoionization rate to the recombination rate. The iron line emission for various ionization parameters has been investigated by Matt *et al.* (1993, 1996) assuming a fixed density structure in the disc. Self-consistent computations have been performed by Ross *et al.* (1999) who showed the spectra as they appear both locally and to a distant observer, after relativistic smearing in Kerr metric, and used them to fit the *ASCA* and *Ginga* data of Cyg X-1 (Young *et al.* 1999).

Nayakshin *et al.* (1999) have relaxed the assumption of a fixed density, including also the effect due to thermal instability in the irradiated disc atmosphere.

Advanced computations of broad-band local spectra and emissivity laws, which are used in our most recent and ongoing work, are widely described in section 3.6.

3.4 A Review of Previous Works

We now summarize relativistic calculations of spectra performed in the past years. Certain details on the techniques which have been used will be given here along with the main results; however, see also sections 2.3 and 3.2 for issues concerning the integration of photon paths and computations of spectra in curved spacetimes.

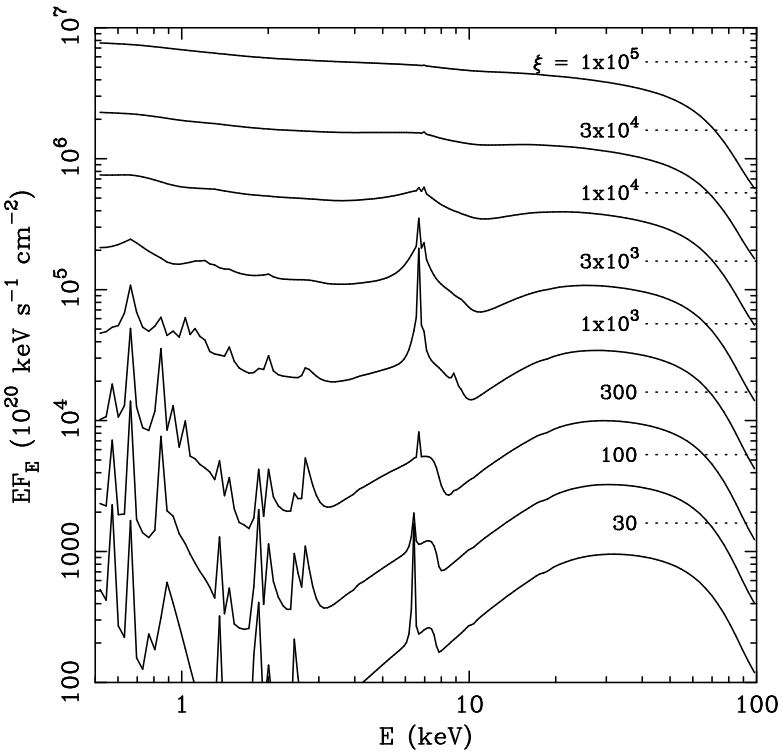

Figure 3.4: Reflection spectra from ionized matter for various values of the ionization parameter ξ. The dotted lines show the level of the illuminating power-law continuum. From Fabian *et al.* 2000.

First Studies

Some important relativistic effects on the radiation coming from accreting, spinning BH systems were discussed already in the pioneering works by Cunningham (1975, 1976), which dealt with the *thermal continuum* emission from the disc. In the current astrophysical models this emission can be relevant, in the X-band, only in the case of low mass BHs, as explained in section 1.4, nevertheless the technique originally developed by Cunningham has been a pillar for all subsequent computations of spectra in Kerr metric.

Cunningham introduced a *transfer function*[9] which accounts for the gravitational lensing of the light rays; Doppler enhancement of the radiation from the part of the disc approaching the observer was estimated; and the effect of the disc self-irradiation was discussed.

Later on, relativistic distortions of *line profiles* have been computed in Schwarzschild metric, initially by Fabian *et al.*(1989) and Stella (1990). The latter also modelled variability due to variations of the central source.

These first calculations of relativistic line profiles already pointed out the fundamental properties: first of all, the blue extent of the line is almost exclusively a function of the observer inclination, thereby providing a robust way to measure the inclination of the disc.[10]

On the other hand, the redward extent of the line is sensitive to the inner radius of the line-emitting portion of the disc, and thus to the BH spin, but depends strongly on the disc emissivity law, too. This because the red tail, being produced by the photons from the innermost orbits, is due both to the gravitational redshift and to the transverse Doppler redshift.

As an effect of the rotation of the matter, it follows that even in a classical (Newtonian) scheme the profiles from inclined discs must be *double-peaked* as a consequence of the kinematic (Doppler) energy shift. The effect grows with growing θ_∞, while at low inclination the double peak disappears and only the gravitational redshift plays a role. Apart from this Doppler feature,

[9]The *transfer function* gives the specific flux (per unit energy) due to each emitting disc ring, including the relativistic distortion of the solid angle from the emitter to the observer.

[10]Interestingly, a careful comparison with the spectral data of more than 20 Sy-1's (Nandra *et al.* 1997a, Reynolds 1997) shows that the inferred inclinations of the accretion discs are clustered around 30 degrees, which is in accordance with the AGN unification scheme (e.g. Antonucci 1993). However, see section 1.4 for more discussion on this issue.

the main (special) relativistic effect on the line profiles is that the peak at higher energy ("blue") is higher. This because of the *Doppler boosting*, which intensifies the radiation from the approaching matter with respect to the receding one.

Bao (1992, 1993), Bao & Stuchlik (1992) and Matt *et al.* (1992, 1993) also noted that a feature between the two horns arises because of the lensing effect at high inclination (disc seen edge-on). This is due to the amplification of the flux coming from the opposite side with respect to the BH. In Figure 3.5, where evidence is given to the contributions to the line flux due to the various disc sections, the origin of these additional features is clearly showed.

For an outlook of the geodesic computation formalism in Schwarzschild metric see e.g. Luminet (1979), Fabian *et al.* (1989), Matt (1992).

Computations in Kerr Metric

More recently, a wealth of work has been made in Kerr metric thanks to many authors, starting with Laor (1991), Kojima (1991), Hameury *et al.* (1994).[11] These works follow similar paths to the solution, whose basic ingredients will be described in the following for completeness and reader's convenience.

First of all, let us define some quantities which are relevant for the numerical approach.

The *specific flux* (per unit energy) as detected by a distant observer is:

$$F_\infty(E_\infty) = 2\pi \int_{r_1}^{r_2} \int_\Omega \frac{dF_\infty}{dr d\Omega_\infty}(E_\infty, r, \Theta) \cos\Theta \, d\Omega_\infty \, dr. \tag{3.23}$$

Θ is the angle between the direction of a photon re-emitted by a disc matter particle and the normal to the disc surface; (Figure 5.1); thus the factor $\cos\Theta$ accounts for the *projection* of the emitting surface. $\frac{dF_\infty}{dr d\Omega_\infty}$ is the *specific flux per unit of solid angle* i.e. the specific intensity, or *brightness*, coming from the infinitesimal ring of radial extension dr and area $dS = 2\pi r \cdot dr$ towards the observer. We have:

$$\frac{dF_\infty}{dr d\Omega_\infty} \equiv I_\infty(E_\infty, r, \Theta) = g^3 I_e(E_\infty, r, \Theta),$$

thus

$$F_\infty(E_\infty) = 2\pi \int_{r_1}^{r_2} \int_\Omega g^3 I_e(E_\infty, r, \Theta) \cos\Theta \, d\Omega_\infty \, dr. \tag{3.24}$$

[11] Hameury *et al.* used K-S coordinates instead of the commonly adopted B-L.

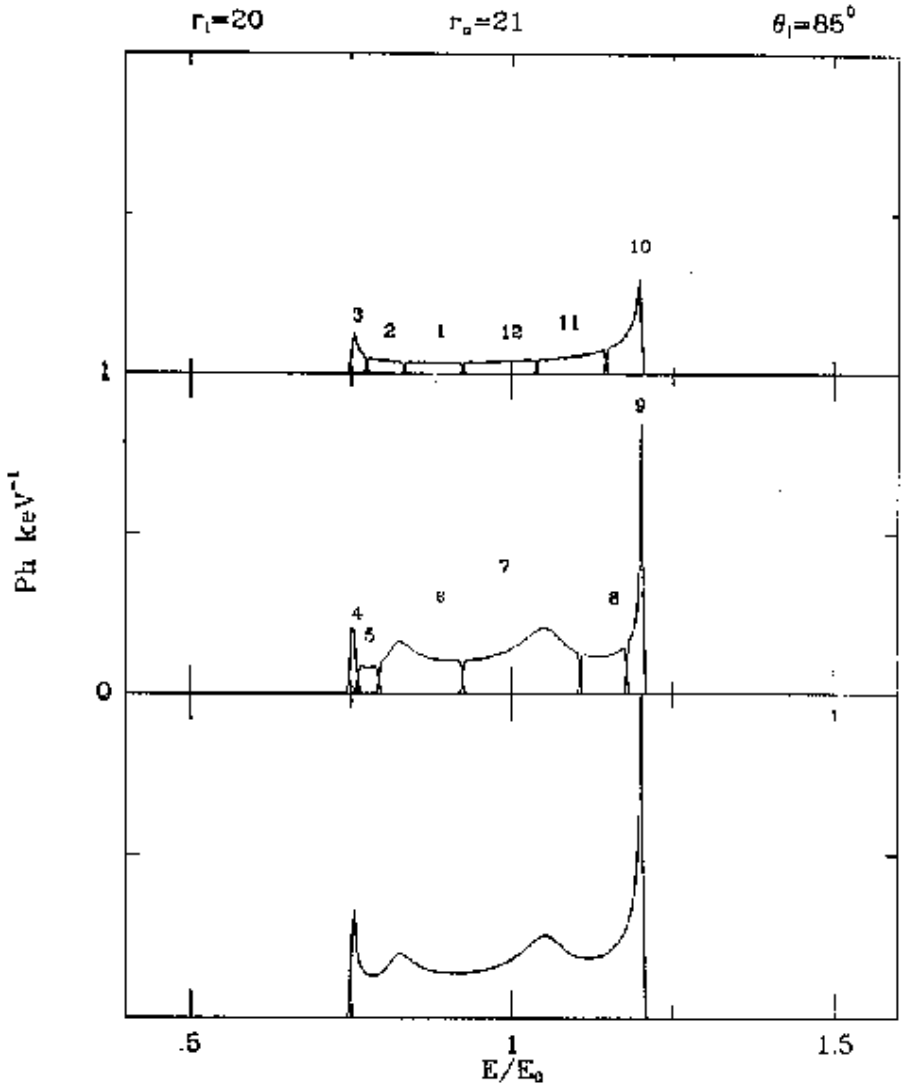

Figure 3.5: The line profile can be divided to stress the contributions due to the various angular portions of the disc. This computation has been made for a narrow ring of radius $r_e \simeq 100m$ in Schwarzschild metric. Taken from Matt (1992).

The shift has an exponent 3 because of the *brightness law* which states that the ratio I/E^3 stays constant along the photon trajectories.[12]

Limiting ourselves to a *monochromatic emission*, we could eliminate the dependence on E_∞ by using a property of the Dirac's delta function $\delta(x-x_0)$ for $E_e = E_0$ and $E_\infty = gE_0$:

$$I_e(E_\infty, r, \Theta) \equiv \tilde{J}_e(r, \Theta)\delta(E_\infty - gE_0) =$$

$$= \tilde{J}_e \cdot g\delta(E_e - E_0) = I_e(g = \frac{E_\infty}{E_0}, r, \Theta),$$

thus the integration in this case will actually be on terms g^4:

$$F_\infty(g) = 2\pi \int_{r_1}^{r_2} \int_\Omega g^4 \tilde{J}_e(r, \Theta) \cos\Theta \; d\Omega_\infty \; dr. \tag{3.25}$$

The model of the disc is thus in general characterized by a radiation intensity $\tilde{J}_e$ emitted locally from its surface (or in general at a height $z \equiv z(r)$, because the disc profile is not necessarily flat) at frequency ν_e. $\tilde{J}_e$ is therefore the *superficial emissivity* or, equivalently, the brightness of an infinitesimal ring corresponding to $r = r_e$. This is the intensity emitted by the ring within an infinitesimal solid angle around the direction (Θ, Φ), and can be rewritten to isolate the r dependence:

$$\tilde{J}_e(\nu_e; r, \Theta) = F(r)\varphi(\nu_e)Y_e(\Theta), \tag{3.26}$$

where Θ denotes the angle between the ray and the direction normal to the disk in LDF (cp. Appendix).

Now it is necessary to express (3.25) in terms of quantities we are able to (numerically) integrate. Thus, $d\Omega_\infty$ should be rewritten in terms of the emission angles, or directly in terms of the constants of motion λ and q. For a fixed disc "ring" the integral (3.25) can be re-written using (3.14):

$$\begin{aligned} \frac{dF_o}{dr}(r) &= 2\pi \int_\Omega g^4 \tilde{J}_e(r, \Theta) \cos\Theta \; d\Omega_o = \\ &= 2\pi \int g^4_{\lambda,q} \tilde{J}_e(r, \Theta) \cos\Theta_{\lambda,q} \mid \frac{q}{\beta \sin i} \mid d\lambda dq. \end{aligned} \tag{3.27}$$

What is integrated here is the infinitesimal flux contribution by the geodesics with constants $(\lambda, q) \div (\lambda + d\lambda, q + dq)$. Introducing the *transfer function*

[12] Namely, I/ν^3 is a Lorentz-invariant quantity: cp. Misner *et al.*, 1973, §22.6. The previously mentioned Doppler-boosting effect is due to this law.

$T(r;\lambda,q)$ – which includes the Θ dependence of the disc emissivity $Y_e(\Theta)$ – we get

$$\frac{dF_o}{dr}(r) \propto J_e(r)\int_{\lambda,q} T(r;\lambda,q)d\lambda dq \tag{3.28}$$

$$T(r;\lambda,q) = g^4_{\lambda,q}\cos\Theta_{\lambda,q}Y_e(\Theta)\mid\frac{q}{\beta_{\lambda,q}\sin i}\mid. \tag{3.29}$$

For the sake of numerical computation, this must be trasformed in a summation over discrete values of the constants:

$$\Delta F_o(r) = J_e(r)\sum_{\lambda_k,q_k} T(r;\lambda_k,q_k), \tag{3.30}$$

or, better, to a summation over discrete values of geometrical variables such as the emission angles of the photons (e.g. Kojima) or the inclination Θ with respect to the vertical and the spectral shift g (e.g. Cunningham, Laor).[13]

Let us consider what Cunningham & Laor did: take some point on the $r = r_e$ ring. Photons will leave towards all directions (Θ,Φ) from there. Thus to compute a spectrum one would consider all possible – or at least a significant sample – of (Θ,Φ) couples in the 2π solid angle; then iterate over all possible points on the ring ($0<\phi<\frac{\pi}{2}$), and finally consider all values of r_e between the fixed r_1 and r_2... This is not a convenient method, of course! But fortunately, for every fixed ring $r\equiv r_e$ and observer at $\theta_\infty\equiv i$, to each value of g do correspond only *two* geodesics, emitted in different directions, with $T_1 = T(r_e;\lambda_1,q_1)$ and $T_2 = T(r_e;\lambda_2,q_2)$. Therefore we can use – as Cunningham and Laor actually did – the correspondence between g and the direction of emission, and between the latter and the point on the ring, to drastically reduce the space of parameters to be considered: just scan all Θ

[13]It is easy to find analytically that for the transfer function $T(r;\lambda,q)$ we have ($\sin\Theta>0$ because $0<\Theta<\frac{\pi}{2}$):

$$T(r;\lambda,q)d\lambda dq = g^4\cos\Theta Y_e(\Theta)\mid\frac{q}{\beta\sin i}\mid[\frac{\partial(\lambda,q)}{\partial(g,\Theta)}]dgd\Theta =$$

$$= g\mid\frac{re^\nu}{\gamma_e\Omega_{[e]}}\frac{q}{\beta\sin i}\mid\cos\Theta\sin\Theta Y_e(\Theta)d\Theta dg = T(r;g,\Theta)dgd\Theta. \tag{3.31}$$

The Jacobian $[\frac{\partial(\lambda,q)}{\partial(g,\Theta)}]$ here has been directly derived on the base of the parameters of the motion, while Cunningham and Laor preferred to use

$$d\lambda dq = \frac{\partial(\lambda,q)}{\partial(g,r_e)}dgdr_e = [\frac{\partial(g,r_e)}{\partial(\lambda,q)}]^{-1}dgdr_e,$$

where the dependence $g=g(\lambda,q)$ from (3.9) is used, and $r_e = r(\lambda,q)$ is expressed in implicit form through inverse Jacobi elliptical functions [Cunningham 1975, equation (A21)].

between 0 and 90, and for each of them sample the g's comprised between reasonable values of the energy shift (e.g. 0.3 and 1.7). So Φ and ϕ have no role to play.

For each geodesic picked up in this way, the constants of the motion are given by inversion of (5.15) and (3.9). The integrals of the motion in r and θ can now be computed (see section 2.3): if they are equal to each other, then the geodesic gives a contribution to the "observed" spectrum. At this point, after "weighting" each of them by the emissivity, the contributions due to each ring are summed together.

In their works, Cunningham[14] (1975, 1976) and Laor (1991) also took into account the *returning radiation*. These are photons falling back onto the disc because of the strong spacetime curvature in the innermost part of the system. A very rough estimate is that up to 2/3 of the photons emitted below $r \sim 2$ can be lost in this way, but the effect becomes rapidly less important with increasing r. Above $r \sim 2$, this effect should reduce the line emission by no more than 10 or 20 percent, moreover partly compensated by the extra illumination given by the returning photons themselves.

Actually, the reillumination can be even neglected in the case of Kα line emission, because the energy of such photons is usually smaller than the K-edge energy (7.1 keV, compared to the 6.4 keV of the line rest energy) so that no photoionization can be produced by them.[15]

Starting from the Image Plane

Instead of explicitly calculating the transfer function, one can equivalently divide the disk image in individual pixels and evaluate contributions to the total radiation flux directly at infinity. This method allows to compute spectra much faster, because it avoids to consider unnecessary trajectories, and has therefore been employed by most of the authors in recent years, for instance by Karas *et al.* (1992) and Bromley *et al.* (1996). These authors also considered the light curves produced by a line-emitting hot spot co-rotating with the disc.

[14] In Martocchia (1996) we noticed that equation (A3d) in Cunningham (1975) holds in a K-N reference system, NOT in the B-L as it is used in that work. Let us remark that the mathematical background used by Cunningham has not been fully described by this author in his original paper; rather, for its careful explanation see: Speith *et al.* (1995).

[15] A very small effect can be produced by those returning photons which satisfy:

$$g_{ret} > \frac{7.1}{6.4} \simeq 1.1$$

Similar conclusions on the returning radiation issue were derived by Dabrowsky *et al.* (1997).

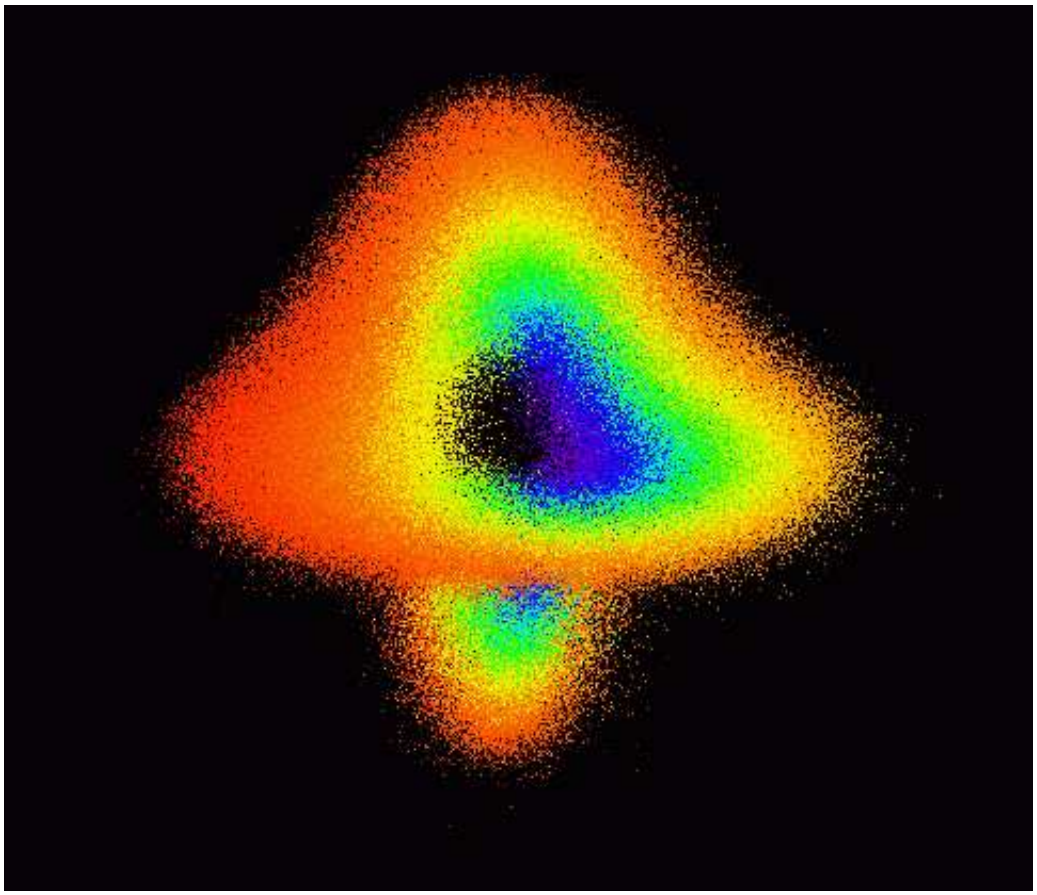

Figure 3.6: False-colour, synthetic image of an accreting black hole. This figure illustrates the direct and the first indirect image of a disc rotating around a fast spinning Kerr black hole and viewed almost edge-on. Relativistic effects on the light propagation are evident: namely, the lensing of the light originating from the part of the disc that is in upper conjunction with the hole, and the energy shift given by the interplay of gravitational and Doppler effects. The existence of higher images is ignored in most works – and also in our fits of the specific sources hereafter – because they do not contribute much to the total signal except for some unusual configurations (extreme edge-on inclination with little obscuration by material in the equatorial plane). This image is a by-product of the code used for spectra computations from a stationary disc (Martocchia, Karas & Matt 2000; image elaborated by V. Karas).

In this method, each point on the detector plane is connected with the corresponding point of emission on the disk surface by a light ray, i.e. a null geodesic in the spacetime. So the light rays can be integrated only when needed, i.e. when belonging to the image, through collecting their contributions on the observer's sky plane.

Another advantage of this approach is that it allows to draw an image of the accretion flow, just by associating the resulting value of the flux to each point on the image plane.

Karas *et al.* (1992) integrated extensive sets of geodesics, approximated their shapes by appropriate functions (Chebyshev polynomials) and stored the parameters of the approximating functions in an electronic archive ("catalogue") for later use. This method is useful when information from such a catalogue is used many times because on this way unnecessary recalculation of light rays is avoided. A disadvantage is in the necessity of additional routines which interpolate between data from the catalogue in order to determine the shape of a geodesic with prescribed, required parameters, and the fact that efficient storage of files is machine-dependent.

This catalogue technique is the base of our recent work, as described in section 3.7. Let us therefore give some more technical details of it. Each catalogue is characterized by the parameters a and i, and each geodesic in a catalogue is characterized by the (ρ, ψ) coordinates of its intersection with the image plane (starting point of the integration). The curves have been integrated by Karas *et al.* (1992) using the differential equations and the Runge-Kutta numerical method; after crossing the equatorial plane, the trajectory is followed in the opposite direction to check the accuracy of the integration routine. The curve is then fitted with a Chebyshev polynomial, which, roughly speaking, has the advantage to minimize the maximum error of the approximation by using the lowest possible order of the polynomial (50 is the fixed maximum). Far from the hole, where trajectories are fairly straight, the polynomial can have of course a lower order than near the BH.

The coefficients are then stored in direct access files. The information is valuable to restore not only the shape of the curve, but also the light travel time and the effect of time delay.

The profile and EW of the iron line from a disc around a Kerr BH have been computed again, with a broader coverage of the involved parameters, by Dabrowsky *et al.* (1997), who had a special interest in the comparison with the famous *ASCA* data of MCG–6-30-15 (see section 4.3).

Fanton et al. (1997) performed similar computations. For a careful de-

scription of the formalism used there and in similar works see: Čadež *et al.* (1998).

Also Speith *et al.* (1995) described thoroughly the formalism and method used to compute the photon transfer function in Kerr metric.

More Remarks

While most of the works on this issue have considered geometrically thin, purely Keplerian discs, some authors have extended the analysis to include those effects on line profiles due to finite disc thickness, self-gravitation, non-Keplerian velocity fields in the accretion flow, or even turbulence, at the expense of adding one or more ambiguous variables in the whole picture.

Karas *et al.* (1995) considered self-gravitating discs and found that the effect on the line photons is to further scatter their energy distribution i.e. to enlarge the profiles.

Pariev & Bromley (1997, 1998) studied the effects of non-negligible thickness and turbulence in the accretion flow, which also produce line broadening. Rybicky & Bromley (1997) investigated the presence of velocity gradients induced by the differential flow, which cause anisotropic local emission, finding that they would produce a relative increase of flux in the red line wing.

The latter paper also includes some considerations on the possibility that efficient line emission from matter inside the last stable orbit be possible. This line of research has been suggested in Bromley *et al.* (1998), while specific calculations had been performed for this case for the first time by Reynolds & Begelman (1997) in Schwarzschild metric, paying attention to the optical thickness and ionization state of such matter. They pointed out that if a contribution to the line is allowed from matter in free-fall inside the marginally stable orbit, then the BH angular momentum parameter is not so relevant in determining the spectral features, therefore not easy to constrain observationally. If this is the case, the presence of an extended red tail of the line could no longer be used as an evidence for rapid rotation of the black hole, whereas the validity of the "spin paradigm" (the assumption that rotating black holes are associated with jet production and radio-loudness; see section 1.4.2) could be preserved.

Young *et al.* (1998) further analyzed this issue fully taking into account the effects of ionization of the innermost part of the accretion flow on the Compton reflected continuum, concluding that the reflection component in MCG–6-30-15 is not consistent with the expected ionization state of the matter inside $r_{\rm ms}$. Below $6m$, the density of the infalling material drops rapidly and it becomes photoionized by the X-ray primary flux, producing a large

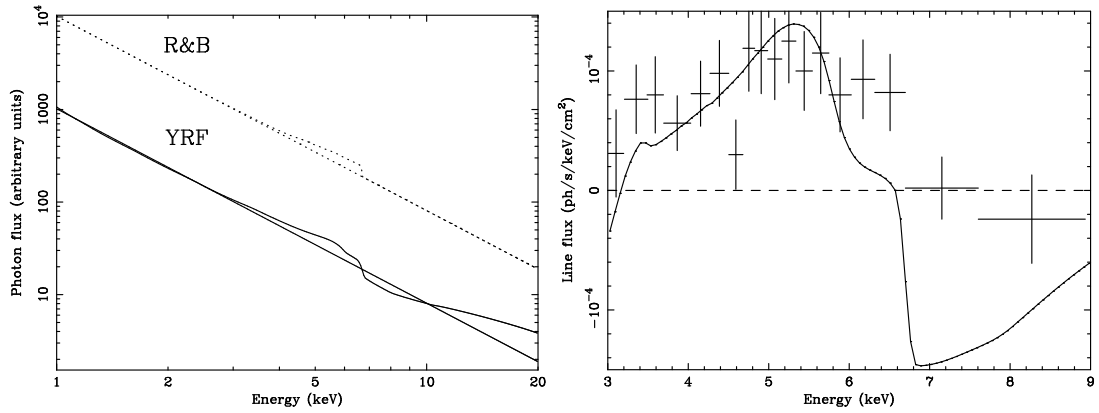

Figure 3.7: The left panel shows a comparison of Reynolds & Begelman's model (1997) with one in which the Compton reflected continuum is fully taken into account (Young *et al.* 1998). The latter spectrum shows a strong absorption edge that appears to be inconsistent with the data of MCG–6-30-15 (right panel). From Fabian *et al.* (2000).

iron absorption edge, which is not observed (see Figure 3.4).

The same model in a more advanced version, coupling the line profile with the shape and amplitude of the Compton reflection component in Schwarzschild, was successfully applied to BHCs by Życki *et al.* (1997, 1998, 1999) and Done & Życki (1999).

Off-axis flares, which would be expected from magnetic reconnection above the accretion disc, have been considered by Yu & Lu (1999) and Reynolds *et al.* (1999) in Schwarzschild and Kerr metrics, respectively. Of course, most of the line flux is then expected to come from the disc region near to (i.e. just under) the flare, so the flare location can strongly affect the line profile – for instance if it lies over the approaching (or receding) disc side, and so on. Yu & Lu also considered the effect of the motion of the primary source.

Recently, Blackman (1999) and Hartnoll & Blackman (2000a) considered concave and warped accretion discs illuminated from a central point source, computing relativistic line profiles in Schwarzschild metric. The concavity could produce a lensing effect (like a mirror telescope) reinforcing the line flux, and also explain why a sharp iron line is so commonly observed at about the same peak energy in all kind of Seyferts, even if the inclination is expected to shift the line peak: the warping would reduce the sensitivity of the peak location to the disc inclination angle. Warped accretion discs have

been invoked also in some cases (e.g. NGC 4151, see section 4.2) in which the estimate of the disc inclination angle with various methods is ambiguous.

Relativistic computations have been also carried out for substantially different accretion flow assumptions. This was the case of ADAF (Jaroszynski 1997; Jaroszynski & Kurpiewski 1997; Kurpiewski & Jaroszynski 1999, 2000), but of course mainly to the aim to reproduce their *thermal* spectra. It was found that flows around fast rotating BHs generate relatively harder spectra than in the Schwarschild case. As a matter of fact, γ-ray spectral lines due to electron-positron annihilation (cp. section 1.4.3) could also be produced in ADAFs: therefore relativistic line profiles have been computed, too. But, as Jaroszynski (1997) underlined, the observed line shape would mainly reflect the temperature distribution in the inner part of the flow, and *not* its kinematics nor its gravitational state; therefore it is unlikely that relativistic line profiles could ever be a useful diagnostic in the case of ADAFs.

Line profiles have been computed also for relativistic outflows (e.g. jets) around a BH, searching through a large set of geometrical parameters (Wang *et al.* 2000). For different cases of accreting flow geometries and assumptions see also: Hartnoll & Blackman (2000b).

Let us stress an obvious thing: although people because of astrophysical-phenomenological reasons usually refer to the famous iron feature at 6.4 keV, relativistic distortions can be calculated with respect to *any* narrow line or spectral feature.[16] For instance, Cunningham (1975) was considering effects on the thermal spectrum; Hameury *et al.* (1994) were interested in the electron-positron annihilation feature, which is expected in the γ band at 511 keV; Jaroszynski (1997) and Jaroszynski & Kurpiewski (1997) looked for features in ADAFs; and so on. Less likely are applications of the relativistic calculations to features in the optical band, because we do not expect to get any relevant emission in that band from the innermost part of an accreting BH system.

Polarization properties of the spectra from accreting BH sources have also been investigated, although X-ray experiments able to detect such effects are not yet realistic. On this issue, see: Connors *et al.* 1980, Chen & Eardley 1991, Laor *et al.* 1991, Ogura *et al.* 2000, and references therein.

[16] In the case of narrow lines, the results are obviously identical apart from shifting the line rest energy E_0.

Modeling Variability

Variable phenomena, of the kinds already mentioned in section 1.7, could be also addressed in the computations of relativistic spectra.

Let us first of all consider irregular variations in the primary source flux and how they result in the secondary emission (*reverberation*). Stella's work (1990) was the first on this subject, still limited to the static BH case.

Reverberation can be applied to restrict the geometry of the source even in Kerr metric, like in the works by Reynolds *et al.* (1999) and Young & Reynolds (2000), who considered instant flares and their induced variations in the line properties. They took both axisymmetric and off-axis flares into account and reproduced the effects due to the different light travel times from different parts of the source. An instant flaring of the primary source corresponds to line and reflected continuum emission from inwardly and/or outwardly moving rings of illumination (the inwardly moving one will "freeze" at the horizon, producing highly redshifted and delayed emission).[17] Of course, the occurrence of multiple different and overlapping flares would complicate the interpretation of the iron line reverberation.

Periodical variability was considered, too. It can be reproduced by inserting an azimuth-dependent structure in the disc emissivity law. Such a structure can be produced physically by hydrodynamical and magnetic processes, or by perturbations due to external forces, such as tidal interactions with satellites or other bodies.

A typical structure which can be considered in the computations is a corotating spot. This has been done by Karas *et al.* (1992), both with regard to photometry and to the response of the line profile, and again by Karas & Kraus (1996) who underlined how spectrophotometry enables not only to restrict the model's parameters, but also to get an image of the accretion disc (*tomography*).

We already mentioned how spot-related variability computations have been performed also by other authors: among others, by Bao *et al.* (1994), who showed light curves produced by spots on eccentric orbits in Schwarzschild metric, and Bromley *et al.* (1996) who simulated profile variations in Kerr metric.

Sanbuichi *et al.* (1994) considered spiral patterns as another example of

[17] For the preliminary application of this technique see section 4.3 on MCG–6-30-15, and references therein.

non-axisymmetric perturbations. This patterns extend close to the Schwarzschild BH, where GR effects are important and have been calculated by the authors. Karas, Martocchia & Šubr (2000) went further, with a fully relativistic treatment in Kerr metric. Their work has been carried out using again the technique by Karas *et al.* (1992).

Ruszkowski (2000) addressed the issue of a moving primary source by considering a flare which corotates with the accreting flow, and computing the time dependent line profile.

3.5 Relativistic Effects on Illumination and Emissivity

In all the works cited above,[18] the disc emissivity has been taken as $F(r) \propto r^{-q}$. But this power law index q, generally assumed to lie between 1 and 3, is indeed crucial to the final result. The actual disc emissivity law (see section 3.3) is model-dependent, of course.

Even in the framework of a simple *lamp-post model*, variations of s obviously correspond to different conditions of disc illumination. Martocchia & Matt (1996) described the consequences of varying the central source height on the iron line EW. The local emissivity of the disc was computed coupling Matt *et al.* (1991) Montecarlo computations for the local spectrum with the illumination field derived by Martocchia (1996) on the base of a fully relativistic integration of geodesics from the primary source (see also Martocchia & Matt, 1996 and 1997; Martocchia, Matt & Karas 1999; Martocchia, Karas & Matt 2000; Fig. 3.8).

In this model the source distance h becomes – instead of the power law index q – one of the model parameters.

A similar model of illumination has been used by Henry & Petrucci (*anisotropic illumination model*, 1997) and by other authors (Reynolds *et al.* 1999, and references cited therein). Bao *et al.* (1998) used a fixed direction of impinging photons (as if the source were distant, possibly displaced from the rotation axis); however, these authors did not solve the radiation transfer within the disc. This is an important point, as different values of h correspond to substantially different illumination of the disc in the local frame corotating with the matter, and consequently to different emissivity

[18] With this section, we start illustrating the original contributions given by the Author to these issues.

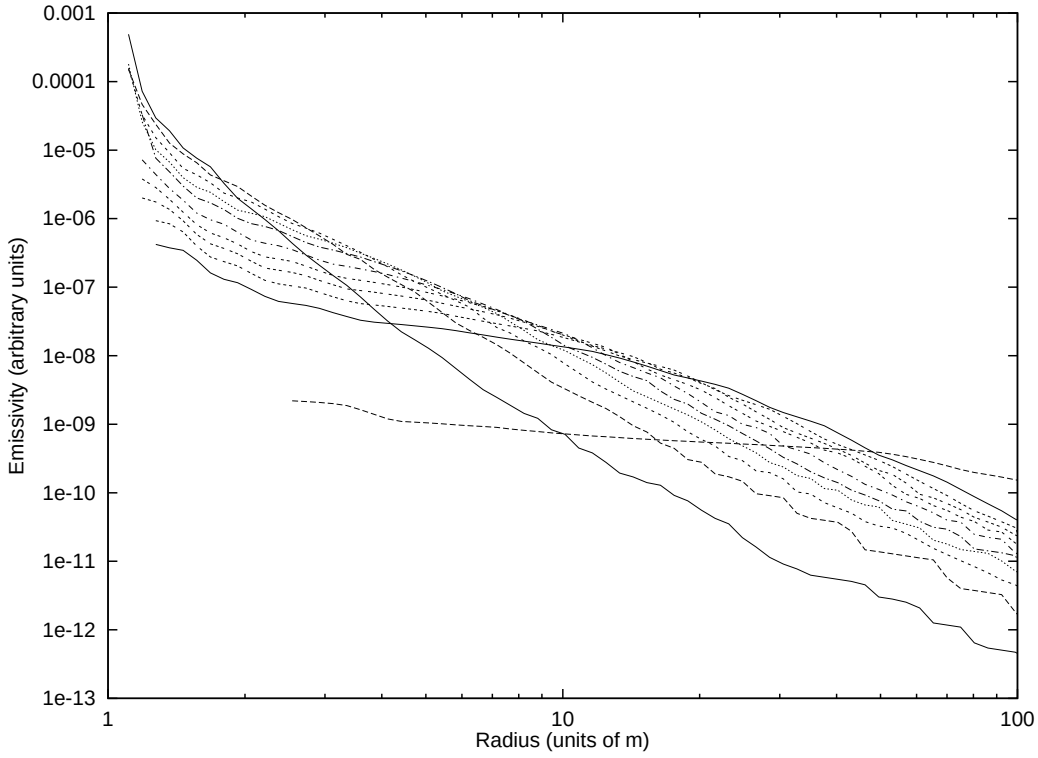

Figure 3.8: Emissivity laws $F_h(r)$ (in arbitrary units) corresponding to different source heights above an extreme Kerr hole, as discussed in Martocchia & Matt (1996, 1997). Looking at the right side of the diagram the curves correspond, from top to bottom, to heights of 100, 20, 15, 12, 10, 8, 6, 5, 4, 3, 2 (units of m). The curves steepen when h decreases, which corresponds to increasing anisotropy of emission.

laws, $F_h(r)$. With decreasing h, the effect of light bending is enhanced and the fraction of X-ray photons impinging onto the disc is increased with respect to those escaping to infinity and contributing to the direct (primary) continuum component. Moreover, photons arriving to the disc at radii $\lesssim h$ are blueshifted, so that the fraction of photons with energies above the photoionization threshold is increased.

A way to discriminate between static and spinning BHs could be based on the fact that the innermost stable orbit $r_{\rm ms}(a)$ of a fast-rotating black hole lies close to the event horizon and approaches the gravitational radius $r_{\rm g} = m$ in the limit of $a \to m$. Highly redshifted features would then represent an imprint of photons emitted at extremely small disc radii, which is possible only near fast-rotating black holes. If the primary source – assumed to be isotropic in its own reference frame – is very close to the black hole, a fraction of photons emitted towards infinity can be deflected by the black hole gravitational field and go to illuminate the accretion disc, thus at the same time increasing the number of X-rays able to produce line emission, and reducing the primary radiation observed at infinity. For static BHs this effect is counterbalanced by the loss of solid angle subtended by the matter to the source when the latter is very close to the BH (Figure 3.9). In fact, the last stable orbit of an accretion disc around a static (Schwarzschild) BH is at $6m$, while for a rotating (Kerr) BH can be as low as m (cp. section 3.1). We showed (Martocchia & Matt 1996) that in this case the increase in the line intensity can be up to a factor $\sim$ a few, and that the increase in the equivalent width can be even more dramatic.

The shape of the photon trajectories in the illuminating radiation field (primary geodesics) is an interesting case study. In Kerr metric the conservation of the angular momentum does not mean, like in the classical and Schwarzschild cases, that geodesics must be planar. On the contrary, what holds in Kerr metric is only the conservation of *the component of the angular momentum which is parallel to the rotation axis*, i.e. λ.

Let us consider a photon emitted by the primary source S, located at a distance h on the BH's axis. Let δ be the angle between this axis and the direction of the photon's emission (its momentum-energy vector). Then λ vanishes,[19] and q^2 is easily derived from (5.13). Thus the integral equations of the motion can be solved (Martocchia 1996, Martocchia & Matt 1997). We can also draw the photon's trajectory down to the equatorial plane (Figures

[19]The choice of the symmetry axis (θ=0) for the emitting point allows to fix one of the four constants of motion, namely λ, which represents the component of the angular momentum along the rotation axis, equal to zero (Carter 1968; see also chapter 2).

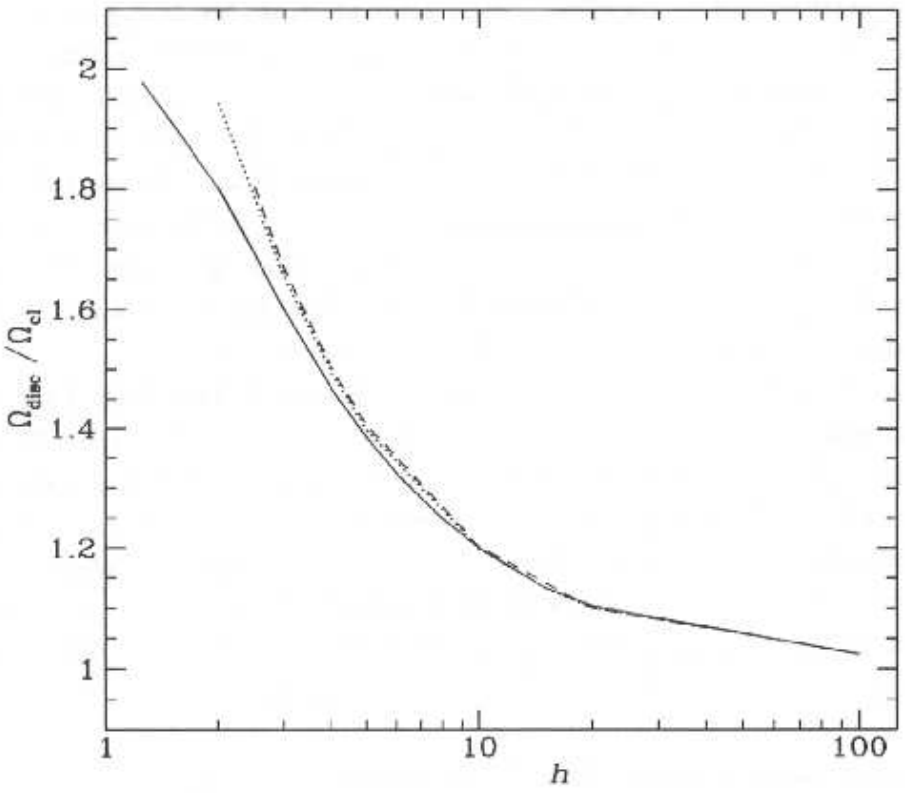

Figure 3.9: Variation with h of the ratio between the solid angle of the radiation which actually illuminates the disc, Ω_{disc}, and the same solid angle as it would come out in a flat spacetime Ω_{cl}, in the assumption that the disc extends up to $r_2 = 1000m$. It is clearly showed that the photon deflection towards the disc, i.e. the anisotropy of the illuminating radiation field, is enhanced with decreasing primary source height. The BH spin also plays a role, especially when the source is low, because it diminishes the inner disc radius (solid line: $a = 1.$; dotted: $a = 0.5$; dashed: static BH). On the other hand, in Kerr metric the photon's deflection has an azimuthal component, too (cp. section 2.2). From Martocchia (1996).

3.10, 3.11). The initial conditions for each trajectory of the primary photons are the source distance h and the emission angle δ, the latter given by:

$$\cos\delta = \pm\frac{V_r^{1/2}(r=h)}{h^2+a^2}. \tag{3.32}$$

(cp. Appendix, eq. (5.13)). The integral equations of the motion can be solved numerically (Martocchia 1996). For each photon, the incident angle in the disc matter reference frame Θ_{inc} and the energy shift $g_{\rm r} \equiv E/E_0$ when reaching the disc are given by (see Appendix, eq. (5.18), (5.23) and (5.24)):

$$\cos\Theta_{inc} = \frac{|q|}{r g_{\rm r}}\sqrt{\frac{\Delta(h)}{h^2+a^2}}, \tag{3.33}$$

$$g_{\rm r} = \sqrt{\frac{\Delta(h)(r^2+a^2+2a^2r^{-1})}{(1-V_{\rm Kepl}^2)\Delta(r)(h^2+a^2)}}. \tag{3.34}$$

The results are quite interesting, especially for low values of h. In Kerr metric, the trajectories do also undergo a deflection in azimuth (i.e. in the ϕ coordinate, thus perpendicular to the sheet's plane and not visible in the figures). This is a sort of screw-motion, or precession around the symmetry axis, due to the fact that the photon "follows the rotation of the metric": at each point (r,θ) on its trajectory, the photon's ϕ angular velocity is

$$\dot{\phi} = \omega = 2amrA^{-1}.$$

In the case $a=0$, $h=3$, $\delta=\frac{\pi}{2}$ we found a circular orbit: this is a known result (e.g. Chandrasekhar 1983), because that value of r corresponds to r_{ph} (section 3.1).

Following the photon's trajectory, one comes onto the accretion disc, where the photon's impinging angle in the local frame of the rotating matter, Θ_{inc}, can be determined; because of the fast rotation of the matter, the photon's incoming angle can be extremely high for low r_{disc}.

The local emissivity is weighted by the factor $f_g = g_{\rm r}^{1.9}$ ($\sim$1.9 being the average photon powerlaw index Γ for Seyfert 1 galaxies, Nandra & Pounds 1994) to take into account the fact that the spectrum, as seen by the matter, is shifted in energy, with consequent change of the number of photons above 7.1 keV, the K-shell photoionization threshold for neutral iron atoms.

The resulting line intensity can be as high as 4 times the classical value, and is greater in any case for h up to $\sim$20. This enhancement is due basically to the following reasons:

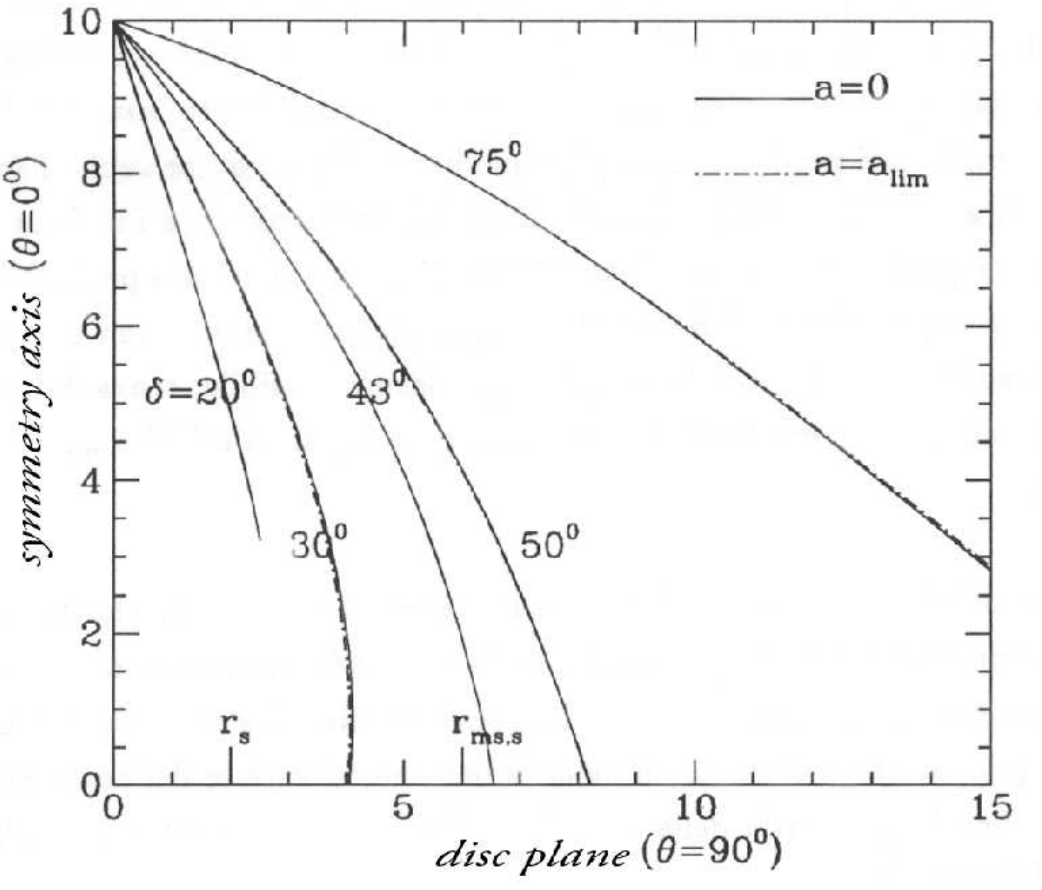

Figure 3.10: Geodesics corresponding to the Schwarzschild and maximal Kerr assumptions follow quite similar paths in the $r-\theta$ plane; however, in the case of a spinning BH, the curved light rays do possess an azimuthal component (perpendicular to the sheet plane) too. From: Martocchia (1996).

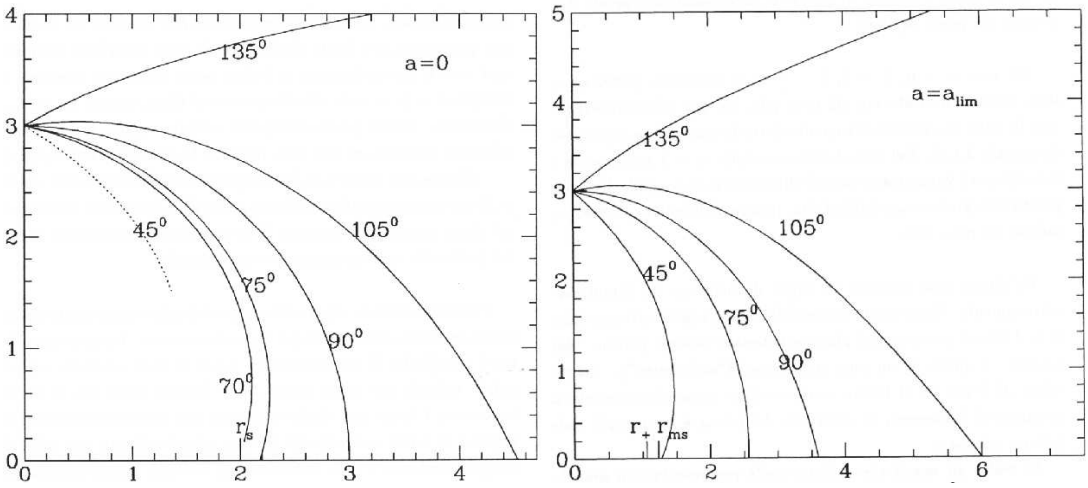

Figure 3.11: Selected geodesics of the primary, illuminating flux are plotted here for a source located at $h = 3m$ in the case of a Schwarzschild BH (left) and for a maximally rotating Kerr BH ($a = a_{\rm lim}$, right). From: Martocchia (1996).

- the fraction of primary photons reaching the disc is increased by the light deflection (of course, this effect increases with decreasing h);

- if $r \lesssim h$, $g_{\rm r}$ is greater than unity, i.e. photons are *blue*shifted and a fraction of photons emitted at h with energies below the photoionization threshold are seen by the matter with energies above the threshold. This increase in $g_{\rm r}$ is due both to the difference in the gravitational potential between the two points, and to the rotation of the matter. Of course, at great radii $g_{\rm r}$ is less than 1 but, at least for small h, these values of the radius have a minor importance because of light deflection.

- typically, photons arrive onto the disc with high incident angles, as seen by the fastly rotating matter (e.g. Cunningham 1976). The efficiency of line emission increases with this angle (e.g. Matt *et al.* 1991).

The equivalent width, i.e. the ratio between the line flux and the continuum specific flux at the line energy as defined in eq. (1.3), is further enhanced by the decrease of the primary continuum due both to the decreasing fraction of primary photons reaching infinity, and to the gravitational redshift which decreases the specific flux at 6.4 keV. Calling $g_{\rm h}$ the ratio between emitted and observed photon energies, for the photon primary radiation we have (cp. Appendix, eq. (5.21)):

$$g_{\rm h} = \sqrt{\frac{\Delta(h)}{h^2 + a^2}}. \tag{3.35}$$

As explained in Martocchia, Karas & Matt (2000), for our work we cur-

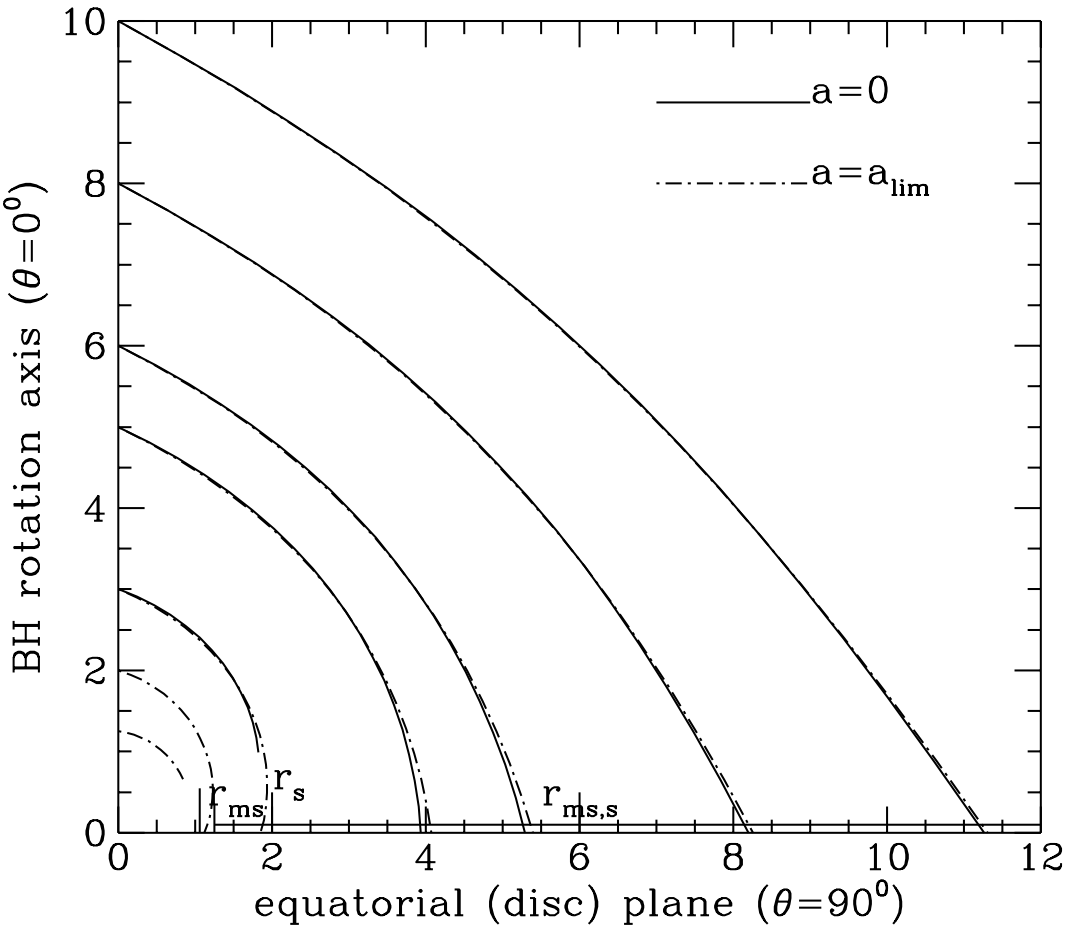

Figure 3.12: From: Martocchia & Matt (1997).

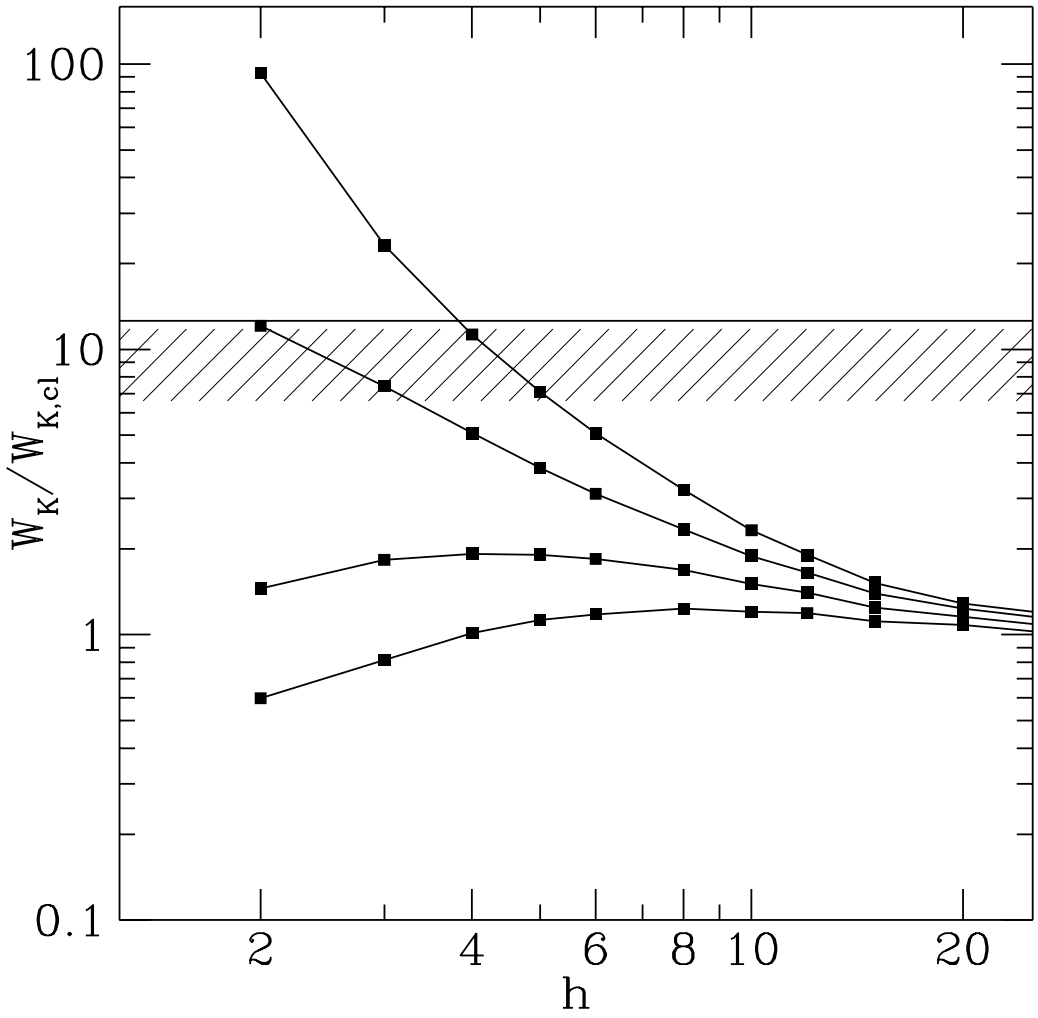

Figure 3.13: The EW – with respect to the primary continuum only – normalized to the 'classical' value, as a function of h. The curves refer to four different values of the inner disc radius: 1.23 (the innermost stable orbit), 2, 4 and 6 (from top to bottom). The shaded area indicates the maximum value when the Compton reflection continuum is taken into account. From Martocchia & Matt, 1996.

rently use the Montecarlo computations of Matt *et al.* (1991), taking into account the energy and impinging angle of the illuminating photons as seen by the rotating matter in the disc. We use the illuminating field computed by Martocchia & Matt (1996) and the mentioned Montecarlo computations to determine the disc emissivity (Figure 3.8) and the local spectra (Figure 3.3) for different values of the involved parameters. In table 3.1 we provide a practical fit of the numerically computed emissivities, which can be useful in calculations. We used a simple fitting law of the type:

$$F_h(r) = c_1 r^{-\lambda_1} + c_2 r^{-\lambda_2} \tag{3.36}$$

Such a function enables to make easy comparisons with the power laws which are commonly used in standard line profile calculations.

3.6 Including the Reflection Continuum

Most of the authors who dealt with line profiles in Kerr metric did not investigate the properties, including relativistic distortions, of the whole Compton-reflected component in the computed spectra. Nevertheless, this is the only way to evaluate the line EWs properly.

The iron line detected in the spectrum of MCG–6-30-15 – as well as its very peculiar profile during the spectral state of the source considered by Iwasawa et al. (1996b) – have been derived from the data subtracting a continuum which does not possess the broad trough due to the relativistic smearing of the iron edge. For this being the case of all similar observations up to now, we think it is particularly important to look for combined effects on both line and reflected continuum and possibly get line profiles after self-consistent subtraction of the underlying Compton reflection. Another reason for looking at combined effects is that the number of assumptions and hypotheses made for computing relativistic spectra from accreting BH sources has grown in such a way that it becomes more and more difficult to use any peculiarity of the line profiles alone in order to get direct informations on the physics of the system, because the calculations show that analogous effects can be in principle produced by a variety of factors. Thus comparisons between satellite data and spectra or profiles resulting from self-consistent computations have a higher level of confidence, in particular when considering line integral quantities like centroid energy, line width and – above all – the equivalent width.

Usually, even when the underlying continuum was considered, calculations of light propagation were performed in the metric of *static* BHs. Matt *et*

	c_1	λ_1	c_2	λ_2
$h = 2m$	0.02268	38.38706	0.000122	6.14786
$h = 3m$	0.00146	24.47516	0.000059	0.00006
$h = 4m$	0.00324	30.85495	0.000039	4.70109
$h = 5m$	0.00640	35.36543	0.000025	4.49187
$h = 6m$	0.00968	34.27642	0.000013	3.75576
$h = 8m$	$0.27139\text{x}10^{-4}$	8.74175	$0.01662\text{x}10^{-4}$	1.74206
$h = 10m$	$0.99815\text{x}10^{-5}$	6.05660	$0.04793\text{x}10^{-5}$	1.14952
$h = 12m$	$0.42940\text{x}10^{-5}$	4.42939	$0.01590\text{x}10^{-5}$	0.81154
$h = 15m$	$0.27182\text{x}10^{-5}$	4.64923	$0.01451\text{x}10^{-5}$	0.89655
$h = 20m$	$0.98182\text{x}10^{-6}$	3.66965	$0.05796\text{x}10^{-6}$	0.72744
$h = 100m$	$0.59002\text{x}10^{-5}$	1.05533	$-0.59023\text{x}10^{-5}$	1.05622
$h_{\rm cl} = 5m$	$0.10084\text{x}10^{-4}$	0.29168	$-0.09948\text{x}10^{-4}$	0.28796

Table 3.1: Results of fitting the emissivity laws $F_h(r)$ for different source heights (refer to the text for details). All coefficients have been obtained for a maximally rotating hole, except for the row $h_{\rm cl}$=5m which refers to the purely classical (i.e. Euclidean) case with the rays not distorted by gravitation. For $r > 6m$ (which is the case of stable orbits in Schwarzschild metric) the emissivity is not very much affected by the BH spin, while the effect of rotation is clearly non-negligible for small values of h. From Martocchia, Karas & Matt (2000).

al. (1991) adopted a weak-field approximation. In 1998 Maciołek-Niedźwiecki & Magdziardz and Bao *et al.* made use of fully relativistic codes, but again in Schwarzschild metric; the same with Young *et al.* (1998). Done *et al.* (1998) and Życky *et al.* (1997, 1998, 1999) calculated both line and reflected continuum in Schwarzschild metric giving evidence to the relativistic smearing, too, with regard to some BHCs (V404 Cyg, Nova Muscae, Cyg X-1). The reflection component in a lamp-post model has been calculated also by Malzac *et al.* (1998).

Ross *et al.* (1999) calculated distortions in Kerr metric for different ionizations states, but without accounting for the relativistic effects on the primary radiation.

Fully relativistic, self-consistent calculations of iron lines and continuum together in the case of a Kerr spacetime were missing until our work on the subject (Martocchia, Karas & Matt 2000), which is described in this section.

We adopted the illumination model, local spectra and emissivities described in the previous section, and employed a ray-tracing code which computes all required photon geodesics, i.e. the photon paths from the accretion disc to the observer, in each run, adapting the code by Karas (Karas & Kraus 1996).

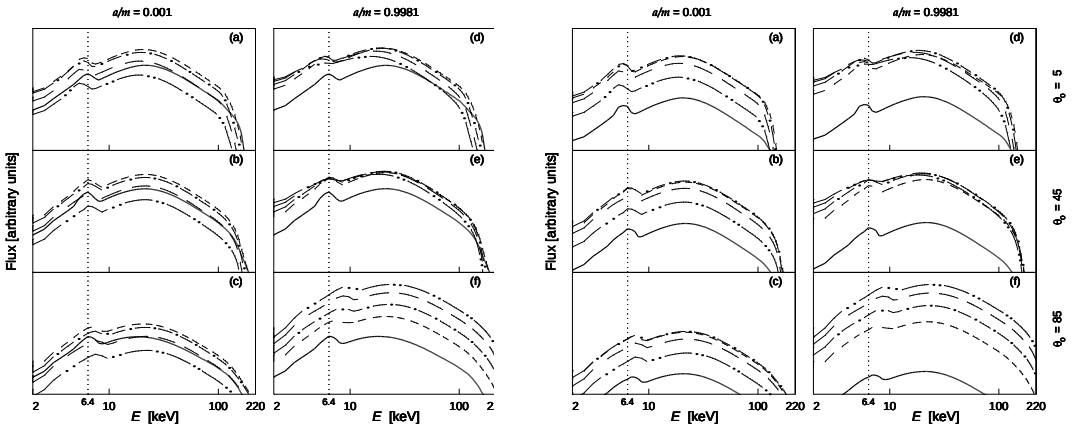

Figure 3.14: Examples of broad-band (2–220 keV) spectra for three inclination angles ($\theta_0 = 5$, 45, and 85 degrees). The following types of lines have been used in this graph to indicate the source height (in Boyer-Lindquist coordinates): $h = 100m$ — thick solid line; $h = 20m$ — short-dashed; $h = 10m$ — dot-dashed; $h = 6m$ — long-dashed; $h = 4m$ — double-dot-dashed. Left panel corresponds to a slowly rotating black hole, while right panel shows the case of rapid rotation, as indicated on the top. Here we considered a disc extending down to the innermost stable orbit. Outer edge is at $r_0 = 100m$. On the right panel, the case $r_0 = 34m$ is showed.

As an effect of the Doppler shift of the photons, even the continuum emission as a whole is distorted, more and more broadened with increasing inclination. The results can be seen in Figure 3.14, and following. Apart from affecting the line profile in the expected way, these shifts towards lower or higher energies also cause the smearing of the photoelectric edge into a broad trough. Therefore both the line and the iron edge are progressively smoothed down with increasing inclination. This behavior is in qualitative agreement with previous claims (i.e. Sincell 1998, who considered the distortion of the Lyman edge in Kerr metric).

The effects of inclination on the smearing and smoothing of all spectral features may be dramatic in Kerr metric not only because of substantial energy shifts of photons emitted at the innermost radii, but also due to the mutual combination of this effect on both the iron line and the underlying continuum. The spectral features spread across a broad range of energies and may become difficult to distinguish from each other.

In the other accompanying figures, also taken from Martocchia, Karas & Matt (2000), we show the spectra in a narrower band ($2 \div 12$ keV) to gain a better "resolution" of the line profiles corresponding to different h. It is evident that the effects of the anisotropic illumination can be enormous, causing

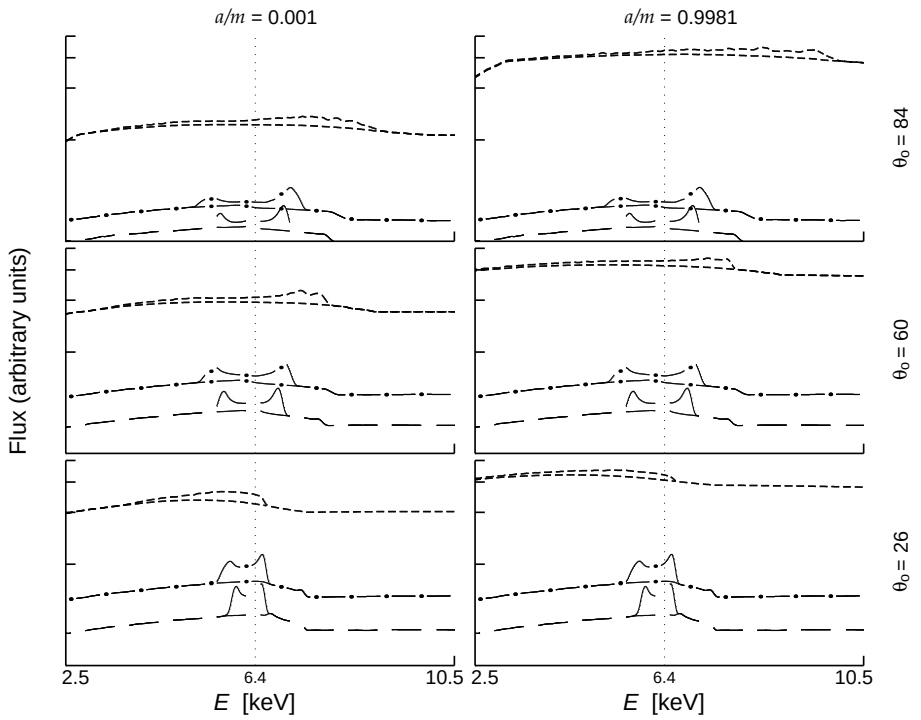

Figure 3.15: Contributions to the total profile for $h = 6m$ from three subsections of the disc are shown in this figure: r/m extending from $r_{\rm ms}$ up to 34 (short-dashed), 34–67 (dash-dotted), and 67–100 (long-dashed). Underlying curves of the reflection continuum are also plotted. Three values of inclinations (corresponding to $\cos\theta_{\rm o} = 0.1,\ 0.5,\ 0.9$) are considered. Vertical scale is logarithmic.

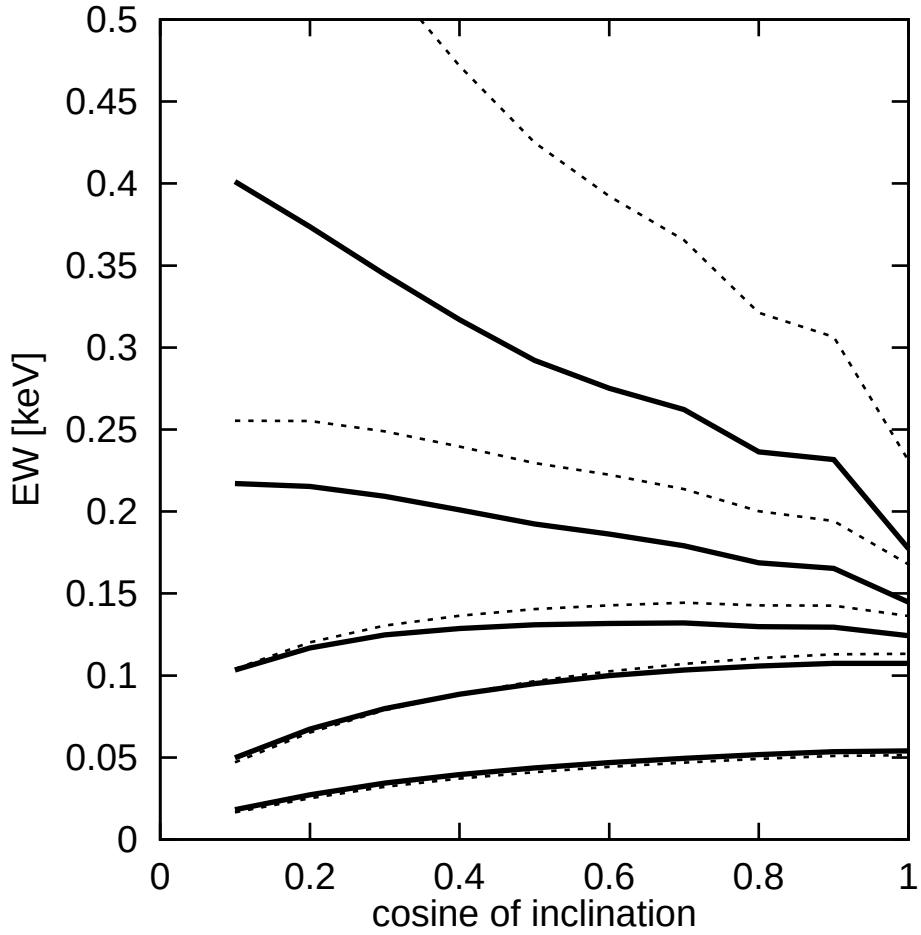

Figure 3.16: Equivalent width versus cosine of the observer's inclination angle, for different illuminations and a disc extending from the innermost stable orbit up to $100m$. The solid lines refer to EWs with respect to the total underlying continuum, the dashed ones to EWs with respect to the direct contribution only. From top to bottom, the curves are for a source located at $h/m = 4$, 6, 10, 20, and 100, respectively. The BH spin parameter is $a/m = 0.9981$. The EW curves we obtained for the static BH case are in agreement with those of Matt *et al.* (1992). From: Martocchia, Karas & Matt (2000).

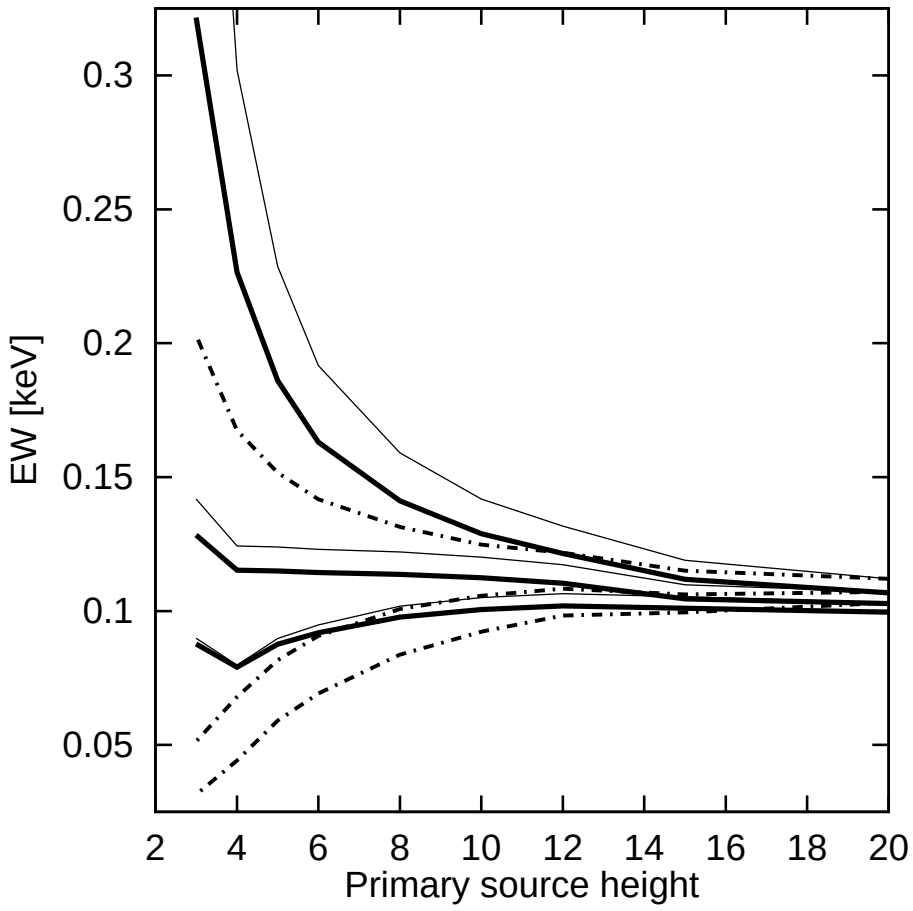

Figure 3.17: EW dependence on the source height h, for an observer inclination fixed at 30 degrees and a disc extending from the innermost stable orbit up to $100m$. Three values have been considered of the black hole spin (from top to bottom): $a = 0.9981m$, $0.5m$ and $0.001m$. See the text for more details.

a substantial amount of the re-emitted flux to be highly redshifted, especially in the low-h case. When the source is very close to the black hole, because of strong anisotropy only the innermost part of the disc contributes to the line and to the reflection continuum fluxes. As a consequence, these spectral components can be very intense in Kerr metric, whereas in the Schwarzschild case they gradually disappear with decreasing h if no efficient reemission is allowed from $r < 6m$.

Clearly, the emissivity law is a key ingredient in the calculations of reflected spectra. Flat local emissivity laws apply when the source is distant from the hole ($h \gg r_{\rm g}$), and produce spectra which show very weak dependence on the black hole angular momentum. On the other hand, with steep emissivities (low h) the observed spectra strongly depend on a.

The detailed line profiles contain a wealth of information which can in principle be compared with data, but it may be useful to describe them also by *integral quantities* which can be determined even from data with just moderate energy resolution. We considered the line equivalent width (EW), defined as (1.3), the centroid energy ($E_{\rm cen}$), and the geometrical width (σ).

In our calculations we also accounted for the effect of the light-rays distortion on the primary flux, i.e. for the fact that the solid angle Ω of the direct continuum which escapes to infinity diminishes considerably when the source is near the black hole (low h). This is accounted for by introducing an h-dependent factor $f(h) = \Omega_{\rm inf}/\Omega_{\rm inf,cl}$ which multiplies $F_{\rm dir}$ in the definition of EW. As expected, f approaches unity if the source is far away from the hole, which mimics a flat spacetime.

We show (table 3.2) a table of such computed line integral quantities; here we consider selected values of the parameters h and i. We also write down approximated analytical laws for the same parameters, as they come out from the calculations, in the form of quadratic polynomials:

$$a_0 + a_1\, h/m + a_2\, (h/m)^2$$

(the coefficients are given in table 3.6). These can approximate h-dependences in the range $4m \leq h \leq 20m$ with sufficient accuracy.[20]

Figure 3.16 shows the equivalent width as a function of the cosine of inclination, $\mu = \cos(i)$. The slope of EW(μ) gets inverted at $h \sim 10m$: for larger values of h we obtain EW *decreasing* with μ, as in the Schwarzschild

[20] For the whole interval, up to $h = 100m$, we used more precise spline fits; the corresponding MATLAB script, which can be used for the numerical inversion to obtain the parameters of the model (i.e. a/m, $\theta_{\rm o}$, and h/m, in terms of the three observables), is available from the authors on request.

$\cos\theta_o$		$h=4m$		$h=6m$		$h=10m$		$h=20m$		$h=100m$	
	E_{cen}	7.65	(6.77)	7.45	(6.73)	7.18	(6.64)	6.78	(6.52)	6.44	(6.44)
0.1	σ	1.71	(1.29)	1.71	(1.27)	1.62	(1.17)	1.31	(0.96)	0.64	(0.61)
	EW	401	(30)	217	(35)	103	(38)	50	(36)	18	(18)
	E_{cen}	6.50	(6.65)	6.56	(6.63)	6.56	(6.57)	6.49	(6.47)	6.38	(6.38)
0.3	σ	1.63	(1.26)	1.56	(1.23)	1.38	(1.14)	1.07	(0.96)	0.64	(0.62)
	EW	345	(58)	209	(66)	125	(72)	80	(68)	34	(34)
	E_{cen}	5.71	(6.36)	5.97	(6.36)	6.17	(6.35)	6.29	(6.34)	6.34	(6.34)
0.5	σ	1.50	(1.13)	1.42	(1.10)	1.23	(1.02)	0.95	(0.86)	0.58	(0.57)
	EW	292	(72)	192	(82)	131	(89)	95	(85)	44	(43)
	E_{cen}	5.08	(6.01)	5.47	(6.03)	5.82	(6.08)	6.09	(6.17)	6.27	(6.27)
0.7	σ	1.35	(0.93)	1.26	(0.91)	1.08	(0.84)	0.82	(0.71)	0.48	(0.47)
	EW	262	(77)	179	(88)	132	(97)	103	(95)	49	(49)
	E_{cen}	4.53	(5.64)	5.01	(5.68)	5.49	(5.79)	5.88	(5.97)	6.19	(6.19)
0.9	σ	1.20	(0.67)	1.11	(0.65)	0.92	(0.61)	0.66	(0.51)	0.33	(0.31)
	EW	232	(79)	165	(91)	130	(101)	107	(100)	53	(53)

Table 3.2: Integral quantities which characterize the iron Kα line profiles: centroid energy and geometrical width (in keV), and EW with respect to the *total* continuum (in eV). Comparison is possible between corresponding quantities for a fast-rotating and a non-rotating (in parenthesis) BHs. These results refer to a disc extending from the innermost stable orbit up to 100 gravitational radii. From Martocchia, Karas & Matt (2000).

$\cos\theta_o$		a_2		a_1		a_0	
	E_{cen}	0.00243	(0.000594)	-0.112	(-0.0301)	8.05	(6.88)
0.1	σ	-0.00103	($-8.77\text{x}10^{-5}$)	-0.000877	(-0.019)	1.74	(1.37)
	EW	2.85	(-0.0979)	-88.8	(2.68)	687	(21.4)
	E_{cen}	-0.0011	(0.000198)	0.0251	(-0.0162)	6.43	(6.71)
0.3	σ	0.000643	(0.000111)	-0.0509	(-0.0217)	1.83	(1.35)
	EW	2.07	(-0.173)	-65.1	(4.74)	555	(42.6)
	E_{cen}	-0.00414	($3.69\text{x}10^{-5}$)	0.134	(-0.00223)	5.27	(6.37)
0.5	σ	0.00104	(0.000136)	-0.0598	(-0.0203)	1.73	(1.21)
	EW	1.5	(-0.206)	-47.4	(5.68)	445	(53.6)
	E_{cen}	-0.00614	(-0.000161)	0.208	(0.014)	4.38	(5.95)
0.7	σ	0.00118	(0.000111)	-0.0616	(-0.0167)	1.58	(0.999)
	EW	1.21	(-0.224)	-38.3	(6.44)	384	(55.8)
	E_{cen}	-0.00769	(-0.00042)	0.266	(0.031)	3.62	(5.52)
0.9	σ	0.00127	($1.34\text{x}10^{-19}$)	-0.0647	(-0.01)	1.44	(0.71)
	EW	0.952	(-0.239)	-30	(6.98)	327	(56)

Table 3.3: Coefficients of the least-square polynomial fits to h-dependences of E_{cen}, σ and EW, as predicted in our model. Angular-momentum parameter is $a = 0.9981m$; for comparison, the values resulting from computations with Schwarzschild metric are given in parentheses. From Martocchia, Karas & Matt (2000).

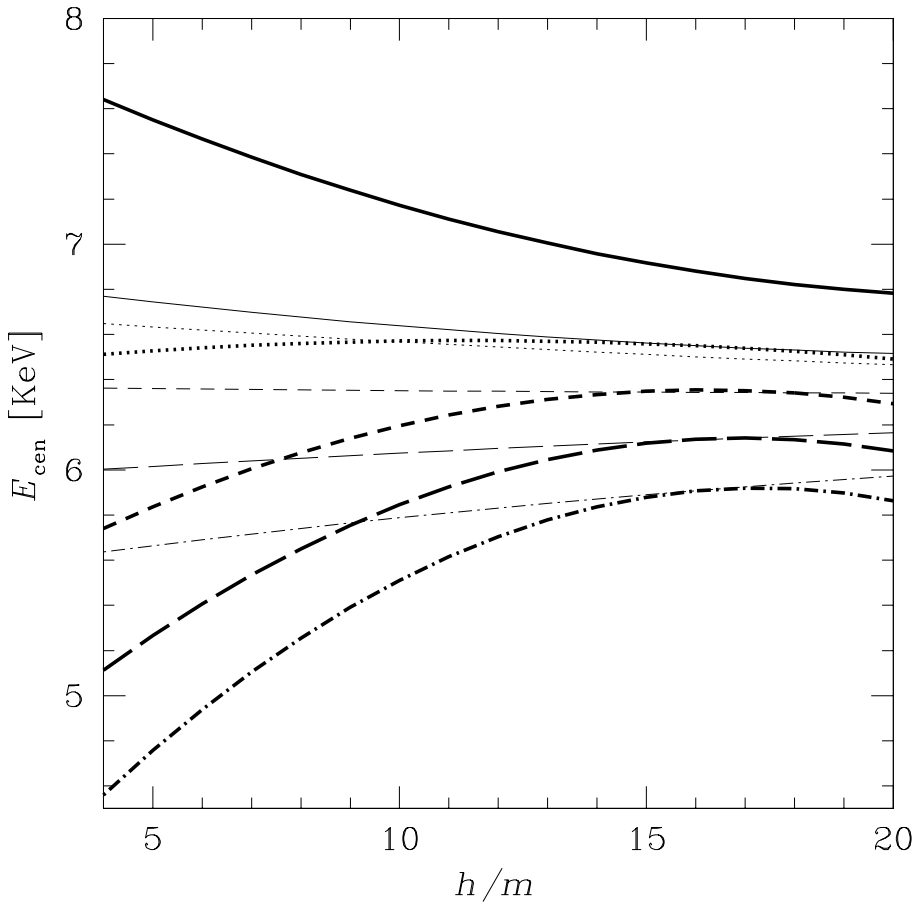

Figure 3.18: Centroid energy dependence on h for $cos(i) = 0.1, 0.3, 0.5, 0.7$ and 0.9 (from top to bottom), both for a static (thin) and a maximally rotating (thick) BH. Units of the vertical axis are keV. From: Martocchia, Matt & Karas (1999).

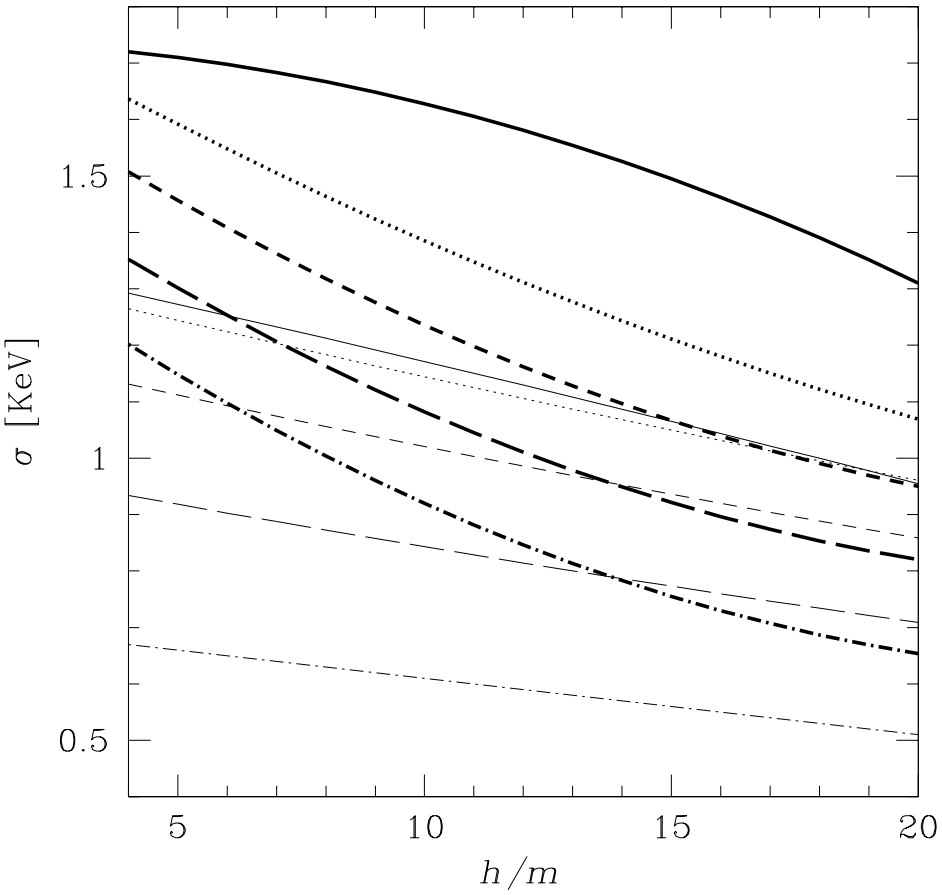

Figure 3.19: Geometrical line width (in keV) with varying h. Line conventions are the same as in the previous figure. From: Martocchia, Matt & Karas (1999).

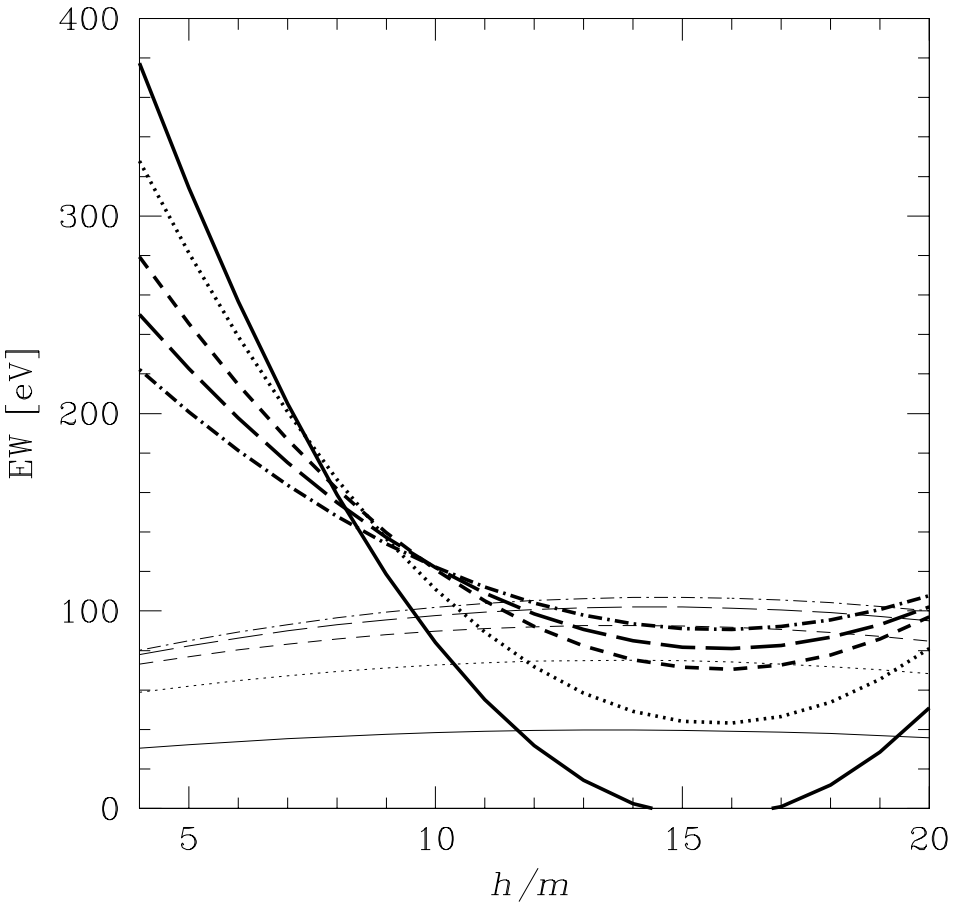

Figure 3.20: Equivalent Width dependence on h. Line conventions are the same as in the previous figures – but notice that for h bigger than ~ 8 the angle dependence gets inverted! Here the EW is expressed in eV. From: Martocchia, Matt & Karas (1999).

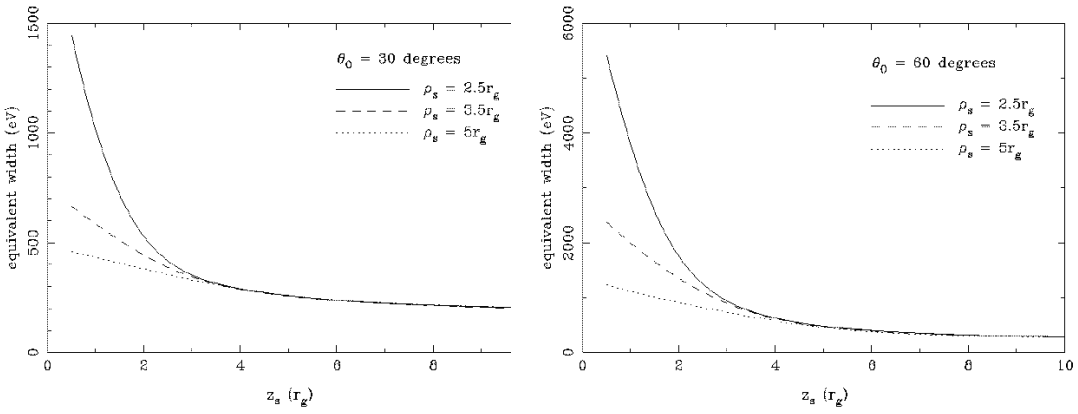

Figure 3.21: The iron line EW – here plotted as a function of the source height – can reach very high values in the model by Dabrowski & Lasenby (2000). Here the primary source is off-axis, above the approaching side of the disc, for three different distances from the axis itself. The BH is a maximally rotating Kerr one and the observer is at 30 (left) or 60 (right) degrees of inclination. From Dabrowski & Lasenby, 2000.

case, whereas for $h \lesssim 10m$ EW *increases* when μ decreases. This is a direct consequence of both the large efficiency of line emission and the enhanced influence of light bending from the innermost Kerr orbits, which strongly affects the profiles. This behavior is less pronounced when EWs with respect to the *total* continuum (direct plus reflected; cf. solid lines) are considered, the reason being that the Compton-reflected contribution $F_{\rm ref}$ increases together with the line contribution, $F_{\rm line}$, when the primary source height decreases, and eventually dominates.

In Figure 3.17, EWs versus three different definitions of the continuum are shown for the sake of illustration: thick solid lines refer to EWs with respect to the total underlying continuum, taking into account the solid angle distortion due to the spacetime curvature; thin solid lines have been computed in a similar manner, but with respect to the direct continuum only; finally, the dash-dotted lines have been plotted with respect to the direct continuum only, and they do not include the solid angle distortion effect. It is worth noticing that, due to efficient emission from the innermost region, in the extreme Kerr case one obtains EW values very much enhanced at low h's.

Recently, a paper by Dabrowsky & Lasenby (2000) has appeared with similar motivation as ours, regarding self-consistent computations which include also the continuum component, and aimed in particular to estimate

the effects on the line EW (see Figures 3.21). In this work, Dabrowski & Lasenby considered both on- and off-axis flares. However, the spectra which are showed there do not include the underlying *reflected* continuum, and the EW computations do not seem to take it into account, either (only the direct power-law component seems to have been considered there). Therefore the EWs may be seriously overestimated, because, as explained before and in Martocchia & Matt (1996), the reflected continuum will grow together with the line.

In their computations, the authors use a gauge-theoretic formalism which allows calculations to be performed in an easy-to-handle flat-similar space (see the paper, and references therein; also: Lasenby *et al.*, 1997).

3.7 The kerrspec Tool

The computation of "synthetic" line profiles and spectra would not be fully exploited if it were not possible to use it for the practical purpose of fitting observational data. To this aim, a large number of spectra has to be computed, even if one restricts the parameter region as far as possible, in a short time. Thus a big number of geodesics has to be pre-calculated and stored in a catalogue, where they can be accessed fastly.

The radius dependence, the angle dependence as well as the frequency dependence (local spectrum) of the local emission can be given as inputs; after fixing the desired resolution in the image plane, the geodesics corresponding to all image points are sorted-out from the catalogue, which is of the kind described by Karas *et al.* (1992) (section 3.4). Karas *et al.* work was actually refined to have a better confidence on the trajectories lying very near to the BH horizon (below $6m$). This because the computed line profiles are strongly sensitive to the radius of the innermost emitting orbit, especially if the emissivity varies rapidly with the radius. The innermost emitting orbit is usually identified with the marginally stable one, which depends on the BH angular momentum.

The routine, which has been called kerrspec and works within the standard XSPEC package for the fitting of X-ray data, [21] allows to adjust or fit over the following parameters and assumptions:

- Spacetime: static or spinning BH. A sub-section of the catalogue can be constructed for every a of interest.

[21] http://heasarc.gsfc.nasa.gov/docs/xanadu/xspec/manual/manual.html

- Inclination of the distant observer: we are currently using 10 catalogues for $\mu = \cos(i)$ between 0 and 90 degrees, with regular steps $\delta\mu = 0.1$.

- Local radiation flux, $F(r)$. One may examine:

  (i) power-law dependence $F_q(r) \propto r^{-q}$ ($q = \text{const}$);

  (ii) standard Novikov-Thorne-Page model (Novikov *et al.* 1974);

  (iii) illumination from a central source (Martocchia & Matt 1996). In this case the parameter is h; the correspondent emissivity law (see also Figure 3.8) is stored in a file;

  (iv) analytical approximation for case (iii), as explained in the previous section (and table 3.1).

- Disc size (inner edge r_1, outer edge r_2).

- Emissivity profile in frequency, $\varphi_1(\nu_e)$. We included:

  (i) Narrow-Gaussian profiles $\varphi_1(\nu_e) \propto \exp[-\varepsilon(\nu_e - 1)]^2$ ($\varepsilon = \text{const}$). Frequency profile is normalized to maximum at unit local frequency (thus the term $\nu_e - 1$);

  (ii) Delta-function profiles;

  (iii) Numerically computed profiles and broader spectra, in order to self-consistently take into account the underlying reflected continuum, as explained in the previous section (Montecarlo computations by Matt *et al.* 1991);

  (iv) Any other analytical form for the local spectrum.

- Angular dependence of the local emissivity, including possibly a limb-darkening law. We examined:

  (i) the functional forms for fluorescent and Compton-reflected emission given by Ghisellini *et al.* (1994), see 3.20, 3.21;

  (ii) the numerically-derived dependence on the radius, from the Montecarlo computations by Matt *et al.* 1991.

For the initial purposes we have restricted ourselves to the case of geometrically thin discs; however, because in the catalogues the whole shape of each geodesic is stored, it is easy to consider a different disc shape, i.e. some law for the disc thickness, in the form of a function $z(r)$ ($z = 0$ for an equatorial disc). Also, a radial component for the velocity of the accreting matter, for instance an advection velocity component, can be easily introduced into the model.

Table 3.4: A typical screen with the parameters and settings for the kerrspec routine in XSPEC. The model used here is: model = wabs(powerlaw + kerrspec). See the text for further explanation.

Model par	Fit par	Model comp	Component	Parameter	Unit	Value	Data
1	1	1	constant	factor		1.000	frozen
2	2	2	wabs	nH	10^{22}	2.043	+/- 0.0000E+00
3	3	3	powerlaw	Γ		1.958	+/- 0.0000E+00
4	4	3	powerlaw	norm		1.8544E-02	+/- 0.0000E+00
5	5	4	kerrspec	a/m		0.9981	frozen
6	6	4	kerrspec	$cos(i)$		0.8700	frozen
7	7	4	kerrspec	h/m		20.00	frozen
8	8	4	kerrspec	r_1/m		1.230	frozen
9	9	4	kerrspec	r_2/m		104.6	+/- 0.0000E+00
10	10	4	kerrspec	dr		1.000	frozen
11	11	4	kerrspec	$dpsi$		1.000	frozen
12	12	4	kerrspec	norm		1.7851E-03	+/- 0.0000E+00

Table 3.4 resembles a typical screen with the parameters and settings for kerrspec during XSPEC running. The parameters of kerrspec have obvious meaning, apart from dr and $dpsi$, which determine the resolution on the image plane, thus the quality of the calculated spectrum but also the computing time. More hidden parameters – e.g. the gravitational redshift and the parameters to set the numerical precision and computational time – are contained in the code itself and auxiliary files. At the beginning of a computation, the routine also asks for the local spectrum model to be used.

Typically, the code takes a few hours to fit a spectrum employing curved geodesics in the very vicinity of the BH, i.e. accounting for radiation emitted at distances of the order of m from the event horizon.

Chapter 4

Comparison with Data

4.1 A Brief History of X-ray Missions

Before illustrating the results that we obtained by fitting recent satellites data of a few relevant X-ray sources, it is useful to review the status of the observations in the X-ray band, and to discuss what is needed and expected from the next generation missions.[1]

Historically, the first X-ray source – apart from the Sun – to be discovered was also the brightest of the X-ray sky, i.e. Scorpius X-1; this happened in 1962 by means of a rocket flight (Giacconi *et al.* 1962). However, only satellite missions could permit the systematic study of the sky in this energy band. The satellite *Uhuru*, launched in 1970, operated for three years, providing fundamental information on important sources, like Cyg X-1, and discovering that AGN and clusters of galaxies are strong X-ray emitters.

NASA operated the *HEAO* mission, which covered the $1 \div 30$ keV band, from 1977 to 1979. The *HEAO-2* satellite, launched in November 1978 and later called *Einstein*, was the first to have an X-ray telescope onboard, to perform X-ray imaging for the first time. In the early 80's, another basic mission was launched, named *EXOSAT*. The European-German "Roentgen Satellite" *ROSAT* came afterwards, to work mainly in the soft X-rays.

The Japanese *Ginga* was the first to provide information on the complex, multi-component structure of the Seyferts' X-ray spectra, yielding interesting data of Sy-1s' iron emission lines and discovering the Compton-reflected

[1] Here we concentrate only on the missions aimed to good energy resolution, as required by the particular research we carry on. A full list of high-energy missions and experiments can be found at http://heasarc.gsfc.nasa.gov/docs/heasarc/missions/alphabet.html

component (Pounds *et al.* 1990, Matsuoka *et al.* 1990). However, *Ginga* data were unable to determine the width, not to mention the profile, of the lines.

An appreciable energy resolution became available only when *ASCA* was launched.[2] *ASCA* (formerly *Astro-D*) is Japan's fourth cosmic X-ray astronomy mission, but with a participation by the USA. The satellite was successfully put into orbit on February 20, 1993, and has just ceased operations. Its instruments could resolve data at $E \sim$ a few keV with $\Delta E = 160$ eV. *ASCA* data of AGN are now free available from the *Tartarus* archive.[3]

A broader spectral coverage, from ~ 0.1 keV with LECS up to ~ 200 keV with PDS, has been possible thanks to the Italian-Dutch satellite *BeppoSAX*. Its name is the acronyme for "Satellite per Astronomia X", and "Beppo" in honor of Giuseppe Occhialini. The energy resolution is poorer than that of *ASCA*. Thanks to *BeppoSAX*, previous results on the iron line have been confirmed and the underlying continuum has been better constrained.[4] Moreover, high-energy detectors onboard *BeppoSAX* have given fundamental results on Gamma Ray Bursts. For an overall description of the *BeppoSAX* mission see Boella *et al.* (1997) or: http://www.sdc.asi.it/.

While results in the soft and medium X-rays are now being extended and improved by *Chandra* and *XMM* (see next)), in hard X-rays *BeppoSAX* results will be unrivalled for many years.

Chandra[5] – formerly known as *AXAF* – was launched with a Shuttle in July 1999, and is already giving a very good performance as an imaging instrument, with a resolution of 0.5 arcsec, i.e. an improvement by an order of magnitude with respect to *ROSAT*, and a good sensitivity in the $0.1 \div 10.$ keV energy range. Its gratings are providing important results on narrow absorption and emission lines, thanks to an energy resolution of the order of a few eV (to be compared to resolutions of about 150 eV typical of CCD detectors).

Shortly afterwards, in December 1999, the European *X-ray Multi Mirror* telescope[6] (*XMM*), now called *XMM-Newton*, has been launched by an Ariane 5. *XMM-Newton* has a very good sensitivity and is suitable for spectroscopy, but the best energy resolution is at energies below ~ 3 keV. In the band of the iron line features, the data will have comparable resolution with

[2] http://heasarc.gsfc.nasa.gov/docs/asca/ascagof.html
[3] http://tartarus.gsfc.nasa.gov/
[4] See for instance the following section on MCG–6-30-15.
[5] http://chandra.harvard.edu/
[6] http://www.astro.estec.esa.nl/XMM/

those obtained by *ASCA*, but a much higher throughput.

Much interest had also arisen about the Japanese mission *ASTRO-E*, that should have had both a good sensitivity and an energy resolution $\Delta E \sim 10$ eV. Unfortunately the mission has failed because of an accident during the launch, but there is some hope that it will be relaunched in a few years.

For the study of time properties, since 1996 an unrivalled instrument is the *Rossi X-ray Timing Explorer*[7] (*RXTE*). Following its great success – especially in analyzing variability properties of BHCs and discovering new QPOs (e.g. Van der Klis 1998) – even more advanced X-ray timing mission are currently under study which should at the same time improve sensitivity and both spectral and angular resolution.

Next Missions

X-ray astronomy has developed very fast in the last 30 years. Following the interest arisen by the large amount of data which became available, and the outstanding theoretical effort devoted to their interpretation, a future generation of X-ray observatories has been planned. They will improve the sensitivity, the spectral and angular resolutions which have been reached with the current missions.

The NASA-born project *Constellation-X*,[8] a satellite which should provide a sensitivity 100-times better than any past or current X-ray mission, a spectral resolution $E/\Delta E \sim 300 \div 3000$ in the range 0.25 to 10 keV, and imaging capabilities in the $10 \div 40$ keV band, should be launched in the year 2008.

The European *XEUS* project will represent a further great leap forward for X-ray astronomy: 2" spatial resolution at 1 keV, and a sensitivity 250 times better than *XMM*.[9] However, if approved, it will take at least a decade to see it operating. The project is under study as a part of the Horizon 2000+ program to utilize the International Space Station for astronomical applications.

In a more distant future, the X-ray interferometry mission *MAXIM*[10] is

[7] http://heasarc.gsfc.nasa.gov/0/docs/xte/xte.html/
[8] http://constellation.gsfc.nasa.gov/
[9] http://astro.estec.esa.nl/SA-general/Projects/XEUS/
[10] http://maxim.gsfc.nasa.gov

intended for an astonishing spatial resolution of the order of 10^{-6} arcsec, which can be achieved with relatively short baselines (some meters) because of the short X-ray wavelenghts: the aim is to allow imaging of BH systems on the scale of a few gravitational radii (10^{-4} arcsec for a nearby galaxy like M87; for a discussion see e.g. Ozel & Di Matteo 2000).

In a higher energy band, the *Integral* mission[11] is expected to give new results, following the path of missions like *Sigma*, *Granat*, *Compton-GRO*. To our aims, its data will be useful to study possible relativistic distortions in the electron-positron annihilation line at ~ 0.5 MeV.

4.2 General Notes on the Fits

In this chapter we present the first results obtained fitting X-ray data with the kerrspec tool. We considered some of the best-known galactic and extra-galactic BH candidate sources, paying attention to relativistic distortions on the iron line profiles. The computations we deal about in this chapter had two main scopes: first, test the functioning of the newly developed numerical tool; secondly, see whether the fast-spinning BH assumption is required by the data or not. Also further preliminary fits have been performed including the underlying reflection continuum; however, these fits should be repeated more carefully and with a complete coverage of the parameters space, due to the long computational time required when using numerical tables for the local broad-band spectra.

We assumed an optically thick, neutral, and geometrically thin Keplerian accretion disc with solar elemental abundances (see the previous chapter for further details).

The data are taken from the *ASCA* and *BeppoSAX* archives.

Let us first of all stress some more technical points which have to be considered in all fits:

1. The XSPEC basic models used are quite standard, apart from kerrspec itself.[12] For fitting AGN spectra, we considered absorption by inter-stellar matter (wabs), plus a powerlaw for the primary continuum and kerrspec. For the galactic BHCs it is sufficient to add a multicolor black-body component, for the reasons explained in section 1.4 (diskbb).

[11] http://astro.estec.esa.nl/SA-general/Projects/Integral/integral.html

[12] The XSPEC package and included models are described in detail in http://legacy.gsfc.nasa.gov/docs/xanadu/xspec/u_manual.html

2. In fitting the data from the *ASCA* satellite we used only spectra from the Solid-state Imaging Spectrometer (SIS) instrument. This because of the lower energy resolution of the Gas Imaging Spectrometer (GIS; Inoue 1993). The normalization constant has been fixed to 1 for one of the two SIS instruments, and kept free for the other.

   All the data from this satellite have been taken from the public archive, which is available on-line in a very user-friendly form thanks to Jane Turner and Kirpal Nandra.[13]

3. In the case of *BeppoSAX*, data from the LECS, MECS and PDS instruments (the latter with a fixed normalization factor 0.84 with respect to MECS data) have been used, in the intervals $0.1 \div 4.$, $1.7 \div 10.$ and $15. \div 200.$ keV, respectively. However, MECS data alone are needed to fit in the narrow energy range where the iron line is detected.

4. The iron lines have been usually fitted in the narrow interval $3.5 \div 10$ keV, after a preliminary fit on a larger energy range was made in order to constrain the properties of the continuum (powerlaw index Γ and cutoff energy E_{cut}: powerlaw) using gaussian or diskline models to account for the line. In this way the computational time for the relativistic line fits is restricted as far as possible.

5. Because the emission tends to be concentrated in the central parts of the disc, the inner emitting radius is better constrained by the fit than the outer radius.

The three sources we have been dealing with for this work are two Sy-1 galaxies (MCG–6-30-15 and NGC 3516) and a galactic superluminal (GRS 1915+105).

The two Seyferts have been chosen because their *ASCA* spectra show the best-resolved broad iron lines.

There are more objects of the same kind where such features have been detected (section 1.5), but for the moment none of them can be very useful to test relativistic distortions.[14]

[13] The *Tartarus* database can be found at http://tartarus.gsfc.nasa.gov.

[14] A candidate for such work has been NGC 4151, which is a bright nearby ($z = 0.0033$) Sy-1.5 object, whose inclination has been estimated to be ~ 65 degrees. This is one of the very first Seyferts in whose spectrum an iron Kα feature was detected. Wang, Zhou & Wang (1999) presented an analysis of the iron line profile based on the *ASCA* data obtained in May 1995: the profile is broad and skewed, with a large red wing and a weaker blue one. In the 1995 observation the profile is similar, and much better resolved, than in a previous observation of 1993 (Yaqoob *et al.* 1995). When fitted through a relativistic

We already mentioned (section 1.5) that broad iron line features are much less common in galactic BHCs. However, there are possibilities for future work on some selected sources, for instance the famous Cygnus X-1, discovered in 1971 by *Uhuru*. We discussed some properties of this source in section 1.4.1. Interestingly, a broad iron emission feature has been detected in this BHC already in 1985 by Barr *et al.* using *EXOSAT* data, which gave motivation to some of the first computations of relativistic line distortions (Fabian *et al.* 1989). Its X-ray reflection spectrum shows a smearing of likely relativistic origin (e.g. Done & Życki, 1998; Życki *et al.*, 1997 and 1998).

4.3 MCG–6-30-15

This source is a bright Sy-1 galaxy where a broad and asymmetric iron line has been unambiguously detected for the first time by *ASCA* (Tanaka *et al.* 1995). The line width corresponds to a disc matter velocity of $\sim 10^5$ km s^{-1}.

It also shows a large variability on a variety of timescales. Analyzing the Fourier power spectral density of the variability, Nowak & Chiang (2000) using both *ASCA* and *RXTE* data deduced that the central BH mass is of the order of $10^6 M_\odot$, which is relatively low for an AGN.

Guainazzi *et al.* (1999) analyzed the *BeppoSAX* data and found a broad asymmetric profile, fully consistent with the *ASCA* one, in a four-days observation which took place in the summer 1996. From the *BeppoSAX* data,

(Schwarzschild; Fabian *et al.* 1989) accretion disc line model plus a narrow core line model at 6.4 keV, the data constrain the accretion disc to be nearly face-on ($\sim$ 27 degrees), in good agreement with Yaqoob & Weaver (1997) but contrary to the edge-on geometry inferred from optical and UV observations (Nandra *et al.* 1997a). The extended blue line wing could not be properly fitted if not including other components, for instance considering a narrow core and two disc lines with different inclinations of 58 degrees (directly observed) and 0 degrees (possibly scattered into our line of sight by a Comptonizing medium, such as an electron disc atmosphere), respectively. Another possibility is that the blue wing is related to a Nickel Kα feature, whose rest energy is expected to be at 7.48 keV (cp. Figure 3.3). Alternatively, the ambiguosity can depend on warping of the accretion disc (Hartnoll & Blackman 2000a).

A Compton reflection component has never been detected and seems not to be required here, either; however, for a different point of view see Zdziarski *et al.* (1996) who suggest that the continuum is complex and makes the line itself difficult to model.

Moreover, while some authors claim that the line profile is variable (Wang *et al.* 1999b), others stress that there is no evidence of changes in the line intensity (the line EW thus anticorrelates with the continuum flux) and suggest an origin in a region larger than the AD (Weaver *et al.* 2000).

This short summary on NGC 4151's iron line makes already clear that the interpretation of the feature is complex for this source, thus deserving a separate, more careful treatment in a future work.

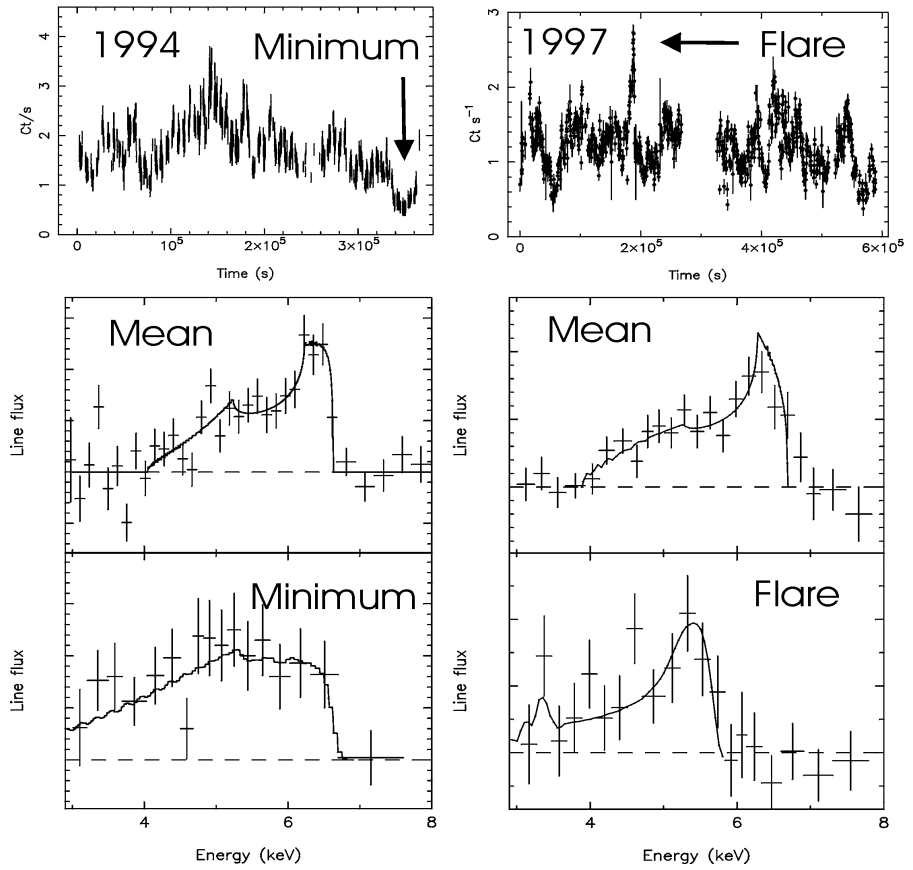

Figure 4.1: The top panels show the light curves of MCG-6-30-15 from the long ASCA observations in 1994 and 1997 (Iwasawa *et al.* 1996b, 1999). The integrated line profiles of both observations are very similar (middle panels). In both observations, however, the line profile was found to vary. In the earlier data, a very broad and redshifted profile was observed during a deep minimum in the flux. In 1997, a similarly extreme profile was observed, but this time during a flare. The profile variations may be attributed to changes in the illumination pattern of the disk due to localized flares. From: Nandra (2000).

the Schwarzschild BH is preferred to the Kerr's one, and $i \sim 30$ degrees. The line EW this time was $\sim$ 200 eV; the amount of reflected continuum could be more carefully evaluated thanks to the satellite's unprecedented broad bandwidth.

Variability

The 2–10 keV flux varies by about 40% between the five *ASCA* pointings of MCG–6-30-15 (e.g. Weaver *et al.*, 2000). During these observations, it is well-documented that the broad line profile varies. Iwasawa *et al.* (1996b) registered rapid variations of the iron line profile and intensity on a timescale of thousands of seconds. In a phase of deep minimum of the total flux the line shape was best fitted by a Kerr profile (Laor 1991) with the inner emitting radius $r_{\rm min}$ equal to the last stable orbit for a maximally rotating black hole. The equivalent width was particularly high, $\sim$1 keV. This value is about a factor three higher than that obtained with the time–averaged data which, when fitted with a Kerr profile using the model by Laor (1991), gives a best fit value for $r_{\rm min}$ of about 9 (Tanaka et al. 1995).

Again, during the 1997 observation another peculiar line shape has been seen, lasting about one hour, which would also require a large red-shifting of the line photons. The blue wing of the line was this time shifted well below 6 keV, while no significant line emission was detected around the rest line energy. A possible explanation is that the line production occurred either in a thin annulus at $4r_m$ or in a small patch at $\sim 2.5r_m$ on the approaching side of the disc (Iwasawa *et al.* 1999).

However, these results have been recently questioned on the base of *RXTE* observations by Lee *et al.* (2000), Reynolds (2000) and by Chiang *et al.* (2000): the line flux seems now to stay constant over timescales of $0.5 \div 500$ ks, while the underlying continuum displays large flux and spectral variations. However, a separate investigation of the broad red wing and narrow core of the line in the 1994 observation (Iwasawa *et al.* 1996a,b) has revealed that, actually, the latter remains constant on short timescales but follows the continuum variations for $\Delta t > 10^4$ seconds, while the red wing follows the continuum on the shorter time scales. This is consistent with a line produced from a relativistic disc (see also: Blackman 1999).

Reverberation in this source has been studied by Reynolds (2000), but in the *ASCA* data there are not enough photons to allow for a detailed time-resolved analysis, while *RXTE* does not have enough energy resolution (see also: Weaver *et al.*, 2000; Lee *et al.*, 2000).

An increase of the line EW occured during the phase of minimum flux singled out by Iwasawa *et al.* (1996b). This may have interesting GR implications: in the model by Martocchia & Matt (1996) the EW increases strongly with decreasing $r_{\rm min}$. An apparent change of $r_{\rm min}$ could actually reflect a change of h. If the black hole is rotating, a strong and even dramatic increase in the line flux is expected owing to light deflection and gravitational and kinematic blueshifts. These effects are instead small for static BHs, because in this case the radius of the accretion disc innermost stable orbit is much greater, i.e. $r_{\rm ms} = 6$ instead of 1.23. It would thus be not surprising if in Kerr metric the EW enhancement is stronger in a phase of minimum flux. However, no line enhancement is predicted by our model with the best-fit value of the inner emitting radius at $\sim 9m$ (Tanaka *et al.* 1995), in which case alternative explanations (e.g. iron abundance greater than solar) would be needed. Indirect checks of our explanation for the large EW observed in this source are also possible. As the primary X–ray continuum is expected to be significantly redshifted if the emitting region is very close to the black hole, a X–ray luminosity lower than usual is expected. Moreover, in our model large EW should be accompanied by large amounts of reflection continuum, which is instead reduced by iron overabundance (George & Fabian 1991; Reynolds *et al.* 1995). However, some new results on this issue, based on *RXTE* data (Lee *et al.* 2000), tend to falsify our model because an anti-correlation between the reflected flux fraction and the iron line EW seems to be at play. It is possible that continuum-flux correlated changes of the ionization of the accretion disc surface do intervene as a complicating factor (e.g. Reynolds 2000).

Finally, it must be stressed that any firm conclusion on the precise value of $r_{\rm min}$ can be derived only by comparing the data with theoretical profiles computed using the proper line emissivity, and subtracting a reflection continuum with the correct intensity and shape - which are also modified by relativistic effects.

Alternative Pictures

As discussed by Fabian *et al.* (2000), alternative models are hardly viable for explaining the broad asymmetric profile of the iron fluorescent line in this source. However, for the sake of completeness we just mention here some non-standard ideas which were formulated about this source.

Misra & Kembhavi (1998) and Misra & Sutaria (1999) put the iron line of MCG–6-30-15 in connection with a highly ionized cloud with radius 10^{14} centimeters – i.e. about 300 Schwarzschild radii – and temperature ~ 0.21

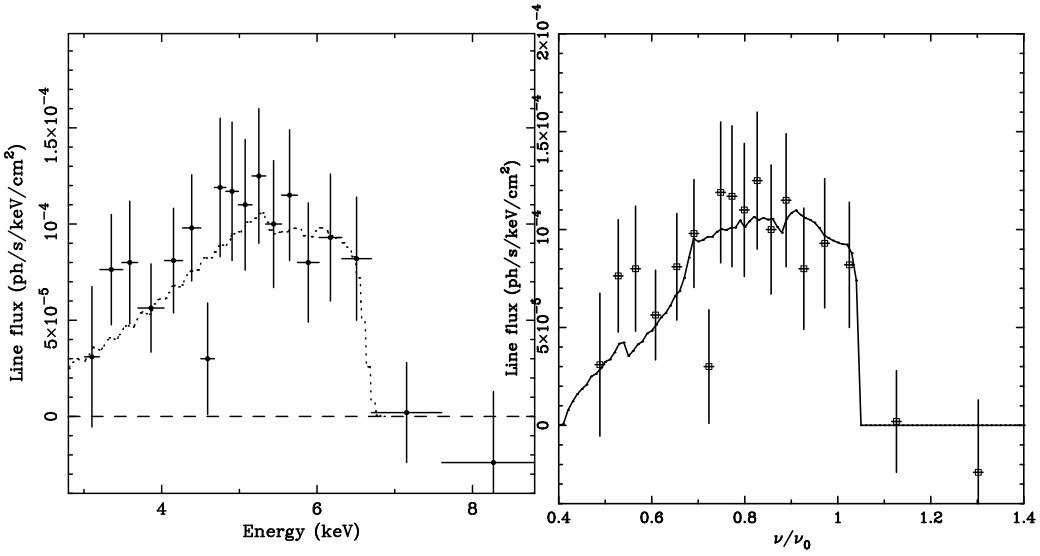

Figure 4.2: The broad and highly redshifted line profile observed in MCG–6-30-15 during a deep minimum of its light curve. The left panel shows the line profile from a maximally spinning Kerr black hole (dotted line), the right panel shows the line profile from a static Schwarzschild black hole using the model of Reynolds & Begelman (1997). From Fabian *et al.* (2000).

keV, where Compton downscattering could occur. The authors in fact state that both effects (the relativistic and the Compton distortions) may concur in this case. As explained in section 1.4.3, Comptonization cannot produce the double peak, which itself implies emission from regions very close to the central BH.

Moreover, Reynolds & Wilms (1999) stressed that the constrains on the cloud size result to be so tight that the optical/UV component would violate the black body limit. Ruszkowski *et al.* (2000) also conclude that, on the base of fits to *ASCA* data, Comptonization as the principal mechanism to explain the shape of the iron line is ruled out for this source.[15]

Two-components models have also been proposed to explain the line profile origin (Sulentic *et al.* 1998a,c; Misra 2000). This alternative pictures could in particular explain the line profile variability reported by Iwasawa *et al.* (1996b): the broad redshifted wing, which remained quite constant, may be originated very near to the BH, while the narrower "blue" component, which strongly responded to continuum changes, can be easily fitted by a

[15]For further discussion on Comptonization models and comparisons to MCG–6-30-15 cp. section ref:alte).

narrow Gaussian (Sulentic *et al.* 1998a).

Weaver & Yaqoob (1998) and McKernan & Yaqoob (1998) considered the deep minimum line profile and EW and suggested that they could be explained by *occultation* of the continuum source and the putative line-emitting accretion disc, without changes in the intrinsic flux.

It must be stressed, however, that only higher time and energy resolution observations of the iron line would be able to differentiate between the various scenarios.

Fitting with kerrspec

Here we present our own fits both to *ASCA* and *BeppoSAX* data of MCG–6-30-15.

We have considered the *ASCA* observation which started on July 23rd, 1994, and lasted for 362895 s, i.e. the same used by Tanaka *et al.* (1995).[16] Assuming $a = 0.9981m$ and $cos(i) = 0.87$, we tried fitting for three different values of the inner disc radius r_1, keeping the pre-calculated best-fit continuum parameters fixed:

absorber's (wabs) column density $n_H = 2.043 \times 10^{22}$ cm^{-2};

powerlaw index $\Gamma = 1.958$.

The fit results to be the best for an intermediate primary source height ($h = 20m$). In this case, we get the values which are shown in table 4.1, and $\chi^2_{\rm red} \sim 1.03$ - while, for instance, the best fit for $h = 6m$ gives $\chi^2_{\rm red} \simeq 1.6$. We also tried including the reflection component in the local spectrum, but the χ^2 was substantially worsened ($\chi^2 \gtrsim 2.3$) due to the bad constrain of the continuum parameters in this case; a better modeling will require further long-lasting computations, to be performed in the future.

We find that the Schwarzschild assumption is slightly favoured, as expected (see table), even if the difference with the Kerr assumption is really tiny.

With our best-fit model, the line EW results to be ~ 210 eV.

We also tried to fit the spectrum of the source corresponding to the 1994 deep minimum, as already analyzed by Iwasawa *et al.* (1996b). The selected data were kindly provided by Kazushi Iwasawa. The results are shown in table 4.2. The values of χ^2 indicate that, this time, a Kerr model is favoured with respect to a Schwarzschild (or: Schwarzschild-equivalent, i.e. just fixing

[16] http://tartarus.gsfc.nasa.gov/html/72013000/72013000.html

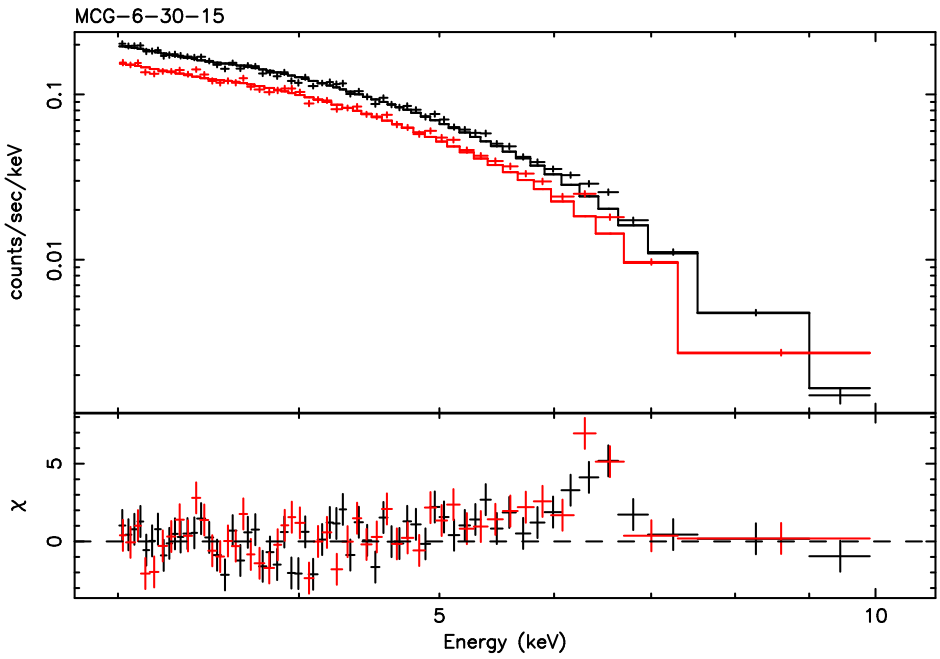

Figure 4.3: The line profile observed in MCG–6-30-15 by *ASCA* in July 1994. The best-fit model (cp. table 4.1) is also shown after putting to zero the normalization of the iron line for illustration purposes.

Table 4.1: A summary of the results obtained with kerrspec for MCG–6-30-15 using the *ASCA* data of the July 1994 observation. The model used here is: model = wabs(powerlaw + kerrspec), the primary source height $h/m = 20$. See the text for more details.

r_1/m	r_2/m	χ^2	dof	$\chi^2_{\rm red}$
1.23 frozen	$104.6^{+60.3}_{-27.2}$	590.4	571	1.034
6 frozen	$99.9^{+59.0}_{-45.5}$	589.3	571	1.025
$7.2^{+27.0}_{-5.9}$	$204.9^{+62.2}_{-105.5}$	589.3	570	1.034

Table 4.2: Results for the *ASCA* low-state spectrum of MCG–6-30-15.

$r_1 \equiv 6m$ $\chi^2_{\rm red} = \frac{181.81}{171} = 1.06$ EW = 678. eV		
Component	Parameter	Value
powerlaw	Γ	1.696 ± 0.095
powerlaw	norm	$(4.680 \pm 0.823)E-03$
kerrspec	a/m	0.9981 frozen
kerrspec	$cos(i)$	0.8700 frozen
kerrspec	h/m	10.00 frozen
kerrspec	r_1/m	6.000 frozen
kerrspec	r_2/m	$13.06^{+7.54}_{-11.83}$
kerrspec	dr	1.000 frozen
kerrspec	$dpsi$	1.000 frozen
kerrspec	norm	$(7.284 \pm 5.300)E-03$

$r_1 \equiv 1.23m$ $\chi^2_{\rm red} = \frac{177.47}{171} = 1.04$ EW = 949. eV		
Component	Parameter	Value
powerlaw	Γ	1.707 ± 0.100
powerlaw	norm	$(4.592 \pm 0.891)E-03$
kerrspec	a/m	0.9981 frozen
kerrspec	$cos(i)$	0.8700 frozen
kerrspec	h/m	10.00 frozen
kerrspec	r_1/m	1.230 frozen
kerrspec	r_2/m	$13.14^{+9.01}_{-11.32}$
kerrspec	dr	1.000 frozen
kerrspec	$dpsi$	1.000 frozen
kerrspec	norm	$(6.422 \pm 2.450)E-03$

r_1, r_2 free $\chi^2_{\rm red} = \frac{177.47}{170} = 1.04$ EW = 914. eV		
Component	Parameter	Value
powerlaw	Γ	1.707 ± 0.100
powerlaw	norm	$(4.61 \pm 0.89)E-03$
kerrspec	a/m	0.9981 frozen
kerrspec	$cos(i)$	0.8700 frozen
kerrspec	h/m	10.00 frozen
kerrspec	r_1/m	$2.44^{+6.08}_{-1.21}$
kerrspec	r_2/m	$13.80^{+9.29}_{-4.01}$
kerrspec	dr	1.000 frozen
kerrspec	$dpsi$	1.000 frozen
kerrspec	norm	$(0.606 \pm 0.460)E-02$

Table 4.3: Results of the fits performed on *BeppoSAX* data for the source MCG–6-30-15. The model used here is wabs × zedge(powerlaw + kerrspec), where the local line emission is given by a Dirac's delta function (**column I**). The best-fit results by Guainazzi *et al.* (1999) are showed in **column II**, even if a comparison should take into account that the underlying reflected component has not been included in our case.

Component	Parameter	I	II
wabs	n_H $[10^{22}]$	0.740 ± 0.258	0.068 ± 0.003
zedge	E_{edge} [keV]	7.6^{fr}	7.6^{fr}
zedge	τ_{max}	0.138 ± 0.027	$0.14^{+0.03}_{-0.05}$
zedge	z	0.008^{fr}	0.008^{fr}
powerlaw	Γ	2.06^{fr}	2.06^{fr}
powerlaw	norm $[10^{-2}]$	2.257 ± 0.038	–
kerrspec	a/m	0.9981^{fr}	0.0000^{fr}
kerrspec	$cos(i)$	0.87^{fr}	0.87^{fr}
kerrspec	h/m	$20.^{fr}$	$(\epsilon \propto r^{-2})$
kerrspec	r_1/m	$7.9^{+13.3}_{-6.7}$	$7.2^{+2.6}_{-1.1}$
kerrspec	r_2/m	$100.7^{+30.3}_{-16.1}$	$1000.^{fr}$
kerrspec	dr	$1.^{fr}$	–
kerrspec	$dpsi$	$1.^{fr}$	–
kerrspec	norm $[10^{-3}]$	1.683 ± 0.607	–
	$EW_{K\alpha}$ [eV]	176.	200.
	χ^2_{red}	$\frac{51.3}{40} \simeq 1.28$	$\frac{138.0}{124} \simeq 1.11$

(^{fr}) frozen

$r_1 = 6m$) one, either through fixing $r_1 \equiv r_{ms}$ or keeping r_1 free (then the best-fit value for r_1 is 2.44; in both cases $\chi^2_{red} \simeq 1.04$).

This time, the primary source had to be "lowered" ($h/m = 10$) in order to improve the fit: apparently, in this state the illuminating field is more concentrated in the inner region. We also tried introducing the Compton-reflected continuum in the local spectrum, still getting a good fit ($\chi^2_{red} \simeq 1.11$), but this result needs to be checked more carefully because the parameter space (e.g. h) was not completely covered.

Also *BeppoSAX* data were fitted with kerrspec. Like in Guainazzi *et al.* (1999), the warm absorber has been parametrized as a set of four absorption edges for OVII, OVIII, NeIX and NeX (Orr *et al.* 1997); more components were added in order to improve the best-fit χ^2 value: narrow emission lines at 0.62 and 0.86 keV, and an absorption edge at 7.6 keV. We found $n_H = 0.74 \times 10^{22}$ cm^{-2}, and a photon index $\Gamma = 2.06$.

When fitting only in the narrow interval where the iron emission is present (from 3.5 to 10. keV) the XSPEC model reduces to:

$$\text{model} = \text{wabs} \times \text{zedge}(\text{powerlaw} + \text{kerrspec}).$$

While a relatively large innermost orbit radius ($r_1 \sim 8m$) seems to be preferred again in the fit, the resulting χ^2 ($\chi^2_{red} = 1.28$) is slightly larger than

the Guainazzi *et al.*'s value (table 4.3), because the Compton-reflected component has not been included in the local spectrum.

In the next future it will be possible to use *XMM-Newton* data of MCG–6-30-15, where a broad iron line is clearly visible even in a quite preliminary data outlook (Molendi *et al.* 2000).

4.4 NGC 3516

Nandra *et al.* (1999) presented an analysis of the broad Kα line in the Seyfert 1 galaxy NGC 3516, on the base of a five-day observation with the *ASCA* satellite which started on April 12, 1998. These data, which have an unprecedented signal-to-noise ratio, clearly show a broad redshifted profile which resembles the well-known one in MCG–6-30-15.

The best fit assuming Schwarzschild metric (Fabian *et al.* 1989) was obtained with an inner radius $r = r_{ms} = 6m$, an inclination $i = 35^o$ (lower in the Kerr assumption) and an extremely steep emissivity, with index $q = 8$, which indicates that the line emission is very much concentrated in the innermost region; when adopting a Kerr metric (diskline model, Laor 1991) the fit is still good but not as in the Schwarzschild case, therefore the fits did not allow to really constrain the BH spin.

The fit is better when an absorption feature in the red line tail is included, which could be due to infalling material, being accreted by the central BH (Nandra *et al.* 1999) or to resonant absorption in a diffuse plasma above the accretion disc (Ruszkowski & Fabian 2000).

The profile variability in NGC 3516 does not have a simple behavior. While the continuum changes by a factor ~ 50 % during the whole observation, when the data are divided into 8 time intervals the line wings appear to be correlated to each other but their fluxes seem *not* to be correlated with the continuum variations; on the contrary, the line core seems to accompany the continuum variations as if it were originated somewhere else in the system. Therefore a process different from reverberation, such as some local flare or obscuration, seems to be at work (see also: Weaver *et al.*, 2000).

Kazanas & Nayakshin (2000) tried to simulate the reflection response from the disc to variations of the central source flux (lamp-post model), considering also the iron line profile, but the results seem to be inconsistent with the observations.

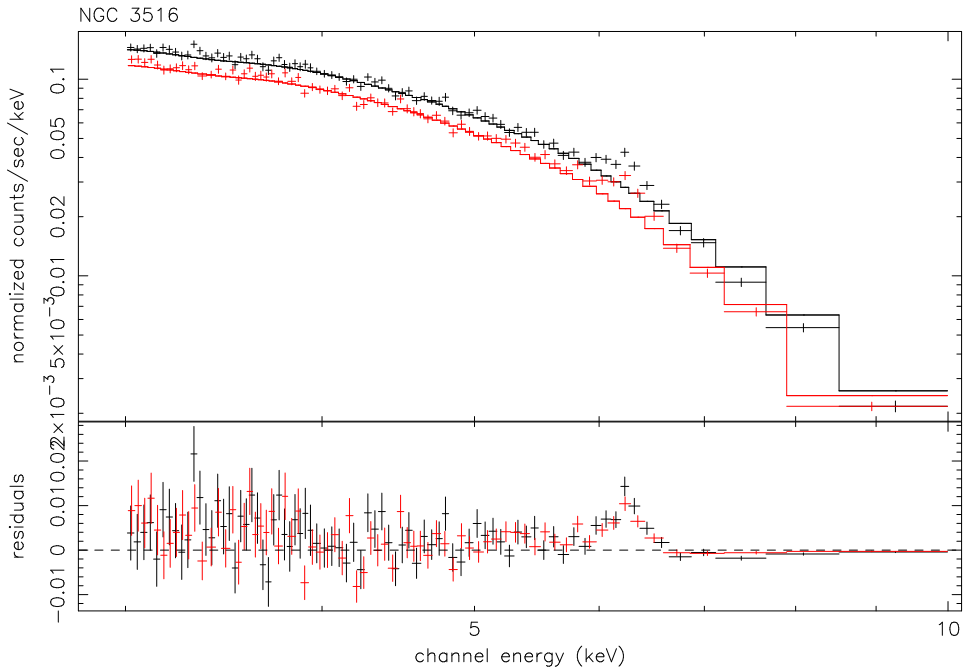

Figure 4.4: The line profile observed in NGC 3516 by *ASCA*, as it comes out from the residuals of our best-fit model, when putting the line normalization to zero for illustration purposes.

Fitting with kerrspec

We used the same dataset of Nandra *et al.* (1999)[17] and started constraining the continuum to the broad-band best-fit values: $n_H = 0.2039 \times 10^{22}$ cm^{-2}, $\Gamma = 1.312$.

Then we tried fitting with a simple powerlaw + kerrspec model. A good fit ($\chi^2_{\rm red} = 1.15$) is obtained using an intermediate primary source height ($h = 20m$) for a Schwarzschild-like assumption on the innermost radius ($r_1 \equiv 6m$), but the resulting outer radius is then quite low ($r_2 \simeq 10.9m$) which does indeed indicate that the emissivity is concentrated at the lowest disc radii, as found by Nandra *et al.* (1999). The resulting spectrum is shown in Figure 4.4; the iron line EW is ~ 240 eV.

When adding an absorption feature at 5.89 keV (Nandra *et al.* 1999) in the form of a Gaussian function with negative normalization, the χ^2 does not improve while the other fit parameters have negligible variations.

We also tried with different values of r_1:

[17] http://tartarus.gsfc.nasa.gov/html/76028000/76028000.html

Table 4.4: Results of the fits performed on *ASCA* data for the source NGC 3516. The model used here is model = wabs(powerlaw + kerrspec + zgauss). We got: $\chi^2_{\rm red} \simeq \frac{764.45}{716 dof} = 1.07$.

Component	Parameter	Unit	Value
wabs	n_H	10^{22}	0.204 ± 0.078
powerlaw	Γ		1.312 ± 0.090
powerlaw	norm		$(0.633 \pm 0.007)E-02$
kerrspec	a/m		0.9981 frozen
kerrspec	$cos(i)$		0.8700 frozen
kerrspec	h/m		20.00 frozen
kerrspec	r_1/m		$5.5^{+12.3}_{-4.2}$
kerrspec	r_2/m		$7.6^{+15.0}_{-6.3}$
kerrspec	dr		1.000 frozen
kerrspec	$dpsi$		1.000 frozen
kerrspec	norm		(0.028 ± 0.001)
zgauss	E_c		6.40000 frozen
zgauss	z		0.0E+00 frozen
zgauss	σ		$(0.883 \pm 0.106)E-02$
zgauss	norm		$(0.633 \pm 0.068)E-04$

- for $r_1 \equiv 1.23m$ (maximal Kerr assumption) we get: $r_2 = 17.0m$ and $\chi^2_{\rm red} \simeq 1.16$;

- for the same r_1 and h "lowered" to $10m$ we have: $r_2 = 9.7m$ and $\chi^2_{\rm red} \simeq 1.26$.

In the residuals we also noticed that a narrow feature remains around 6.4 keV; we thus tried inserting a gaussian line function in the model. The result is shown in table 4.4. Even if the χ^2 improves ($\chi^2_{\rm red} \simeq 1.07$), the residual feature is not completely accounted for.

Clearly, from these results we still cannot really infer whether the one or the other BH model (spinning or static) is favoured by the data.

However, the interesting point here is in the values we got for the disc radii. In our very best fit values (table 4.4), as well as in all other computations we made, the best-fit radii are quite close to each other, which does not seem very physical (e.g. $r_1 = 5.5m$ and $r_2 = 7.6m$). But this may indicate that the emissivity law is really steep, as already found by Nandra *et al.* (1999), and thus that the primary flux is very anisotropic (even if the fit does not improve when varying h) and concentrated in the innermost part of the accretion disc.

4.5 GRS 1915+105

GRS 1915+105 is a galactic superluminal jet source, well-known as an amazing object in the X-ray sky since its discovery by the WATCH experiment on GRANAT in 1992 (Castro-Tirado *et al.* 1992). This source has no optical counterpart because of the very large interstellar absorption, but weak variable radio/IR emission connected with jets (Mirabel & Rodriguez 1994). Measurements of the jets superluminal motions allowed to estimate the source's distance ~ 10 kpc and inclination ~ 70 degrees.

GRS 1915+105 is believed to host a BH because it shows properties very similar to those of the other famous "microquasar", GRO J1655-40, for which precise dynamical measurements yielded $M \sim 7M_{\odot}$, well above the standard neutron star mass limit.

GRS 1915+105 shows an extremely wide variety of variability modes, ranging over all possible bands and timescales (e.g. Markwardt *et al.* 1999, Belloni *et al.* 1997a,b; Greiner *et al.* 1996).

QPOs have also been observed in this source, in a wide range of frequencies ($0.001 \div 67$ Hz, e.g. Morgan *et al.* 1997). In particular, in some observations a QPO with variable centroid frequency, from 0.5 to 10 Hz, is detected, whose value and root mean square amplitude correlate with the thermal flux. Power density spectra show QPOs whose frequency increases with increasing count rate and varies in the range 0.6-8 Hz (Reig *et al.* 2000, Markwardt *et al.* 1999).

The highest frequency, unlike all the others, does not change with time, suggesting that it may be related to the accretion disc innermost stable orbit (Morgan *et al.* 1997). This is consistent with the fact that the QPO is a transient phenomenon, which is present only at certain spectral states: those states in which the disc extends all the way down to the (Kerr) innermost stable orbit.

Time-resolved observations have been intensively performed especially with the Rossi X-ray Timing Explorer (RXTE) satellite mission. Belloni *et al.* (2000), for instance, refer to 163 observations made in the period 1996-1997. They managed to classify these observations into 12 separate classes based on count rate and color characteristics. In this way, the source's variability could be explained in terms of transitions between three basic states: a hard state corresponding to the non-observability of the innermost parts of the accretion disc (state "C"), and two softer states with a fully observable disc at two different temperatures ("A" with the lower temperature, "B" with the higher). Such transitions are very fast, nevertheless they seem to

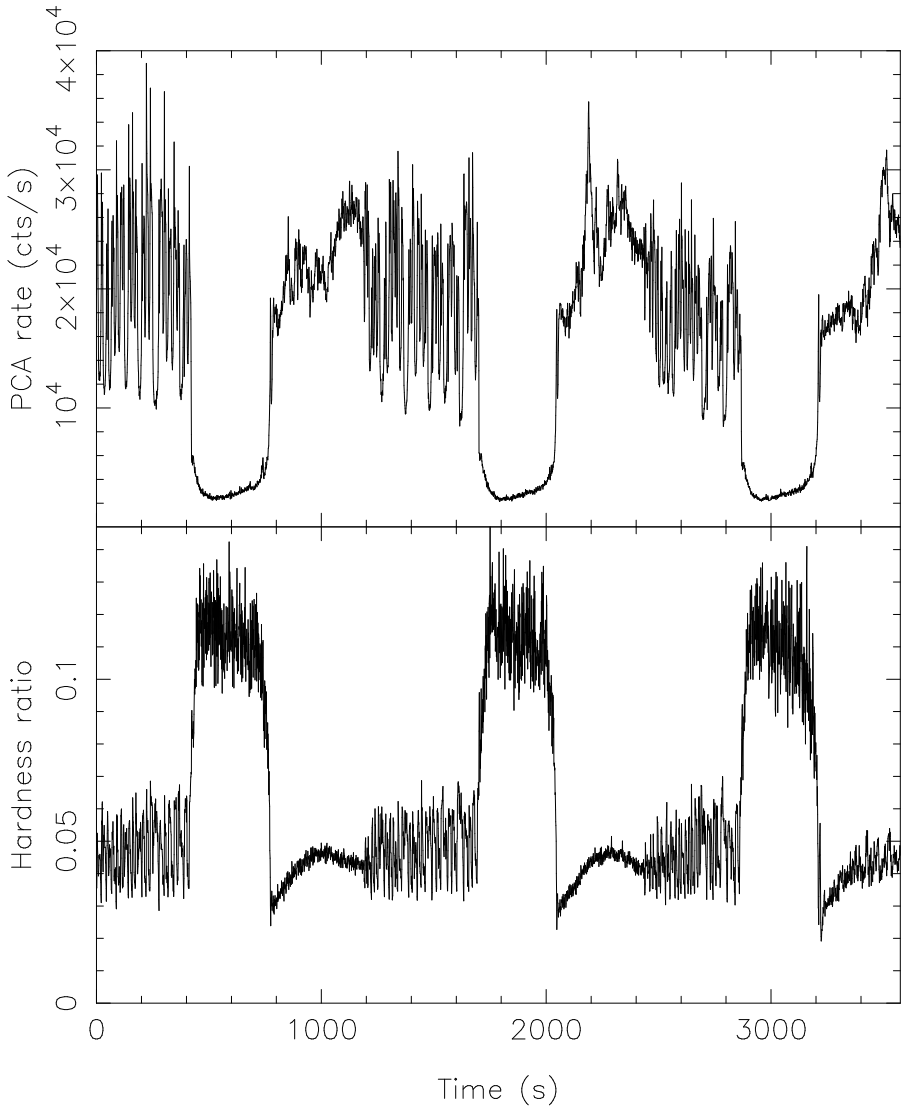

Figure 4.5: In this picture, taken from Belloni *et al.* (1997a), a sequence of the A-B-C (outburst-flaring-quiescent) states of GRS 1915+105 is shown. Data have been taken by *RXTE* in the 2.0-13.3 keV band. In the top panel is the light curve, in the bottom panel the hardness ratio 13.3-60 keV / 2.0-13.3 keV. In other observations this sequence was not always such regular.

follow some precise patterns, giving rise to a large, but still limited number of variability classes.

Belloni *et al.* (1997a,b) suggested that the main cause for the large scale variability of GRS 1915+105 is the onset of a Lightman-Eardley thermal-viscous instability which blows-off the innermost, radiation-pressure supported part of the disc. The hard state (C) would then correspond to a steady replenishment, which takes place on a viscous timescale.[18] Belloni *et al.*'s scenario is based on deriving the innermost disc radius from a multi-blackbody spectral model.

Zhang *et al.* (1997) and Cui *et al.* (1998), on the base of the source X-ray brightness in the soft state – which is most likely due to thermal emission from the innermost disc region – and QPO behavior, respectively, deduced that the accretion disc extends very much near the event horizon, thus that the BH is a Kerr one. If this is true, then in the hard (C) spectral state the disc – or its emitting region at least – does not reach the innermost stable orbit.

State C (low flux, hard color) is always associated with the 0.5-10. Hz QPO, and can last uninterruptedly for weeks or even months. Phase lags are observed during these "plateau" intervals: sometimes they are positive (i.e. photons in the 5-13 keV band arrive later than those in the 2-5 keV band), sometimes negative (soft photons are delayed). The sign of the lags is correlated with the QPO frequency, the count rate and the X-ray colors. When the lag is positive, the spectrum is hard (low state) and the centroid of the 0.5-10 Hz QPO is below 2 Hz; when the lag is negative, the spectrum softens and the QPO frequency increases (Reig *et al.* 2000).

Nobili *et al.* (2000) recently found that a simple Comptonization model can account for this behavior, successfully reproducing various correlations: color-color, lag-color and lag-QPO frequency. They invoke a stratification of the temperature in the corona – hot in the inner region, warm in the outer region. They assume that the dimension of the corona somehow "follows" the innermost disc radius, i.e. the dimension of the corona decreases (by a factor ~ 20) while the disc innermost part is replenished and the disc inner radius moves inwards; at the same time, the coronal optical depth increases and the temperature decreases.

The decrease of the lag in the continuum and the softening of the spectrum as the disc fills in are then a simple consequence of the increase of the coronal optical depth. When the inner edge of the disc is far out, the spectrum is a powerlaw produced by thermal Comptonization of the soft disc photons.

[18] Further support to this picture is provided by numerical simulations (Szuszkiewicz & Miller 1997, 1998).

As r_1 decreases, downscattering becomes progressively more important with respect to upscattering in the hot corona, the spectrum softens and the phase lag decreases. Eventually, the downscattering dominates and the sign of the lag gets inverted.

The QPO frequency also changes in connection with the variation of the disc innermost radius. Nobili *et al.* found a dependence $r_1 \simeq 13\nu_{\rm QPO}^{-0.43}$, similar to what other authors (e.g. Di Matteo & Psaltis 1999) also found in an independent way.

Many different disc-corona models have been invoked to explain the source emission and timing properties. The most common of them refers to the emptying of the innermost part of the (optically thick) accretion disc, and its subsequent replenishment. This perhaps implies noticeable and fast variations of the inner (emission) disc radius, even if Di Matteo & Psaltis (1999) argue that these variations do not need to be so dramatic. Indeed, evidence of the temporary disappearance and subsequent restoring of the inner portion of the accretion disc comes from comparative analysis of *BeppoSAX* and Ryle radiotelescope data (Feroci *et al.* 1999).

Zhang *et al.* (2000) imagine a three-layered atmospheric structure in the inner region of the accretion disc, consisting of a cold (0.2-0.5 keV) standard disc surrounded by a warm layer (1.0-1.5 keV) and, sometimes, a much hotter ($\sim$ 100 keV) optically thin corona above the latter.

A confirmation that an extremely hot disc, possibly not stable but, still, existing at certain spectral phases, resides in the system would be very important because an unusually high disc temperature may be explained by the BH rotation, which causes the disc to extend closer to the BH, hence to be hotter. If interpreted according to the standard accretion disc prescription of Shakura & Sunyaev (1973), where $T[\mathrm{keV}] \propto (\dot{M}/M)^{1/4}$, the observed temperatures of 2-3 keV would correspond to a mass of the central object of much less than 1 $M_\odot$. Such a low mass, however, seems unacceptable given the high luminosity. Thus, either a different cooling process is active in such an object, or the implicit assumption of a last stable orbit at the Schwarzschild's BH value of $6m$ is wrong. Assuming a mass of 30 $M_\odot$ (based on the lower QPO frequency and luminosity arguments), the presence of an extreme Kerr BH would be deduced.

Table 4.5: Flux and duration of the six spectral phases sorted out from the *BeppoSAX* observation of GRS 1915+105 which took place on April 19th, 1998. The flux is calculated for the best-fit model in the energy interval from 3.5 to 8.0 keV.

	Flux:	[photons cm^{-2} s^{-1}]	[ergs cm^{-2} s^{-1}]	Count rate [cts/s]	Δt [s]
QS1	*maxim.*	2.084	1.627E-08	124	2562
QS2		1.963	1.541E-08	117	1993
QS3		2.026	1.592E-08	119	2551
QS4		1.990	1.575E-08	119	2003
QS5	*minim.*	1.889	1.489E-08	113	1628
QS6		2.072	1.617E-08	124	2708

The Iron Line

GRS 1915+105 shows a strong iron Kα fluorescent emission line in the spectrum observed by *BeppoSAX* on April 19, 1998 (e.g. Figure 4.9).[19] We have fitted the data, and the results are shown in the tables 4.5 – 4.9. Considering the time-averaged profile one obviously cannot get a meaningful fit because of the extreme source's variability. We therefore sorted out a phase of relative calmness in the lightcurve, and further divided this period into six short intervals (figure 4.6).

A summary of the results obtained for each one of the sub-intervals is given in table 4.9.

In this section we present in particular all the results of the fits performed for three of these states, the first with the relative maximum flux (we called it "QS1"), the second showing an intermediate flux ("QS2"), and the third corresponding to the relative minimum flux ("QS5"; see tables 4.6, 4.7 and 4.8 respectively).

[19] An absorption feature had been detected in *ASCA* data (Ebisawa 1996), similar to the one detected in the spectrum of the other superluminal BHC GRO J1655–40 (Ueda *et al.* 1998). Its interpretation seemed difficult because of the complex profile, probably due to absorption by He-like and H-like iron ions in an anisotropic hot plasma perhaps connected to the jets. Alternatively, the absorption-line feature may be a consequence of the large inclination angle of the system.

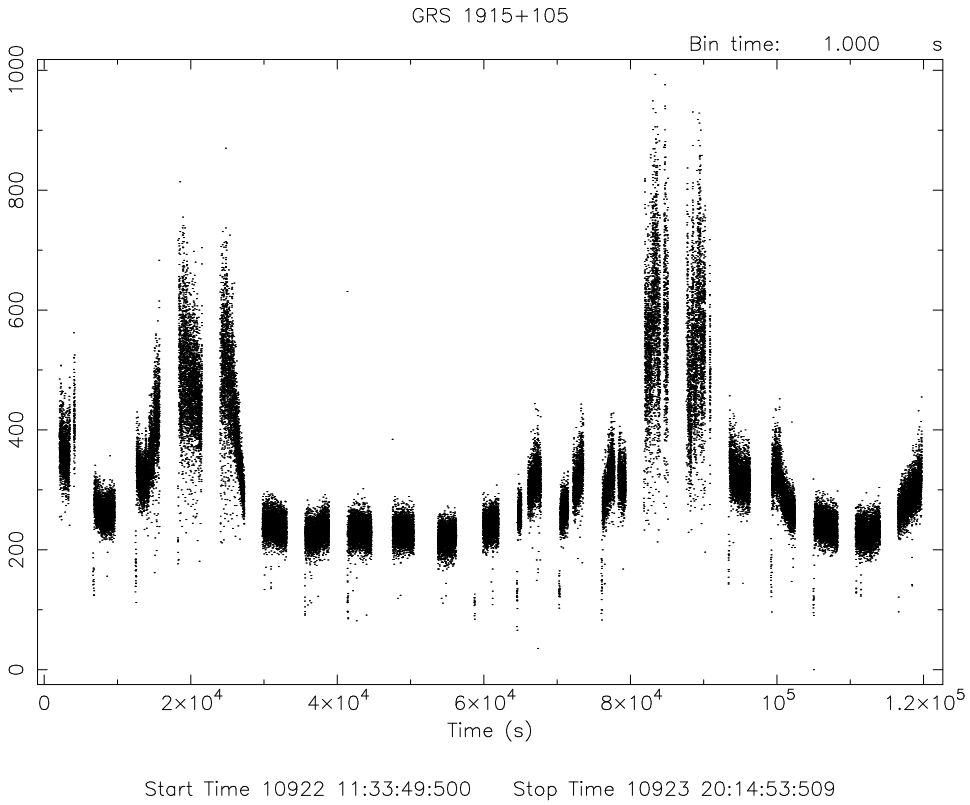

Figure 4.6: The lightcurve of GRS 1915+105 during the April 19, 1998 observation with *BeppoSAX*, which lasted $\sim$ 120 ks. The six spectral phases considered in this paragraph are those comprised between $t \sim 3 \times 10^4$ and$t \sim 6.2 \times 10^4$ s.

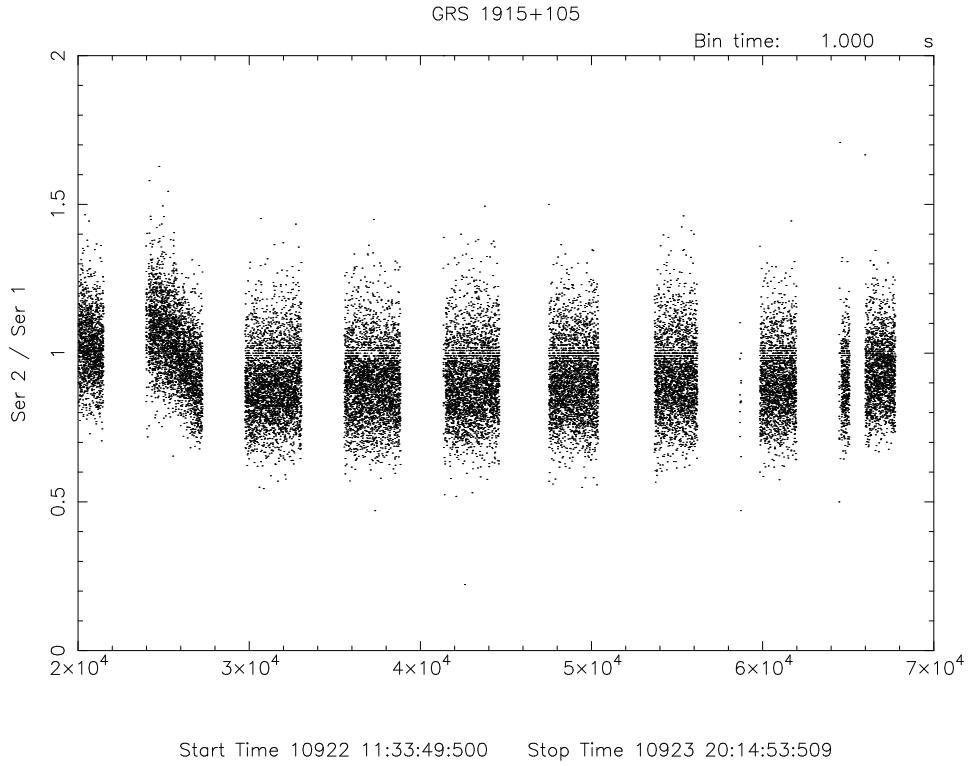

Figure 4.7: The hardness ratio ($\frac{4.\div 10.\ \mathrm{keV}}{1.\div 4.\ \mathrm{keV}}$) variation of the spectrum of GRS 1915+105 in the time intervals used for our computations. The binning used here is of 1 second.

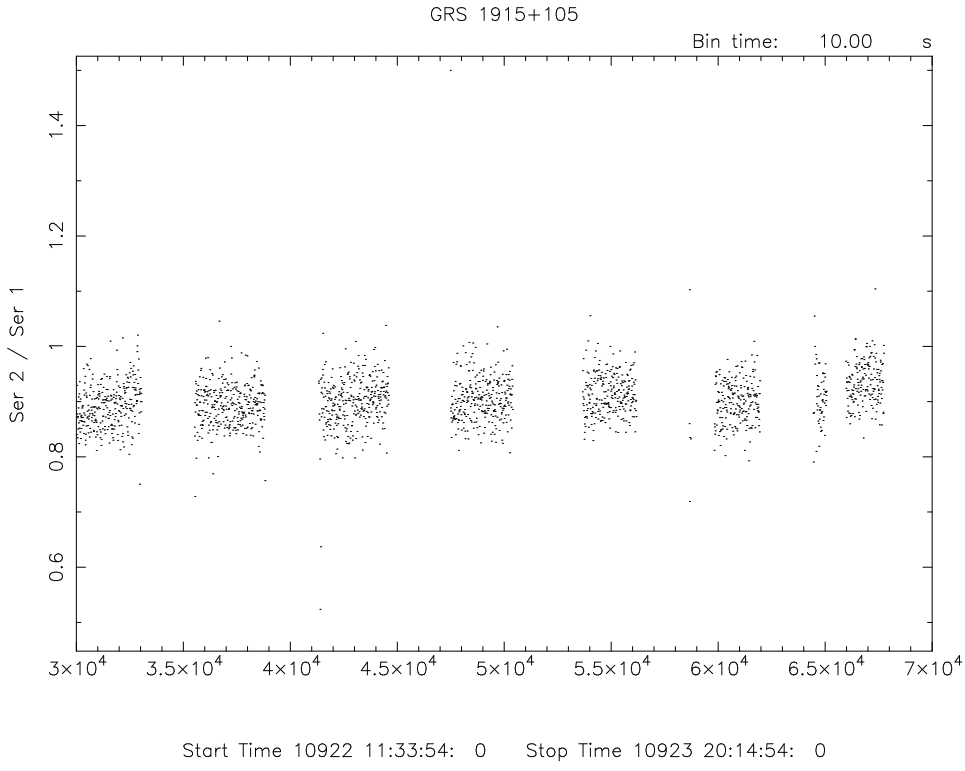

Figure 4.8: Again the hardness ratio variation, but for bins of 10 seconds.

Table 4.6: Results of fitting GRS 1915+105 *BeppoSAX* data in a narrow range around the iron Kα feature with a model: wabs $\times$ diskbb(powerlaw + kerrspec). The first spectral phase of our sample (**QS1**) is considered here, which corresponds to the relative **maximum** flux.

$r_1 \equiv 6.$		$\chi^2_{\rm red} = \frac{43.04}{26} = 1.65$	EW = 260. eV
Component	Parameter	Unit	Value
wabs	n_H	10^{22}	5.900 ± 1.094
diskbb	T	keV	1.857 frozen
diskbb	norm		4.1525E-03
powerlaw	Γ		2.910 frozen
powerlaw	norm		41.50 ± 5.70
kerrspec	a/m		0.9981 frozen
kerrspec	$cos(i)$		0.3500 frozen
kerrspec	h/m		20.00 frozen
kerrspec	r_1/m		6.0 frozen
kerrspec	r_2/m		63.96 ± 12.50
kerrspec	dr		1.000 frozen
kerrspec	$dpsi$		1.000 frozen
kerrspec	norm		1.300 ± 0.230
$r_1 \equiv 1.23$		$\chi^2_{\rm red} = \frac{46.70}{26} = 1.80$	EW = 204. eV
Component	Parameter	Unit	Value
wabs	n_H	10^{22}	5.920 ± 1.112
diskbb	T	keV	1.857 frozen
diskbb	norm		4.7125E-03
powerlaw	Γ		2.910 frozen
powerlaw	norm		47.75 ± 12.02
kerrspec	a/m		0.9981 frozen
kerrspec	$cos(i)$		0.3500 frozen
kerrspec	h/m		20.00 frozen
kerrspec	r_1/m		1.23 frozen
kerrspec	r_2/m		76.33 ± 22.38
kerrspec	dr		1.000 frozen
kerrspec	$dpsi$		1.000 frozen
kerrspec	norm		0.847 ± 0.097
r_1, r_2 free		$\chi^2_{\rm red} = \frac{38.72}{25} = 1.55$	EW = 239. eV
Component	Parameter	Unit	Value
wabs	n_H	10^{22}	5.890 ± 1.351
diskbb	T	keV	1.857 frozen
diskbb	norm		2.8385E-15
powerlaw	Γ		2.910 frozen
powerlaw	norm		47.70 ± 14.68
kerrspec	a/m		0.9981 frozen
kerrspec	$cos(i)$		0.3500 frozen
kerrspec	h/m		20.00 frozen
kerrspec	r_1/m		10.79 ± 2.33
kerrspec	r_2/m		49.43 ± 7.97
kerrspec	dr		1.000 frozen
kerrspec	$dpsi$		1.000 frozen
kerrspec	norm		1.300 ± 0.230

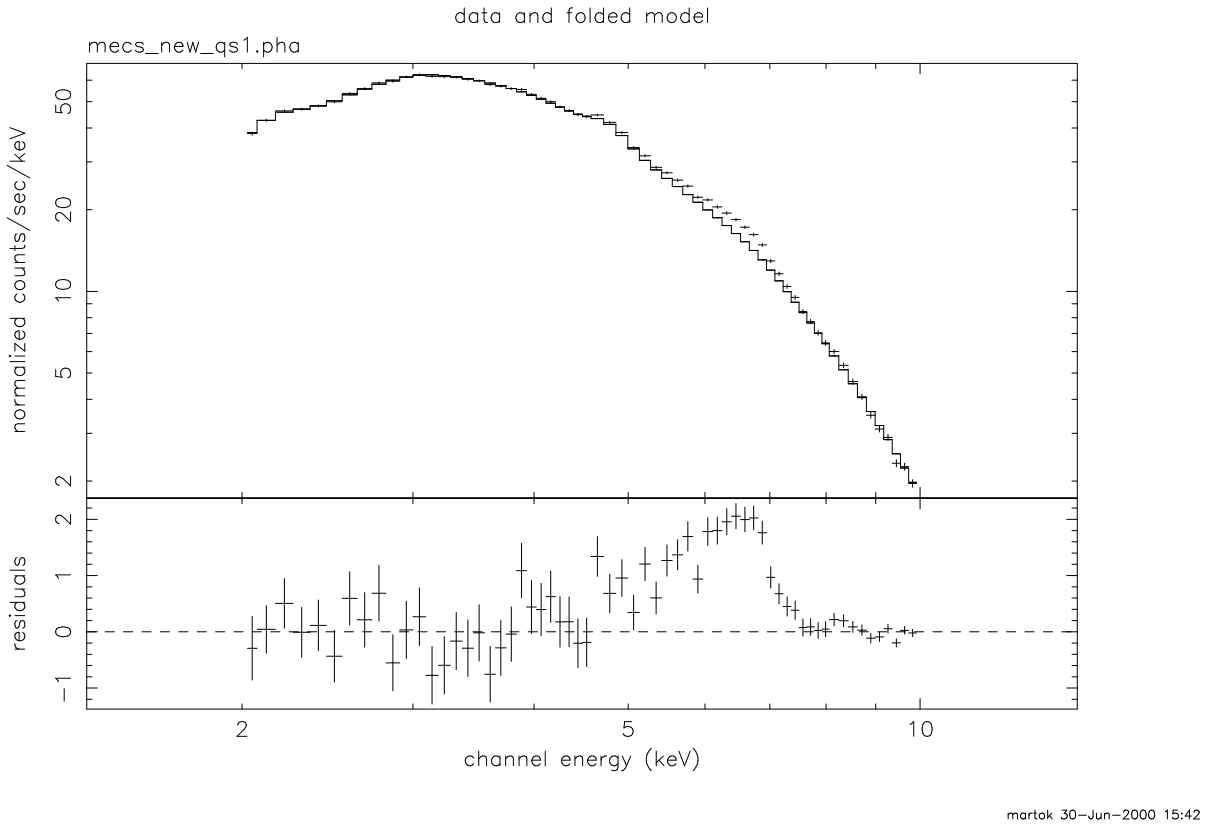

Figure 4.9: The data and best-fit spectrum of GRS 1915+105 with *BeppoSAX* (spectrum QS1).

In the phase QS1, corresponding to the relative maximum flux, the best-fit model ($\frac{38.72}{25\ dof} = 1.55$) indicates an inner radius even larger than the Schwarzschild innermost stable orbit ($r_1 = 10.8$, $r_2 = 49.4$); thus the rapidly rotating BH assumption is not required by the data. The same conclusion holds for the phase of relative minimum flux (QS5, $\chi^2_{\rm red} = 1.28$, $r_1 = 12.5$ and $r_2 = 32.9$) as well as for all other phases. In all six cases, the best fit is for an intermediate emissivity ($h = 20.$).

When we exclude the spectrum QS4, which provided the biggest problems and uncertainties in the fitting (cp. table 4.9), in all the remaining cases we found no need for invoking a rotating BH. For all spectral phases the emitting disc region is the same within the errors, but interestingly the phases of minimum and maximum relative fluxes do also correspond to the minimally (QS5: $r_1 = 12.5$ and $r_2 = 32.9$) and maximally (QS2: $r_1 = 10.8$, $r_2 = 49.4$) extended best-fit emitting disc radii. However, more spectral phases should be analyzed in the future, in order to underline possible correlations which are not easily understandable at this stage, including also the reflection component in the model.

Table 4.7: Like in the previous table, but for the spectral phase **QS2**.

$r_1/m \equiv 6.$		$\chi^2_{\rm red} = \frac{69.18}{41} = 1.69$	EW = 290. eV
Component	Parameter	Unit	Value
wabs	n_H	10^{22}	6.525 ± 1.094
diskbb	T	keV	4.184 frozen
diskbb	norm		0.660 ± 0.052
powerlaw	Γ		3.129 frozen
powerlaw	norm		59.03 ± 1.12
kerrspec	a/m		0.9981 frozen
kerrspec	$cos(i)$		0.3500 frozen
kerrspec	h/m		20.00 frozen
kerrspec	r_1/m		6.0 frozen
kerrspec	r_2/m		$61.93^{+938.07}_{-15.82}$
kerrspec	dr		1.000 frozen
kerrspec	$dpsi$		1.000 frozen
kerrspec	norm		1.112 ± 0.102
$r_1/m \equiv 1.23$		$\chi^2_{\rm red} = \frac{75.7}{41} = 1.85$	EW = 233. eV
Component	Parameter	Unit	Value
wabs	n_H	10^{22}	6.628 ± 0.205
diskbb	T	keV	4.184 frozen
diskbb	norm		0.633 ± 0.052
powerlaw	Γ		3.129 frozen
powerlaw	norm		59.63 ± 1.10
kerrspec	a/m		0.9981 frozen
kerrspec	$cos(i)$		0.3500 frozen
kerrspec	h/m		20.00 frozen
kerrspec	r_1/m		1.23 frozen
kerrspec	r_2/m		$83.49^{+916.51}_{-21.03}$
kerrspec	dr		1.000 frozen
kerrspec	$dpsi$		1.000 frozen
kerrspec	norm		0.913 ± 0.087
r_1, r_2 free		$\chi^2_{\rm red} = \frac{59.32}{40} = 1.48$	EW = 282. eV
Component	Parameter	Unit	Value
wabs	n_H	10^{22}	6.337 ± 0.216
diskbb	T	keV	4.184 frozen
diskbb	norm		0.720 ± 0.053
powerlaw	Γ		3.129 frozen
powerlaw	norm		57.94 ± 1.14
kerrspec	a/m		0.9981 frozen
kerrspec	$cos(i)$		0.3500 frozen
kerrspec	h/m		20.00 frozen
kerrspec	r_1/m		$11.49^{2.30}_{-1.88}$
kerrspec	r_2/m		40.89 ± 5.43
kerrspec	dr		1.000 frozen
kerrspec	$dpsi$		1.000 frozen
kerrspec	norm		1.676 ± 0.289

Table 4.8: The same as before, but for the **minimum** flux spectral phase **QS5**. The fit becomes substantially worse ($\chi^2_{\rm red}$ larger than 2) when fixing $h = 10m$ instead of $20m$, as used here and in the previous tables.

$r_1 \equiv 1.23$		$\chi^2_{\rm red} = \frac{92.24}{58} = 1.59$	EW = 291. eV
Component	Parameter	Unit	Value
wabs	n_H	10^{22}	5.876 ± 0.043
diskbb	T	keV	2.647 frozen
diskbb	norm		10.35 ± 0.28
powerlaw	Γ		3.321 frozen
powerlaw	norm		56.15 ± 0.75
kerrspec	a/m		0.9981 frozen
kerrspec	$cos(i)$		0.3500 frozen
kerrspec	h/m		20.00 frozen
kerrspec	r_1/m		1.230 frozen
kerrspec	r_2/m		48.37 ± 8.41
kerrspec	dr		1.000 frozen
kerrspec	$dpsi$		1.000 frozen
kerrspec	norm		1.011 ± 0.102
$r_1 \equiv 6.0$		$\chi^2_{\rm red} = \frac{85.07}{58} = 1.47$	EW = 281. eV
Component	Parameter	Unit	Value
wabs	n_H	10^{22}	5.869 ± 0.043
diskbb	T	keV	2.647 frozen
diskbb	norm		10.41 ± 0.27
powerlaw	Γ		3.321 frozen
powerlaw	norm		56.02 ± 0.74
kerrspec	a/m		0.9981 frozen
kerrspec	$cos(i)$		0.3500 frozen
kerrspec	h/m		20.00 frozen
kerrspec	r_1/m		6.0 frozen
kerrspec	r_2/m		42.94 ± 5.88
kerrspec	dr		1.000 frozen
kerrspec	$dpsi$		1.000 frozen
kerrspec	norm		1.190 ± 0.125
r_1, r_2 free		$\chi^2_{\rm red} = \frac{72.91}{57} = 1.28$	EW = 269. eV
Component	Parameter	Unit	Value
wabs	n_H	10^{22}	5.850 ± 0.043
diskbb	T	keV	2.647 frozen
diskbb	norm		10.63 ± 0.27
powerlaw	Γ		3.321 frozen
powerlaw	norm		55.59 ± 0.74
kerrspec	a/m		0.9981 frozen
kerrspec	$cos(i)$		0.3500 frozen
kerrspec	h/m		20.00 frozen
kerrspec	r_1/m		12.50 ± 2.22
kerrspec	r_2/m		32.88 ± 5.01
kerrspec	dr		1.000 frozen
kerrspec	$dpsi$		1.000 frozen
kerrspec	norm		1.906 ± 0.521

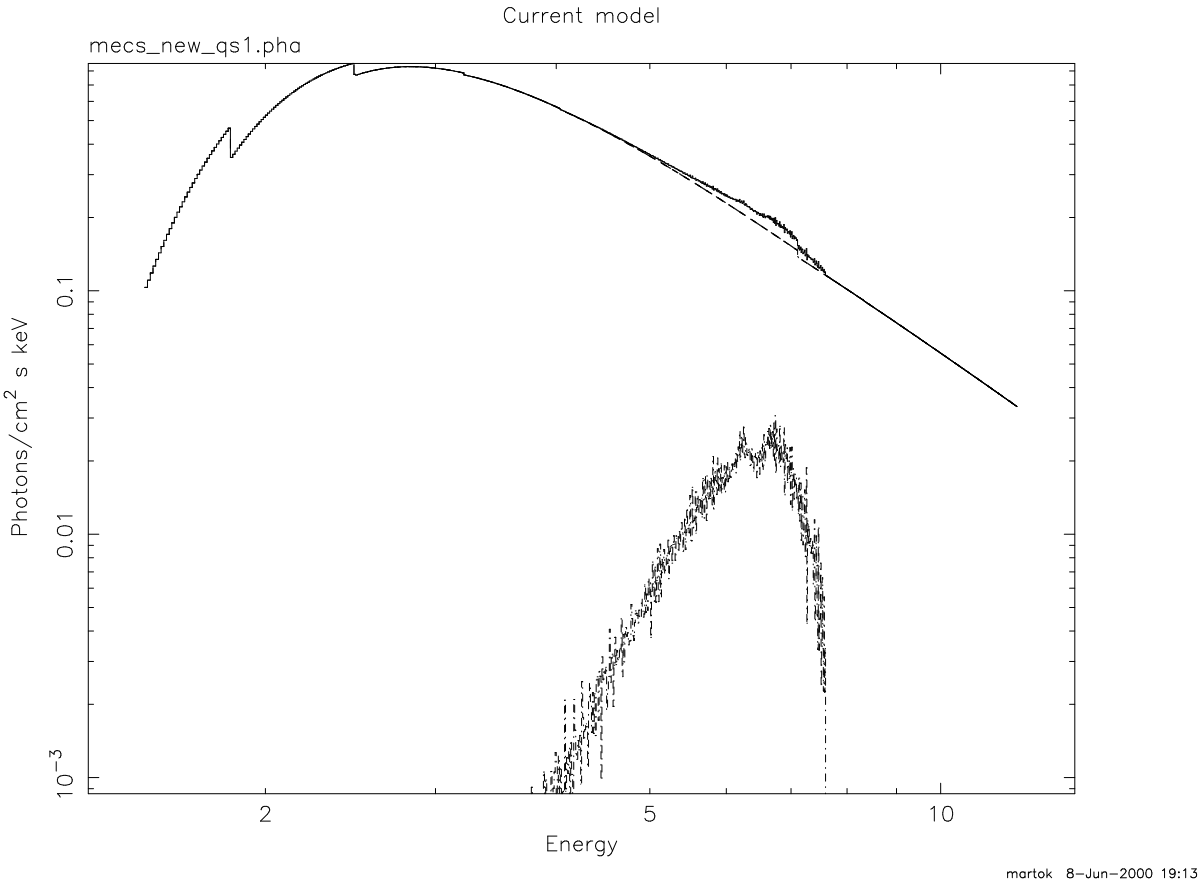

Figure 4.10: An example of the broad iron line in GRS 1915+105 modelled with kerrspec (spectrum QS1).

Table 4.9: Here is a summary of the best-fit results we obtained using the *BeppoSAX* observation of GRS 1915+105 which took place on 04/19/1998 (cfr. table 4.5). While the continuum parameters T and Γ have been previously constrained to allow a faster computation with kerrspec, n_H^{bf}, h^{bf}, $r_{1,2}^{bf}$ are final best-fit values.

	n_H^{bf} [$\times 10^{22}$ cm^{-2}]	T [keV]	Γ	h^{bf}/m	r_1^{bf}/m	r_2^{bf}/m	EW [eV]	$\chi^2_{\rm red}$
QS1	5.89 ± 1.35	1.86 ± 0.46	2.91 ± 0.11	20.	10.8 ± 2.3	49.4 ± 8.0	239.	1.55
QS2	6.34 ± 0.22	4.18 ± 0.08	3.13 ± 0.01	20.	11.5 ± 1.9	40.9 ± 5.4	282.	1.48
QS3	5.39 ± 0.34	4.92 ± 0.27	2.68 ± 0.04	20.	10.8 ± 4.3	36.4 ± 6.6	217.	1.40
QS4	5.68 ± 0.04	4.71 ± 0.07	2.71 ± 0.01	20.	1.230 frozen	372.7 ± 56.7	196.	0.91
QS5	5.85 ± 0.04	2.65 ± 0.21	3.32 ± 0.42	20.	12.5 ± 2.2	32.9 ± 5.0	269.	1.28
QS6	6.02 ± 1.05	$1.94^{+0.48}_{-0.45}$	$2.94^{+0.30}_{-0.14}$	20.	11.1 ± 1.6	35.4 ± 3.7	280.	0.89

Conclusions

Relativistic distortions in the X-ray spectra of BH systems are a fundamental diagnostic to probe the effects of strong gravity. Fully-relativistic calculations may also help to distinguish static from rotating BHs.

To these aims, both the continuum and the iron Kα line emission from accretion discs around rotating black holes are currently being investigated under simplifying assumptions on the geometry of the sources and the physical processes which produce the X-ray features.

In such studies, the disc has been usually considered as a perfectly thin, cold reflector extending on the equatorial plane from r_{ms} to some outer radius, and the disc emissivity law has been parametrized as a simple power-law function of the distance.

However, a self-consistent treatment of the problem must take into account the general-relativistic effects acting also on the primary, illuminating flux, as well as the complex physical conditions (density, ionization, etc.) under which the X-ray reprocessing takes place in the accretion disc.

While the latter issue is very complex and yet subject to preliminary studies (e.g. Done & Nayakshin, 2000), the GR anisotropy of the illuminating flux can be now treated in a satisfactory way (Martocchia & Matt 1996) even if still on the base of simplified toy-models of the geometry of the primary flux emitting region.

Considering GR anisotropy of the illuminating flux is crucial to distinguish static from spinning BHs, because the primary illumination – and thus the subsequent disc emissivity law of the reflection component – carries fundamental information on the spacetime in the very vicinity of the BH. In

particular, it contributes to determine the iron line intensity and EW, together with the line profile (Martocchia & Matt 1996, Martocchia, Karas & Matt 2000).

Another point to consider carefully is that of the underlying continuum component. The observed line profiles are often obtained from the data by subtracting the Compton-reflected continuum component, for which important relativistic effects, such as the iron edge smearing, are usually not taken into account.

Therefore, in our computations (e.g. Martocchia, Karas & Matt, 2000), besides using emissivity laws derived from a proper GR treatment of the illuminating flux, we treated at the same time the GR distortions on the iron line together with those on the underlying continuum.

We could thus present new results for the line integral quantities, which self-consistently take into account the mentioned effects (Martocchia, Karas & Matt, 2000; Martocchia, Matt & Karas, 1999).

The same method can be also used to fit real data. Synthetic spectra of the radiation which is reflected from the BH accretion disc – iron fluorescent line and Compton-reflected continuum hump – have to be compared with the data obtained by X-ray telescopes. We have developed a fitting tool, named kerrspec, which works within the XSPEC package for fitting data in the X-ray band.

In the last chapter of this Dissertation we have showed preliminary results obtained with this tool for some relevant sources: MCG–6-30-15, NGC 3516 and GRS 1915+105. We payed attention to the relativistic distortions on the iron line profiles, while fits performed including the continuum reflected component will be the subject of future work, to allow a complete coverage of the parameters space. These first computations have had two main scopes: first, to test the functioning of the newly developed numerical tool; secondly, to see whether the fast-spinning BH assumption is required by the data or not.

The iron line profile of MCG–6-30-15 has been observed both by *ASCA* (Tanaka *et al.* 1995) and *BeppoSAX* (Guainazzi *et al.* 1999). Apart from confirming the broad, double-peaked asymmetric shape of the line profile, the latter mission could also better constrain the underlying continuum.

Fitting the data from both missions, we find that a Schwarzschild picture may explain the profile's time-averaged shape. The deep minimum profile (Iwasawa *et al.* 1996b), on the contrary, is better fitted using the innermost

orbit for a maximally rotating Kerr BH: light rays originating from below $6m$ are necessary to account for the extremely redshifted radiation.

A broad line profile has been detected in NGC 3516, too. Again, on the base of our computations with kerrspec we can confirm the previous claim (Nandra *et al.* 1999) that no extreme Kerr assumption is required, and that the emissivity law is very steep, which causes the best-fit disc emitting region to restrict to a narrow ring around $r_{eq} \sim 6m$. An additional narrow feature at 6.4 keV further improves the fit.

The most original result is the one we obtained considering the *BeppoSAX* data of the superluminal galactic source GRS 1915+105, which also has a strong iron Kα fluorescent feature in its April 19, 1998, spectrum. We considered various intervals in the observation in which the source variability is less pronounced, and fitted the innermost emitting orbit, again concluding that the maximal Kerr assumption is generally not required by the data.

Of course, our results here are just indicative of the intensity and shape of the fluorescent iron emission, while more significant hints on the physical processes taking place in this object should account for its extreme variability more in detail.

The results are encouraging; however, the theoretical models still suffer from a large number of free parameters, which the observational evidence does not yet permit to constrain tightly enough. Better sensitivity and spectral resolution are needed to confirm typical, double-horn profiles that are expected in disc-type geometry under suitable conditions (e.g. large inclination angle), while temporal resolution will enable real mapping of the sources.

The above-described kerrspec is a useful tool to compute spectra and to use them for fitting the observed features. Various assumptions on the locally emitted radiation can be made and given as inputs for the computations, while different parameters are adjustable with regard to the theoretical model. In the future we also intend to consider non-axisymmetric patterns in the disc emissivity (e.g. spiral waves; Karas, Martocchia & Šubr 2000), geometrically thick and non-Keplerian discs, and other situations which have not been fully explored yet. Apart from introducing a more refined description of the accretion flow and of the X-ray production mechanism, the plan is to explore also multi-component models, in which the gaseous disc resides and radiates in symbiosis with the environment (corona, outflows...).

After the important results provided by the *ASCA* and *BeppoSAX* missions, many more data from the satellite *XMM-Newton*, launched in Decem-

ber 1999, will be available soon. These data have resolution comparable to that of *ASCA*, but a much better throughput. This will allow to get better insight of the known sources, and to broaden the collection of objects to be carefully taken into consideration. By performing extensive computations and fitting to *XMM* data it will be possible to explore a much broader set of parameters and sources.

We thus expect, in the next future, to become able to address the numerous unsettled problems and questions which still remain open, possibly checking the current hypotheses and models.

Bibliography

[1] Abramowicz M.A. *et al.*, 1988, Astroph. J. **332**, 646
[2] Abramowicz M.A. *et al.*, 1995, Astroph. J. **438**, L37
[3] Abramowicz M.A. *et al.*, 1996, Astron. & Astroph. **313**, 334
[4] Abramowicz M.A., Lasota J.P., Igumenshchev I.V., 2000, MNRAS **314**, 775
[5] Abrassart A., 1999, in: Proc. of the 32nd COSPAR Scientific Assembly (Nagoya), Advances in Space Research – in press
[6] Abrassart A. & Dumont A.M., 1998, in: Proc. 1st XMM Workshop *"Science with XMM"*, held in Noordwijk, The Netherlands – http://astro.estec.esa.nl/XMM/news/ws1/ws1_papers.html
[7] Agol E. & Krolik J., Astroph. J. **524**, 49
[8] Antonucci R., 1993, Ann. Rev. Astron. Astroph. **31**, 473
[9] Armitage P.J., Reynolds C.S., Chiang J., 2000, Astroph. J., submitted – astro-ph/0007042
[10] Artemova I.V., Björnsson G., Novikov I.D., 1996, **461**, 565
[11] Ball G., Narayan R., Quataert E., 2000, Astroph. J. Lett., submitted - astro-ph/0007037
[12] Balucinska-Church M. & Church M.J., 2000, MNRAS **312**, L55
[13] Bao G., 1992, Astron. & Astroph. **257**, 594
[14] Bao G., 1993, Astroph. J. **409**, L41
[15] Bao G. & Stuchlik Z., 1992, Astroph. J. **400**, 163
[16] Bao G., Hadrava P., Østgaard E., 1994, Astroph. J. **425**, 63
[17] Bao G., Wiita P.J., Hadrava P., 1998, Astroph. J. **504**, 58
[18] Bardeen J.M., 1970, Astroph. J. **162**, 71
[19] Bardeen J.M. & Patterson J.A., 1975, Astroph. J. **195**, L65
[20] Bardeen J.M., Press W.H., Teukolsky S.A., 1972, Astroph. J. **178**, 347
[21] Barr P., White N.E., Page C.G., 1985, MNRAS **216**, 65
[22] Basko M.M., 1978, Astroph. J. **223**, 268
[23] Beckert T., 2000, Astroph. J., in press – astro-ph/0003323
[24] Belloni T. *et al.*, 1997a, Astroph. J. **479**, L145
[25] Belloni T. *et al.*, 1997b, Astroph. J. **488**, L109
[26] Blackman E.G., 1999, MNRAS **306**, L25
[27] Blandford R.D. & Begelman M.C., 1999, MNRAS **303**, L1
[28] Blandford R.D. & Znajek R.L., 1977, MNRAS **179**, 433

[29] Boella G. *et al.*, 1997, Astron. & Astroph. Suppl. Series **122**, 299

[30] Bondi H. & Hoyle F., 1944, MNRAS **104**, 203

[31] Bromley B.C., Chen K., Miller W.A. 1997, Astroph. J. **475**, 57B

[32] Bromley B.C., Miller W.A., Pariev V.I., 1998, Nature **391**, 54

[33] Byrd P.F. & Friedman M.D., 1974, *Handbook of Elliptic Integrals for Engineers and Physicists*, Springer Verlag, Würzburg

[34] Čadež A., Fanton C., Calvani M., 1998, New Astr. **3**, 647

[35] Čadež A. *et al.*, 1999, New Astr., submitted

[36] Carter B., 1968, Phys. Rev. **174**, 1559

[37] Castro-Tirado A.J., Brandt S., Lund N., 1992, IAU Circular n.5590

[38] Celotti A. & Blandford R.D., 2000, in: Proc. ESO Workshop *"Black Holes in Binaries and Galactic Nuclei"*, Garching, Sept. 1999; Ed. L. Kaper, E.P.J. van den Heuvel, P.A. Woudt, Springer-Verlag, in press – astro-ph/0001056

[39] Celotti A., Miller J.C., Sciama D.W., 1999, *Astrophysical evidence for the existence of black holes*, Classical and Quantum Gravity, Millennium Issue, **16**, A3

[40] Chakrabarti S.K., 2000, in: Proc. 3rd ICRA Workshop, July 12-21, 1999; Il Nuovo Cimento, in press – astro-ph/0007254

[41] Chandrasekhar S., 1931, Astroph. J. **74**, 81

[42] Chandrasekhar S., 1983, *The Mathematical Theory of Black Holes*, Clarendon Press, Oxford

[43] Chen K. & Eardley D.M., 1991, Astroph. J. **382**, 125

[44] Chiang J. *et al.*, 2000, Astroph. J. **528**, 292

[45] Collin S. *et al.*, 2000, in: Proc. *"AGN in their Cosmic Environment"*, EDPS Conf. Series in Astron. & Astroph., in press – astro-ph/0003108

[46] Collin-Souffrin S. *et al.*, 1996, Astron. & Astroph. **314**, 393

[47] Connors P.A., Piran T., Stark R.F., 1980, Astroph. J. **235**, 224

[48] Cui W., Chen W., Zhang S.N., 1999, Astroph. J. **529**, 952

[49] Cui W., Zhang S.N., Chen W., 1998, Astroph. J. **492**, L53

[50] Curtis H. D., 1918, Publ. Lick. Obs. **13**, 9

[51] Cunningham C.T., 1975, Astroph. J. **202**, 788

[52] Cunningham C.T., 1976, Astroph. J. **208**, 534

[53] Cunningham C.T. & Bardeen J.M., 1973, Astroph. J. **183**, 237

[54] Czerny B., Zbyszewska M., Raine D.J., 1991, in Treves A. ed., *Iron Line Diagnostics in X-Ray Sources*, Springer Verlag, Berlin

[55] Dabrowski Y. *et al.*, 1997, MNRAS **288**, L11

[56] Dabrowski Y. & Lasenby A.N., 2000, MNRAS, submitted - astro-ph/0005020

[57] De Felice F., Nobili L., Calvani M., 1974, Astron. & Astroph. **30**, 111

[58] Di Matteo T. & Psaltis D., 1999, Astroph. J. **526**, L101

[59] Di Matteo T. *et al.*, 1999, MNRAS, **305**, 492

[60] Done C., Życki P.T., Smith D.A., 1998, in: Proc. of the Active X-ray Sky symposium *Results from BeppoSAX and RXTE*, October 21-24, 1997, Rome, Italy, Ed. L. Scarsi *et al.*, Elsevier, Amsterdam; Reprint: Nuclear Physics B (Proc. Suppl.) **69/1-3**, 352

[61] Done C. & Życki P.T., 1999, MNRAS **305**, 457

[62] Doran C., 1999, Phys. Rev. D, in press – gr-qc/9910099

[63] Dullemond C.P. & Turolla R., 1998, Astroph. J. **503**, 361

[64] Ebisawa K., 1996, in: *"X-ray Imaging and Spectroscopy of Cosmic Hot Plasmas"*, Eds. Makino F. & Mitsuda K., Universal Academy, Tokyo

[65] Einstein A., 1939, Ann. Math. (Princeton) **40**, 922

[66] Eracleous M., Halpern J.P., Livio M., 1996, Astroph. J. **459**, 89

[67] Fabian A.C. *et al.*, 1989, MNRAS **238**, 729

[68] Fabian A.C. *et al.*, 1995, MNRAS **277**, L11

[69] Fabian A.C. *et al.*, 2000, PASP, in press – astro-ph/0004366

[70] Fanton C. *et al.*, 1997, PASJ **49**, 159

[71] Fiore F. *et al.*, 2000, Astroph. J., accepted

[72] Fukue J. & Ohna E., 1997, PASJ **49**, 315

[73] Gebhardt K. *et al.*, 2000, Astroph. J. Lett., submitted – astro-ph/0007123

[74] George I.M. & Fabian A.C., 1991, MNRAS **249**, 352

[75] Ghez A.M. *et al.*, 1998, Astroph. J. **509**, 678

[76] Ghisellini G. *et al.*, 1991, MNRAS **248**, 14

[77] Ghisellini G., Haardt F., Matt G., 1994, MNRAS **267**, 743

[78] Giacconi R. *et al.*, 1962, Phys. Rev. Lett. **9**, 439

[79] Gilfanov M., Churazov E., Revnivtsev M., 2000, MNRAS **316**, 923

[80] Goldstein H., 1950, *Classical Mechanics*, Addison-Wesley Pub. Co., Massachusetts (USA)

[81] Greiner J., Morgan E., Remillard R.A., 1996, Astroph. J. **473**, L107

[82] Gu W.M. & Lu J.F., 2000, Astroph. J. Lett., accepted – astro-ph/0008319

[83] Guainazzi M. *et al.*, 1999, Astron. & Astroph. **341**, L27

[84] Guilbert P.W. & Rees M.J., 1988, MNRAS **233**, 475

[85] Haardt F., 1993, Astroph. J. **413**, 680

[86] Haardt F., 1994, *High Energy Processes in Seyfert Galaxies*, PhD Thesis, SISSA-ISAS, Trieste, Italy

[87] Haardt F. & Maraschi L., 1991, Astroph. J. **380**, L51

[88] Haardt F. & Maraschi L., 1993, Astroph. J. **413**, 507

[89] Haardt F., Maraschi L., Ghisellini G., 1994, Astroph. J. **432**, L95

[90] Haardt F., Maraschi L., Ghisellini G., 1997, Astroph. J. **476**, 620

[91] Hameury J.M., Marck J.A., Pelat D., 1994, Astron. & Astroph. **287**, 795

[92] Hartnoll S.A. & Blackman E.G., 2000a, MNRAS **317**, 880

[93] Hartnoll S.A. & Blackman E.G., 2000b, MNRAS, submitted - astro-ph/0009263
[94] Hazard C., Mackey M. B, Shimmins, A. J., 1963, Nature **197**, 1037
[95] Henry G. & Petrucci P.O., 1997, Astron. & Astroph. **326**, 87
[96] Herrnstein J.R. *et al.*, 1999, Nature **400**, 539
[97] Ho L.C. & Kormendy J., 2000, in: *The Encyclopedia of Astronomy and Astrophysics*, IOP Publishing
[98] Hoyle F. *et al.*, 1964, Astroph. J. **139**, 909
[99] Ichimaru S., 1977, Astroph. J. **214**, 840
[100] Inoue H., 1993, Exp. Astr. **4**, 1
[101] Iwasawa K. *et al.*, 1996a, MNRAS **279**, 837
[102] Iwasawa K. *et al.*, 1996b, MNRAS **282**, 1038
[103] Iwasawa K. *et al.*, 1999, MNRAS **306**, L19
[104] Iwasawa K. & Taniguchi Y., 1993, Astroph. J. **413**, L15
[105] Jaroszynski M., 1997, Acta Astron. **47**, 399
[106] Jaroszynski M. & Kurpiewski A., 1997, Astron. & Astroph. **326**, 419
[107] Karas V. *et al.*, 2000, MNRAS **318**, 547
[108] Karas V., Martocchia A., Šubr L., 2000, in preparation *(on spiral patterns)*
[109] Karas V. & Kraus P., 1996, PASJ **48**, 771
[110] Karas V., Lanza A., Vokrouhlický D., 1995, Astroph. J. **440**, 108
[111] Karas V., Vokrouhlický D., Polnarev A.G., 1992, MNRAS **259**, 569
[112] Kazanas D. & Nayakshin S., 2000, Astroph. J., submitted - astro-ph/0007421
[113] Kerr R.P., 1963, Phys. Rev. Lett. **11**, 237
[114] Kerr R.P. & Schild A., 1964, Am. Math. Soc. Symposium, New York
[115] Kojima Y., 1991, MNRAS **250**, 629
[116] Kormendy J. & Richstone D., 1995, ARA&A **33**, 581
[117] Krolik J.H., 2000, in: Proc. 1st KIAS Workshop *"Explosive Phenomena in Astrophysical Compact Objects"*, in press – astro-ph/0008372
[118] Kunieda H. *et al.*, 1990, Nature **345**, 786
[119] Kurpiewski A. & Jaroszynski M., 1999, Astron. & Astroph. **346**, 713
[120] Kurpiewski A. & Jaroszynski M., 2000, Acta Astron. **50**, 79
[121] Landau L.D. & Lifsits E.M., *Meccanica*, MIR - Editori Riuniti, Roma 1975
[122] Laor A., 1991, Astroph. J. **376**, 90
[123] Laor A., 2000, Astroph. J. Lett., accepted – astro-ph/0009192
[124] Laor A., Netzer H., Piran T., 1990, MNRAS **242**, 560
[125] Laplace P.S., 1796, *Exposition du Système du Monde*
[126] Lasenby A.N. *et al.*, 1997, Proc. of 5th Course *"Current Topics in Astrofundamental Physics"* held in Erice (Italy), eds. N. Sanchez and A. Zichichi, World Scient. Pub., Singapore - astro-ph/9707165
[127] Lee J.C. *et al.*, 1999, MNRAS **310**, 973

[128] Lee J.C. *et al.*, 2000, MNRAS, in press – astro-ph/9909239

[129] Lense J. & Thirring H., 1918, Physik. Z. **19**, 156

[130] Lightman A.P. & White N.E., 1988, Astroph. J. **335**, 57

[131] Lo K.Y. *et al.*, 1998, Astroph. J. **508**, L61

[132] Longair M.S., 1981 (second edition 1994), *High Energy Astrophysics* , Cambridge Univ. Press, Cambridge (UK)

[133] Lubiński P. & Zdziarski A.A., 2000, MNRAS, submitted – astro-ph/0009017

[134] Luminet J.P., 1979, Astron. & Astroph. **75**, 228

[135] Lynden-Bell D., 1969, Nature **223**, 690

[136] Maciołek-Niedźwiecki A. & Magdziarz P., 1998, in *"Observational Evidence for Black Holes in the Universe"*, ed. S. K. Chakrabarti; Kluwer, Dordrecht - astro-ph/9805328

[137] Magorrian J. *et al.*, 1998, AJ **115**, 2285

[138] Malzac J. *et al.*, 1998, Astron. & Astroph. **336**, 807

[139] Mannucci F., Salvati M., Stanga R.M., 1992, Astroph. J. **394**, 98

[140] Markwardt C.B., Swank J.H. & Taam R.E., 1999, Astroph. J. **513**, L37

[141] Markowitz A. & Edelson R., 2000, Astroph. J., accepted - astro-ph/0009422

[142] Martocchia A., 1996, *"Le geodetiche in metrica di Kerr. Applicazione a dischi di accrescimento attorno a buchi neri rotanti"*, First Degree Thesis, Univ. "La Sapienza", Roma

[143] Martocchia A. & Matt G., 1996, MNRAS **282**, L53-L57

[144] Martocchia A. & Matt G., 1997, in: Proc. 12th Italian Conference on General Relativity and Gravitational Physics (SIGRAV), held in Rome in September 1996, World Scient. Publ., Singapore

[145] Martocchia A., Matt G., Karas V., 1999, in: Proc. of the *X-Ray Astronomy '999* Meeting, held in Bologna, 6-10/9/1999, Astroph. Lett. & Comm., in press

[146] Martocchia A., Karas V., Matt G., 2000, MNRAS **312**, 817

[147] Martocchia A., Haardt F., Matt G., 2000, in preparation

[148] Martocchia A., Matt G., Karas V., 2000, in: Proc. IX Marcel Grossmann Meeting, held in Rome, July 2000, in preparation

[149] Mathur S., 2000, MNRAS **314**, L17

[150] Matsuoka M. *et al.*, 1990, Astroph. J. **361**, 400

[151] Matt G., 1992, *"Dischi di accrescimento illuminati da una sorgente centrale: spettro e polarizzazione della radiazione X"*, PhD Thesis, Univ. "La Sapienza", Rome

[152] Matt G., 2000, in: Proc. of the *X-Ray Astronomy '999* Meeting, held in Bologna, 6-10/9/1999, Astroph. Lett. & Comm., in press – astro-ph/0007105

[153] Matt G., 2000b, Astron. & Astroph., in press – astro-ph/0002427

[154] Matt G., Fabian A.C., Reynolds C.S., 1997, MNRAS **289**, 175

[155] Matt G., Fabian A.C., Ross R.R., 1996, MNRAS **280**, 823

[156] Matt G., Fabian A.C., Ross R.R., 1993, MNRAS **262**, 179

[157] Matt G., Perola G.C., Piro L., 1991, Astron. & Astroph. **247**, 25

[158] Matt G. *et al.*, 1992, Astron. & Astroph. **257**, 63; Erratum in: Astron. & Astroph. **263**, 453

[159] Matt G., Perola G.C., Stella L., 1993, Astron. & Astroph. **267**, 643

[160] McKernan B. & Yaqoob T., 1998, Astroph. J. **501**, L29

[161] Menou K., Quataert E., Narayan R., 1997, in: Proc. VIII Marcel Grossmann Meeting, held in Jerusalem, June 1997 – astro-ph/9712015

[162] Merloni A. & Fabian A.C., 2000, MNRAS, accepted – astro-ph/0009498

[163] Meyer F., Liu B., Meyer-Hofmeister E., 2000, Astron. & Astroph., in press - astro-ph/0007091

[164] Michell J., 1784, Phil. Trans. R. Soc. Lond. **74**, 35

[165] Miller J. S. (ed.), 1985, in: Proc. of the 7th Santa Cruz Workshop *"Astrophysics of Active Galaxies and Quasi-Stellar Objects"*, Oxford University Press, Oxford (UK)

[166] Miller J.C., 1997, in: Proc. 12th Italian Conference on General Relativity and Gravitational Physics (SIGRAV), held in Rome in September 1996, World Scient. Publ., Singapore

[167] Miller J.M. *et al.*, 2000, Astroph. J., in press – astro-ph/0008118

[168] Mineshige S. *et al.*, 2000, PASJ **52**, 499

[169] Mirabel I.F. & Rodriguez L.F., 1994, Nature **371**, 46

[170] Misner C.W., Thorne K.S., Wheeler J.A., 1973, *Gravitation*, Freeman & Co., New York

[171] Misra R., 1999, IUCAA preprint 32/99

[172] Misra R., 2000, MNRAS, submitted – astro-ph/9912178

[173] Misra R. & Kembhavi A.K., 1998, Astroph. J. **499**, 205

[174] Misra R. & Sutaria F.K., 1999, Astroph. J. **517**, 661

[175] Miyoshi M. *et al.*, 1995, Nature **373**, 127

[176] Miwa T. *et al.*, 1998, PASJ **50**, 325

[177] Molendi S. *et al.*, 2000, in: Proc. of the *X-Ray Astronomy 2000* Meeting, held in Mondello (PA), September 2000 - in preparation

[178] Morgan E.H., Remillard R.A. & Greiner J., 1997, Astroph. J. **482**, 993

[179] Mushotzky R.F. *et al.*, 1978, Astroph. J. **220**, 790

[180] Mushotzky R.F. *et al.*, 1995, MNRAS **272**, L9

[181] Nandra K., 2000, in: Proc. of the *X-Ray Astronomy '999* Meeting, held in Bologna, 6-10/9/1999, Astroph. Lett. & Comm., in press - astro-ph/0007356

[182] Nandra K., 1999, in: *Quasars and Cosmology*, Ed. Ferland G. & Baldwin J., ASP, San Francisco

[183] Nandra K. & Pounds K.A., 1994, MNRAS **268**, 405

[184] Nandra K. *et al.*, 1997a, Astroph. J. **477**, 602

[185] Nandra K. *et al.*, 1997b, Astroph. J. **488**, L91

[186] Nandra K. *et al.*, 1999, Astroph. J. **523**, L17

[187] Narayan R. & Yi I., 1995, Astroph. J. **452**, 71

[188] Narayan R. *et al.*, 1998a, Astroph. J. **492**, 554

[189] Narayan R., Mahadevan, R., Quataert E., 1998b, in: *"Theory of Black Hole Accretion Disks*, eds. M. A. Abramowicz, G. Bjornsson, J. E. Pringle, Cambridge Univ. Press, Cambridge (UK)

[190] Narlikar J.V., 1994, Am. J. Phys. **62** (10), 903

[191] Nayakshin S., 2000a, Astroph. J. Lett., submitted – astro-ph/0005603

[192] Nayakshin S., 2000b, Astroph. J. Lett., submitted – astro-ph/0007152

[193] Nayakshin S., Kallman T.R., Kazanas D., 1999, Astroph. J., submitted – astro-ph/9909359

[194] Nayakshin S. & Kallman T.R., 2000, Astroph. J., submitted - astro-ph/0005597

[195] Nobili L. *et al.*, 2000, Astroph. J. **538**, 137

[196] Novikov I.D. & Thorne K.S., 1973, in *Black Holes*, ed. C. DeWitt & B. DeWitt, Gordon & Breach, New York

[197] Novikov I.D., Thorne K.S., Page D.N., 1974, Astroph. J. **191**, ...

[198] Nowak A.M. & Chiang J., 2000, Astroph. J. **531**, L13

[199] Ogura J., Ohuo N., Kojima Y., 2000, PASJ **52**/5

[200] Oppenheimer J.R. & Snyder H., 1939, Phys. Rev. **56**, 455

[201] Ozel F. & Di Matteo T., 2000, Astroph. J., submitted – astro-ph/0004267

[202] Paczyński B. & Wiita P.J., 1980, Astron. & Astroph. **88**, 23

[203] Page D.N. & Thorne K.S., 1974, Astroph. J. **191**, 449

[204] Pariev V.I. & Bromley B.C., 1997, in: Proc. of the 8th Annual October Astrophysics Conference in Maryland - astro-ph/9711214

[205] Pariev V.I. & Bromley B.C., 1998, Astroph. J. **508**, 590

[206] Peterson B.M. & Wandel A., 2000, Astroph. J. **540**, L13

[207] Pineault S. & Roeder R.C., 1977a, Astroph. J. **212**, 541

[208] Pineault S. & Roeder R.C., 1977b, Astroph. J. **213**, 548

[209] Piro L., Matt G., Ricci R., 1997, A&AS **126**, 525

[210] Pounds K.A. *et al.*, 1990, Nature **344**, 132

[211] Pringle J.E. & Rees M., 1972, Astron. & Astroph. **21**, 1

[212] Quataert E. & Gruzinov A., 1999, Astroph. J., in press - astro-ph/9912440

[213] Quataert E. & Narayan R., 1999, Astroph. J. **520**, 298

[214] Rauch K. & Blandford R.D., 1994, Astroph. J. **421**, 46

[215] Reig P. *et al.*, 2000, Astroph. J., in press – astro-ph/0001134

[216] Revnivtsev M., Gilfanov M., Churazov E., 1999, Astron. & Astroph. **347**, L23

[217] Reynolds C.S., 1996, Ph.D. Thesis, Univ. of Cambridge, UK

[218] Reynolds C.S., 1997, MNRAS **286**, 513

[219] Reynolds C.S., 2000a, Astroph. J., in press – astro-ph/9912001

[220] Reynolds C.S., 2000b, in: Proc. of the Workshop *"Probing the Physics of Active Galactic Nuclei"*, NASA-GSFC – astro-ph/0009503

[221] Reynolds C.S., Fabian A.C., Inoue I., 1995, MNRAS **276**, 1311
[222] Reynolds C.S. & Begelman M.C., 1997, Astroph. J. **488**, 109
[223] Reynolds C.S. *et al.*, 1999, Astroph. J. **514**, 164
[224] Reynolds C.S. & Wilms J., 2000, Astroph. J. **533**, 821
[225] Reynolds C.S., Nowak M.A., Maloney P.R., 2000, Astroph. J., in press – astro-ph/0004068
[226] Rhoades C.E. & Ruffini R., 1974, Phys. Rev. Lett. **32**, 324
[227] Robertson S.L., 1998, PASP, submitted – astro-ph/9801269
[228] Ross R.R. & Fabian A.C., 1993, MNRAS **261**, 74
[229] Ross R.R. *et al.* 1996 ...
[230] Ross R.R., Fabian A.C., Young A.J., 1999, MNRAS **306**, 461
[231] Ruszkowski M., 2000, MNRAS **315**, 1
[232] Ruszkowski M. & Fabian A.C., 2000, MNRAS **315**, 223
[233] Ruszkowski M. *et al.*, 2000, MNRAS **317**, L11
[234] Rybicky G.B. & Bromley B.C., 1997, preprint astro-ph/9711104
[235] Salpeter E.E., 1964, Astroph. J. **140**, 796
[236] Sanbuichi K., Fukue J., Kojima Y., 1994, PASJ **46**, 605
[237] Schmidt M., 1963, Nature **197**, 1040
[238] Semerák O. & Karas V., 1999, Astron. & Astroph. **343**, 325
[239] Semerák O., Karas V., De Felice F., 1999, PASJ **51**, 571
[240] Seyfert C. K., 1943, Astroph. J.**97**, 28
[241] Shakura N.I. & Sunyaev R.A., 1973, Astron. & Astroph. **24**, 337
[242] Shapiro S.L., Lightman A.P. & Eardley D.M., 1976, Astroph. J. **204**, 187
[243] Shields G.A., 1978, Nature **272**, 706
[244] Sincell M.W., 1998, Proc. for the Atelier ADJ-LAOG, *"La relation accretion-ejection"*, Observatoire de Grenoble – astro-ph/9801088
[245] Speith R., Riffert H., Ruder H., 1995, Comp. Phys. Comm. **88**, 109
[246] Spruit H.C., 2000, in: *The neutron star – black hole connection*, NATO ASI Elounda 1999, J. Ventura *et al.* Eds., in press - astro-ph/0003143
[247] Stella L., 1990, Nature **344**, 747
[248] Stella L. & Vietri M., 1998, Astroph. J. **492**, L59
[249] Straumann N., 1988, *Allgemeine Relativitätstheorie und relativistische Astrophysik*, Springer Verlag, Heidelberg
[250] Sulentic J.W., Marziani P., Calvani M., 1998a, Astroph. J. **497**, L65
[251] Sulentic J.W. *et al.*, 1998b, Astroph. J. **501**, 54
[252] Sulentic J.W., Marziani P., D. Dultzin-Hacyan, 1998c, in: *Structure and Kinematics of Quasars Broad Line Regions*, Proceedings of a meeting held in Lincoln, March 23-36, 1998, ASP Conference Series – astro-ph/9808166
[253] Szuszkiewicz E. & Miller J.C., 1997, MNRAS **287**, 165
[254] Szuszkiewicz E. & Miller J.C., 1998, MNRAS **298**, 888
[255] Tanaka Y. *et al.*, 1995, Nature **375**, 659

[256] Thorne K.S., 1974, Astroph. J. **191**, 507

[257] Treves A., Maraschi L., Abramowicz M., 1988, Publ. Astron. Soc. Pac. **100**, 427

[258] Turner T.J. *et al.*, 1998, Astroph. J. **493**, 91

[259] Turolla R. & Dullemond C.P., 2000, Astroph. J. **531**, 49

[260] Ueda Y. *et al.*, 1998, Astroph. J. **492**, 782

[261] Van der Klis M., 1998, Nucl. Phys. B **69**, 103

[262] Viergutz S.U., 1993, Astron. & Astroph. **272**, 355

[263] Wandel A., 2000, contribution at the Joint MPE-AIP-ESO Workshop on NLS1's, Bad Honnef, december 1999 (http://wave.xray.mpe.mpg.de/conferences/nls1-workshop); New Astron. Rev., in press - astro-ph/0005130

[264] Wang J.M. *et al.*, 2000, Astroph. J. **544**, in press – astro-ph/0006268

[265] Wang J.X., Zhou Y.Y., Wang T.G., 1999, Astroph. J. **523**, L129

[266] Wang J.X. *et al.*, 1999b, Astroph. J. **516**, L65

[267] Weaver K.A. & Yaqoob T., 1998, Astroph. J. **502**, 139

[268] Weaver K.A. & Reynolds C.S., 1998, Astroph. J. **503**, L39

[269] Weaver K.A., Gelbord J., Yaqoob T., 2000, Astroph. J., accepted - astro-ph/0008522

[270] Weedman D. W., 1986, *Quasi-stellar Objects*, Cambridge University Press, Cambridge (UK)

[271] Wilkins D.C., 1972, Phys. Rev. D **5**, 814

[272] Woltjer L., 1990, *"Phenomenology of active galactic nuclei"*, in: *Active Galactic Nuclei*, with Blandford R.D. & Netzer H., Saas-Fee Advanced Course 20 Lecture Notes, Eds. T. J.-L. Courvoisier & M. Mayor, Springer-Verlag, Berlin

[273] *X-Ray Binaries*, ed. Lewin W.H.G., Van Paradijs J., Van den Heuvel E.P.J., Cambridge Univ. Press, Cambridge (UK) 1995

[274] Yaqoob T. *et al.*, 1995, Astroph. J. **453**, L81

[275] Yaqoob T. *et al.*, 1996, Astroph. J. **470**, L27

[276] Yaqoob T. & Weaver K.A., 1997, *X-ray Imaging and Spectroscopy of Cosmic Hot Plasmas*, Univ. Acad. Press, 201

[277] Young A.J., Ross R.R., Fabian A.C., 1998, MNRAS **300**, L11

[278] Young A.J. *et al.*, 1999, AAS Meeting 195, 126.04

[279] Young A.J. & Reynolds C.S., 2000, Astroph. J. **529**, 101

[280] Yu Q., Lu Y., 1999, MNRAS, in press – astro-ph/9908079

[281] Zdziarski A.A. *et al.*, 1996, MNRAS **283**, 193

[282] Zdziarski A.A., 1999, *X-rays and soft gamma-rays from Seyferts, radio galaxies, and BH binaries*, in: *High Energy Processes in Accreting Black Holes*, eds. PoutanenJ., Svensson R., ASP Conf. Series – astro-ph/9812449

[283] Zdziarski A.A., Lubiński P., Smith D.A., 1999, MNRAS **303**, L1

[284] Zeldovich Y.B. & Novikov I.D., 1964, Sov. Phys. Dokl. **158**, 811

[285] Zhang S.N., Cui W., Chen W., 1997, Astroph. J. **482**, L155

[286] Zhang S.N. *et al.*, 2000, Science **287**, 1239
[287] Życki P.T., Done C., Smith D.A., 1997, Astroph. J. **488**, L113
[288] Życki P.T., Done C., Smith D.A., 1998, Astroph. J. **496**, L25
[289] Życki P.T., Done C., Smith D.A., 1999, MNRAS **305**, 231

Appendix: Conventions, Notation and Useful Formulae

Conventions

For the metric we used the usual conventions and signature (Chandrasekar 1983): four-vectors are either written in boldface style, or through individual components, with latin indices indicating the first three (spatial) components, and greek indices for all four components.

A dot on top of a variable indicates derivative with respect to an affine parameter, e.g. the proper time τ or some $\sigma = k \cdot \tau$. Any other derivative is expressed in an explicit way to avoid ambiguity.

All quantities are generally expressed in *geometrical units* ($G = 1$, $c = 1$), so that dimensions for masses, lenghts, angular momenta, velocities and times are in *centimeters*, unless a transformation to physical quantities is indicated explicitely. For instance, in such units the solar mass ($\sim 4 \times 10^{30}$ kg) results to be $M_\odot \simeq 1.48 \times 10^5$ centimeters.

A fundamental quantity in accretion theory is the *Eddington luminosity*, which expresses the radiation output of an equilibrium configuration in which the radiation pressure on plasma balances gravity:

$$L_{Edd} = \frac{4\pi G M m_P c}{\sigma_T} \simeq 1.3 \times 10^{38} \frac{M}{M_\odot} \quad [\mathrm{erg\ s^{-1}}].$$

It is useful to remind here the values of the *fundamental constants* we used all throughout this work:
c is the light speed $\simeq 2.998 \times 10^{10}$ cm s^{-1};
G is the constant of universal gravitation (6.673×10^{-11} m^3 kg^{-1} s^{-2});
h is the Planck constant, equal to 6.6262×10^{-27} erg s.
σ is the Stefan-Boltzmann constant: $\sigma = 5.67 \times 10^{-8}$ Wm^{-2}K^{-4}.

In this work we analyze phenomena which originate close to very large mass concentrations and therefore in extreme gravitational fields. However,

Table 5.1: Abbreviations and acronymes used all throughout the text

AD	Accretion Disc
ADAF	Advection Dominated Accretion Disc
ADIOs	Advection Dominated Inflow-Outflows
AGN	Active Galactic Nucleus
ASCA	Advanced Satellite for Cosmology and Astrophysics
BBB	Big Blue Bump
BH	Black Hole
BHC	Black Hole Candidate
B-L	Boyer-Lindquist (coordinates)
BLR	Broad Lines Region
FR	Fanaroff-Riley (radiogalaxy)
GR	General Theory of Relativity
K-N	Kerr-Newman (coordinates)
K-S	Kerr-Schild (coordinates)
LMXRB	Low Mass X-Ray Binary
LNRF	Local Non-Rotating Frame
NLSy-1	Narrow Line Seyfert 1 (galaxy)
NS	Neutron Star
PN	Pseudo-Newtonian
QPO	Quasi Periodic Oscillation
Quasar	Quasi Stellar Radio Source
QSO	Quasi Stellar Object
RXTE	Rossi X-ray Timing Explorer (satellite)
SS	Shakura-Sunyaev (accretion disc)
Sy	Seyfert (galaxies)

the spacetime is described by the standard BH metrics, without need for ad-hoc integrations of the Einstein's field equations. This because the outside matter, affected by the compact object's (BH) strong gravity, has negligible mass with respect to it, i.e. can be accounted for as test particles. No effects of self-gravity are thus taken into account, if not explicitly mentioned.

Auxiliary Reference Frames

The gravitational field of a rotating body in GR is different from the field induced by a static body. Namely, the metric is "dragged" around the axis of rotation, and this effect influences the motion of particles and fluids. Near the body, static observers – i.e. observers who are at rest with respect to the distant "fixed stars" – do not possess any privileges compared to other observers: in fact, they cannot even exist in some spacetime regions, for instance in the ergosphere, where all observers are forced to rotate around the BH in the same sense of ω.

Thus it is interesting to see what happens if we introduce a reference frame which is "locked" to the rotation *of the metric* (Bardeen 1970; Bardeen *et al.*, 1972). This can be done at any point – except for the symmetry axis, where the metric degenerates – through constructing an orthonormal tetrad of four-vectors

$$(\mathbf{e}_{(\mu)}) \equiv (\mathbf{e}_{(0)}, \mathbf{e}_{(1)}, \mathbf{e}_{(2)}, \mathbf{e}_{(3)}),$$

which is attached to the "locally non-rotating" observer, i.e. to the test particle which moves around the symmetry axis with the angular velocity ω, so that its resulting angular momentum is zero.

Such a tetrad is the basis of a *locally non-rotating frame* (**LNRF**). This reference frame "rotates together with the geometry" so that, the physical processes are easier to describe in it. The world line of an observer located at the origin of such a system has a constant r, a constant θ, and a ϕ which rotates with ω (see (2.3)).

If we indicate the basis versors of the B-L system as partial derivatives with respect to the corresponding coordinates ($\partial_\mu \equiv \frac{\partial}{\partial x^\mu}$), the orthonormal basis of a LNRF built in (t, r, θ, ϕ)) is the following:

$$\mathbf{e}_{(0)} = e^{-\nu}(\partial_t + \omega\partial_\phi) \tag{5.1}$$
$$\mathbf{e}_{(1)} = e^{-\mu_1}\partial_r \tag{5.2}$$
$$\mathbf{e}_{(2)} = e^{-\mu_2}\partial_\theta \tag{5.3}$$
$$\mathbf{e}_{(3)} = e^{-\chi}\partial_\phi. \tag{5.4}$$

This basis gives the directions of the four axes of a locally Minkowskian reference frame (e.g. Synge 1960), which means that at any time *the local*

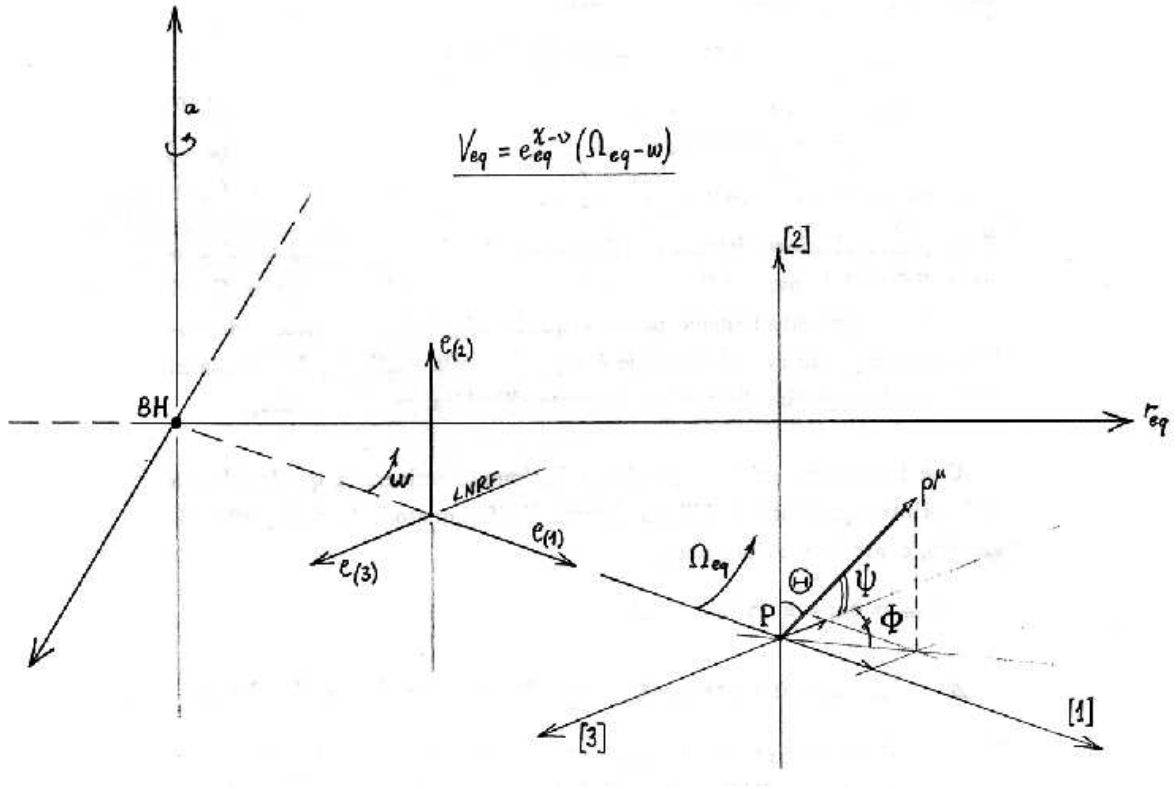

Figure 5.1: Reference frames used for the study of circular equatorial and photon trajectories.

system ($\mathbf{e}_{[\mu]}$) attached to an observer differs from the corresponding LNRF ($\mathbf{e}_{(\mu)}$) at that point by a simple Lorentz trasformation. One just has to know which is the relative velocity between the two systems

$$\mathbf{u}^{(\alpha)} = u^{\mu}\mathbf{e}_{\mu}^{(\alpha)},$$

or the three-velocity

$$\mathbf{v}^{(\mathbf{i})} = \frac{u^{\mu}\mathbf{e}_{\mu}^{(i)}}{u^{\mu}e_{\mu}^{(0)}}$$

and then to operate a *boost*.

Consider for instance what happens in the case of an equatorial disc ($\theta = \pi/2$; $r > r_{ms}$). Between the LNRF and the locally comoving frame of a particle – i.e. the *local disc frame* **LDF** ($\mathbf{e}_{[\mu]}$) – one uses the relative velocity V_{eq}:

$$\begin{aligned} \gamma_{eq} &= (1 - V_{eq}^2)^{-1/2} \\ &= \frac{\Delta^{1/2}(r^{3/2} \pm a)}{r^{1/4}(r^{3/2} - 3r^{1/2} \pm 2a)^{1/2}(r^3 + a^2 r + 2a^2)^{1/2}}. \end{aligned} \tag{5.5}$$

The corresponding four-vectors basis is therefore:

$$\mathbf{e}_{[0]} = \gamma\mathbf{e}_{(0)} + V_{eq}\gamma\mathbf{e}_{(3)} = e^{-\nu}\gamma(\partial_t + \Omega\partial_{\phi}) \tag{5.6}$$

$$\mathbf{e}_{[1]} = \mathbf{e}_{(1)} = e^{-\mu_1}\partial_r \tag{5.7}$$

$$\mathbf{e}_{[2=\Theta]} = \mathbf{e}_{(2)} = e^{-\mu_2}\partial_{\theta} \tag{5.8}$$

$$\mathbf{e}_{[3=\Phi]} = \gamma V_{eq}\mathbf{e}_{(0)} + \gamma\mathbf{e}_{(3)} = \gamma\left[V_{eq}e^{-\nu}\partial_t + (V_{eq}e^{-\nu}\omega + e^{-\chi})\partial_{\phi}\right] \tag{5.9}$$

Θ and Φ are respectively the polar and azimuthal angles of the momentum-energy vector at the point of emission. (see Figure 5.1). The coefficient $e^{-\nu}\gamma$, which appears in the expression of $\mathbf{e}_{[0]}$, is sometimes called *redshift factor* and written as e^{ψ} (e.g. Fanton *et al.* 1996); this because its inverse, which on the equatorial plane results to be equal to

$$e^{-\psi} = \frac{r^{3/4}(r^{3/2} \pm a - 3r^{1/2} \pm a)^{1/2}}{(r^{3/2} \pm a)},$$

(more expressions in: Fanton *et al.* 1996, Hameury *et al.* 1994 (3.16), Cunningham & Bardeen 1973 (3.17),) is found in the expression of g_{∞} (3.9).

The four vectors of a comoving basis are called by relativists "legs" (*Beine*, in German) of the tetrad they form. We enumerate in () the LNRF indices, while with [] we refer to the components of vectors and tensors in

reference frames attached to the observers: disc matter (LDF), particles, photons, etc. They have to be raised or lowered with the flat Minkowski metric $\eta = diag(1, -1, -1, -1)$;

Note that in every orthonormal tetrad the first (time) versor is nothing else than its four-velocity; so, for the photon or test particle we have $\mathbf{u}_{test} = \mathbf{e}_{(0)}$. The $\mathbf{e}_{(i)}$ are parallel to the corresponding B-L basis vectors: $\mathbf{e}_{(1)}$ is always directed in the radial direction; $\mathbf{e}_{(2)}$ is parallel to the rotation axis at any point $\theta = \frac{\pi}{2}$, i.e. on the accretion disc, and perpendicular to the symmetry axis at $\theta = 0$; $\mathbf{e}_{(3)}$ is degenerate on the axis, as one can see from (5.4) ($e^{-\chi}$ diverges for $\theta = 0$), and stays perpendicular to the other two vectors as follows from the "right hand rule". LNRFs are defined everywhere *except for the symmetry axis*. Nevertheless, some expressions which are derived using LNRF formalism result to have a continuous, regular behavior in regions which include the axis, too.

For a further description see: Bardeen (1970), Bardeen *et al.* (1972), or Pineault & Roeder (1977a, b).

Photon Direction and Constants of Motion

Let's consider a generic observer (at a point with coordinates (r, θ, ϕ) and a tetrad $\mathbf{e}_{[\mu]}$ attached to it) orbiting with circular uniform velocity around the symmetry axis – i.e. on a plane which is parallel to the equatorial one. Imagine that a photon is emitted from it. We are interested in finding out relations which link the costants of motion of the photon to its direction, which can be expressed through the angles formed by $\mathbf{p}_{ph}$ with the vectors $\mathbf{e}_{[i]}$ of the emitting point tetrad:

$$\frac{p_{[i]}}{p_{[0]}} = \frac{(p_\mu)_{ph} e^\mu_{[i]}}{(p_\mu)_{ph} e^\mu_{[0]}} \qquad i = 1, 2, 3 \tag{5.10}$$

Take for instance the angle which is formed with the ∂_θ direction. From the second of the previous expressions we have

$$\cos\delta_2 \equiv \frac{p_{[2]}}{p_{[0]}} = \frac{\pm V_\theta^{1/2} \Delta^{1/2} \gamma^{-1}}{A^{1/2}(1 - \lambda\Omega)}, \tag{5.11}$$

and becomes even simpler in the case $\theta = \frac{\pi}{2}$ when using the formulae for g_∞, or g_h; on the other hand, in the case $\theta \to 0$ the function V_θ diverges.

Consider the angle formed with the radial direction, i.e. with the axis itself:

$$\cos\delta_1 \equiv \frac{p_{[1]}}{p_{[0]}} = \frac{\pm V_r^{1/2} \gamma^{-1}}{A^{1/2}(1 - \lambda\Omega)}. \tag{5.12}$$

Table 5.2: Expressions of the auxiliary functions on the equatorial plane ($\theta = \frac{\pi}{2}$, $r = r_{eq}$) and on the symmetry axis ($\theta = 0$, $r = h$), normalized by m.

Function	Equatorial plane ($\theta = \frac{\pi}{2}$)	Axis ($\theta = 0$)
$\rho^2 = r^2 + a^2\cos^2\theta$	r_{eq}^2	$h^2 + a^2$
$\Delta = r^2 - 2r + a^2$	Δ_{eq}	Δ_h
$A = (r^2 + a^2)^2 - a^2\Delta\sin^2\theta$	$(r_{eq}^2 + a^2)^2 - a^2\Delta_{eq}$	$(h^2 + a^2)^2$
$\Lambda \equiv A\rho^{-2}$	$r_{eq}^2 + a^2 + 2a^2 r_{eq}^{-1}$	$h^2 + a^2$
$\omega = 2arA^{-1}$	$2ar_{eq}^{-1}\Lambda_{eq}^{-1}$	$\frac{2ah}{(h^2+a^2)^2}$
$e^{2\nu} = \rho^2\Delta A^{-1}$	$\Delta_{eq}\Lambda_{eq}^{-1}$	$\frac{\Delta_h}{h^2+a^2}$
$e^{2\chi} = A\rho^{-2}\sin^2\theta$	Λ_{eq}	0
$e^{2\mu_1} = \rho^2\Delta^{-1}$	$r_{eq}^2\Delta_{eq}^{-1}$	$\frac{h^2+a^2}{\Delta_h}$
$e^{2\mu_2} = \rho^2$	r_{eq}^2	$h^2 + a^2$

This expression is perfectly defined also for θ going to zero: given a source S fixed at distance h on the BH, if δ is the angle between its energy-momentum vector and the symmetry axis, then

$$\cos\delta = \pm\frac{V_h^{1/2}}{h^2 + a^2}. \tag{5.13}$$

We will now consider the photon emission from matter particles in the disc. For a fixed $r = req$ we can link the photon's constants of motion (λ, q) to its spectral shift $g_\infty = E_o/E_e$ and direction, given by Θ and Φ (see figure 5.1):

$$\begin{aligned} \cos\Theta &= \frac{p_{[2]}}{p_{[0]}} \\ \sin\Theta\sin\Phi &= \frac{p_{[1]}}{p_{[0]}} \\ \sin\Theta\cos\Phi &= -\frac{p_{[3]}}{p_{[0]}} = \cos\Psi. \end{aligned} \tag{5.14}$$

Again, we can write these formulae using the scalar products between the comoving tetrad of the particle ($\mathbf{e}_{[\mu]}$) and the energy-momentum vector of the photon $\mathbf{p}_{ph}$.

Without regard of the meaning of Ω_e on the axis, it simply holds that [cp. (5.22)] $\gamma \overset{\theta\to 0}{\longrightarrow} 1$.
On the equatorial plane ($\theta = \frac{\pi}{2}$) we have $(V_\theta)_{ph} = q^2$, and so[20] for the spectral shift (Kojima 1991):

[20]We make use of the expressions written in the third column of Tab. 4.5 as well as those for $g = g_\infty$.

$$\cos\Theta = \frac{\pm|q|\Delta^{1/2}\gamma_{eq}^{-1}}{r\Lambda^{1/2}(1-\lambda\Omega_{eq})} = \pm|q|g_\infty r^{-1} \quad (5.15)$$

$$\sin\Theta\cos\Phi = \pm\frac{g_\infty (V_r)_{ph}^{1/2}}{r\Delta^{1/2}} \quad (5.16)$$

$$\sin\Theta\sin\Phi = g_\infty\gamma_{eq}[\lambda(e^{-\chi}+\omega V_e e^{-\nu}) - V_e e^{-\nu}] \quad (5.17)$$

It is worth paying attention that the constants of motion are *the photon's constants*, while for the matter in the disc we know that $q^2 = 0$.

In order to describe the illumination from a central source S onto the accreting matter we express the impinging photon's inclination Θ in the system of the rotating disc particle. Being $\lambda = 0$, the following can be simply derived (Martocchia 1996):

$$\cos\Theta = \frac{p_{[2]}}{p_{[0]}} = \pm V_{\theta=\pi/2}^{1/2} e_{eq}^{\nu-\mu_2}\gamma_{eq}^{-1}(1-\lambda\Omega_{eq}) = \\ = \frac{\pm|q|\Delta_{eq}^{1/2}}{r\Lambda^{1/2}\gamma_{eq}} = \frac{\pm|q|}{rg_h}\sqrt{\frac{\Delta_h}{h^2+a^2}}. \quad (5.18)$$

and the + sign will be always taken being $0 \leq \Theta \leq 90$.

Let us now consider the emission of a photon from the Keplerian disc. Cunningham & Bardeen (1973) wrote an expression for explicitly linking the constants of motion to the angles formed, in the emission point P, by the vector tangential to the photon's trajectory with the vertical axis (Θ) and with the direction tangential to the orbit Ψ:

$$\lambda = \frac{\cos\Psi + V_{eq}}{e^{\nu-\chi} + \Omega_{eq}\cos\Psi + \omega V_{eq}} \quad (5.19)$$

$$q = rg\cos\Theta. \quad (5.20)$$

The second relation directly comes from (5.15); q is real, as for all orbits intersecting the equatorial plane. Also the first expression comes from (5.15)-(5.17), which are in fact redundant now. Being $\cos\Psi = \sin\Theta\sin\Phi$, eq. (5.19) is derived from (5.17). Therefore the second expression written by Kojima (1991) can serve just for a numerical check.

Energy Shift and Constants of Motion

Let us consider two points in the space – not necessarily on the equatorial plane – rotating along uniform circular orbits around the BH spin axis with

angular velocity Ω_e, Ω_o. From Eq. (3.9) we get

$$g = \frac{e_e^\nu \gamma_o (1 - \lambda\Omega_o)}{e_o^\nu \gamma_e (1 - \lambda\Omega_e)}, \tag{5.21}$$

where the Lorentz factor γ is

$$\gamma = (1 - V^2)^{-1/2} = [1 - (\Omega - \omega)^2 e^{2\chi - 2\nu}]^{-1/2} \tag{5.22}$$

(from (3.2)). This function is regular at any point in the spacetime, even on the axis itself *if* $\lambda = 0$ (i.e. if there is no angular momentum component along the axis). This must be underlined because we are particularly interested in the case of a source located *on the symmetry axis*. Let's write, as an example, the spectral shift of the radiation from such a point source S to the matter located at some disc radius r_{eq}:

$$g \xrightarrow{\theta \to 0} g_h(h, r_{eq}) = F_{r_{eq},h} \gamma_{eq}, \tag{5.23}$$

where $F_{r_{eq},h}$, using Tab. 4.5, is

$$F_{r_{eq},h} = \frac{e_h^\nu}{e_{eq}^\nu} = \sqrt{\frac{\Delta_h \Lambda_{eq}}{\Delta_{eq}(h^2 + a^2)}}. \tag{5.24}$$

Non-Keplerian Motion

For the sake of illustration and completeness we shall now see how a radial component of the motion of the matter in the disc may be taken into account in the formulae. Still using 3.8, we get:

$$g = \left[g^{00}(u_0)_e + g^{30}\left((u_3)_e - \lambda(u_0)_e\right) - g^{33}\lambda(u_3)_e + g^{11}(u_1)_e (p_1)_{ph}/(p_0)_{ph} \right]^{-1}, \tag{5.25}$$

with the same notations used in chapter 2, and being:

$$\begin{aligned}
g^{00}(u_0)_e &= \left(\sqrt{\frac{A}{\rho\Delta}} + \frac{2ar\sqrt{A}}{\rho^{3/2}\Delta} v^{(\phi)} \right) \gamma, \\
g^{03}(u_3)_e &= -\frac{2ar\sqrt{A}}{\rho^{3/2}\Delta} \gamma v^{(\phi)}, \\
g^{30}\lambda\,(u_0)_e &= -2ar \left[\frac{1}{\sqrt{\rho\Delta A}} + \frac{2ar}{\rho^{3/2}\sqrt{A}\Delta} v^{(\phi)} \right] \gamma\lambda, \\
g^{33}\lambda\,(u_3)_e &= \frac{(r^2 - 2r)\sqrt{A}}{\rho^{3/2}\Delta} \gamma v^{(\phi)} \lambda, \\
g^{11}(u_1)_e \tfrac{(p_1)_{ph}}{(p_0)_{ph}} &= \frac{\sqrt{\Delta V_r}}{\rho^{3/2}} \gamma v^{(r)} \sigma_r.
\end{aligned}$$

Here, V_r is given by eq.(2.20), σ_r is the signature of $(p^1)_{ph} \propto \sigma_r \sqrt{V_r}$, and $\gamma = 1/\sqrt{1-v^2}$.

The azimuthal and radial components of the material orbital velocity, $v^{(\phi)}$ and $v^{(r)}$, can be parametrized as

$$\begin{aligned} v^{(\phi)} &= w^{\phi} v_{\rm k} \\ v^{(r)} &= w^{r} v_{\rm k} \end{aligned} \tag{5.26}$$

where $v_{\rm k} = V_{eq}$ as in (3.3), and w^r is a *negative* constant depending on the viscosity ($w^r \propto -\alpha$, unless an outflow is considered; cp. Fukue & Ohna 1997, Miwa *et al.* 1998, Pariev & Bromley 1998).

Pseudo-Newtonian Models

Pseudo-Newtonian (PN) models are useful in order to reproduce basic relativistic effects without going too much in depth with the mathematical GR machinery, when this is too cumbersome.

Although in our calculations we usually do not employ such models, but rather perform fully-relativistic computations using the formalism described in chapter 2, on some particular occasions we compared our results to those obtained with PN models. The latter have a worse degree of approximation very near to the BH, of course, but the numerical computation is fast and the result is accurate in low and medium gravity regime.

We give a short summary of such models here. For a recent account of developments on PN descriptions for the Kerr spacetime, as well as for a general discussion and more references on the subject, see Semerák & Karas (1999).

The widely used PN potential for the static BH metric is that of Paczyński & Wiita (1980) $\sim \frac{-m}{r-2m}$. It reproduces correctly the marginally stable and marginally bound circular orbits. In this context the Keplerian velocity can be written:

$$v_{\rm k} = \frac{\sqrt{r}}{r-2}; \tag{5.27}$$

This has been further corrected for the Doppler effect by Abramowicz and collaborators (1996):

$$v_{\rm k} = \sqrt{\frac{r}{(r-2)^2 + r}}; \tag{5.28}$$

this follows from substitution

$$v_{\rm k} \to \tilde{v}_{\rm k} = \sqrt{\frac{v_{\rm k}^2}{1+v_{\rm k}^2}}. \tag{5.29}$$

The Keplerian velocity takes another form in the potential by Artemova *et al.* (1996), who tried to include the effects of BH rotation:

$$v_{\rm k} = \frac{\sqrt{r}}{r-2}; v_{\rm k}^2 = \left(\frac{r}{r-r_{\rm a}}\right)^{\beta_{\rm n}} \frac{1}{r} \tag{5.30}$$

with $r_{\rm a} = 1+\sqrt{1-a^2}$, $\beta_{\rm n} = (r_{\rm ms}/r_{\rm g}-1)$; this expression can also be corrected for the Doppler effect. Artemova *et al.* (1996) pseudopotential reproduces very well the steady circular motion, but ignores all effects connected to the "rotation of the metric", i.e. frame-dragging and related effects (including the Lense-Thirring precession). This is also the reason why pseudopotentials for the Kerr metric are less used than those for the static BH case.

However, recently Semerák & Karas (1999) further refined the approximation in the Kerr case with the aim to solve the mentioned difficulty. They employed a potential which includes a purely Newtonian (gravitoelectric) term, a dragging (gravitomagnetic) term written through analogy with the electromagnetic formalism, and a space-geometry correction.

A special relativistic formula for the redshift function is used in pseudo-Newtonian models:

$$g = \frac{1}{\gamma(1-v\cos\alpha)}, \tag{5.31}$$

where $\boldsymbol{v} = v^{(r)}\boldsymbol{e_r} + v^{(\phi)}\boldsymbol{e_\phi}$ is the velocity of the disk material, and

$$\cos\alpha = -\sin\theta_{\rm o}\left(v^{(\phi)}\sin\phi + v^{(r)}\cos\phi\right) \tag{5.32}$$

the angle between $\boldsymbol{v}$ and the direction to the observer.

The Keplerian motion is $\boldsymbol{v} = v_{\rm k}\boldsymbol{e_r}$. One can thus express radial and azimuthal components of the velocity as a fraction of the Keplerian velocity itself, as in 5.26.